

SIMULATION OF WETTABILITY ALTERATION AND CO₂ INJECTION BASED
ENHANCED OIL RECOVERY IN TIGHT AND LOW PERMEABILITY
RESERVOIRS

A Dissertation

by

HYE YOUNG JUNG

Submitted to the Office of Graduate and Professional Studies of
Texas A&M University
in partial fulfillment of the requirements for the degree of

DOCTOR OF PHILOSOPHY

Chair of Committee,	Akhil Datta-Gupta
Committee Members,	Michael J. King
	Eduardo Gildin
	Debjyoti Banerjee
Head of Department,	Jeff Spath

August 2020

Major Subject: Petroleum Engineering

Copyright 2020 Hye Young Jung

ABSTRACT

Development of unconventional oil resources has attracted attention in recent years due to not only the rapid growth in energy demand but also emerging technologies such as multi-stage hydraulic fracturing with long horizontal wells. Some of the world's largest oil reservoirs are characterized by low permeability and oil-wet rocks. There has been a constant need to combat this challenge. One of the key problems in tight/low permeability reservoirs, defined as resources that contain light crude oil in a less permeable formation relative to conventional resources, is that production drops rapidly. Therefore, this limited oil recovery from primary depletion in tight formation necessitates efficient solutions for enhanced recovery. In this research, we mainly focus on the application of enhanced oil recovery (EOR) methods including gas injection and surfactant injection to increase productivity for tight and low permeability reservoirs. This dissertation also presents the performance and feasibility of various EOR methods through exhaustive simulation studies.

First, our objective is to model, scale up and optimize the process using a comprehensive chemical flood simulator with wettability alteration mechanism. We start with the surfactant mechanisms in enhanced oil recovery. We then demonstrate the effectiveness of surfactant-based nanofluids for wettability alteration using a comprehensive chemical flooding simulation. Through the optimization process, the dominant parameters affecting oil recovery in tight oil reservoirs using surfactant are first identified with a synthetic case. Then, applications are extended to field scale examples

that have different hydraulic fracture geometries from simple planar type to complex hydraulic fractures.

Second, we apply the Fast Marching Method (FMM)-based simulation to make the simulation of unconventional reservoirs more efficient for field applications. The FMM-based simulation enables us to perform fast computation while achieving a good approximation of results, compared to a full 3-D numerical simulation. Previous efforts to extend the FMM-based approach to multi-well cases have been improved to rigorously account for interferences between different wells with increased computational efficiency.

Finally, we perform hierarchical history matching using multi-objective Genetic Algorithm (MOGA) on a field example of carbon capture, utilization and storage in order to understand reservoir mechanism during primary depletion as well as CO₂ injection period. Employing the appropriate hierarchical workflow leads to successful reservoir/fluid property calibrations while providing a reasonable match between simulation responses and observed data.

DEDICATION

I dedicate this dissertation to my husband, Albert Kim, and my family.

ACKNOWLEDGEMENTS

I would like to thank my committee chair, Dr. Akhil Datta-Gupta, and my committee members, Dr. Michael J. King, Dr. Eduardo Gildin and Dr. Debjyoti Banerjee, for their guidance and support throughout the course of this research.

Thanks also go to MCERI colleagues for their mentorship and thoughtful discussion on the research and the department faculty and staff for their support to finish my Ph.D degree at Texas A&M University.

Finally, I would like to express my sincere gratitude to my parents and my husband for their support, encouragement and love.

CONTRIBUTORS AND FUNDING SOURCES

Contributors

This work was supported by a dissertation committee consisting of Professor Akhil Datta-Gupta (advisor), Michael J. King and Eduardo Gildin of the Department of Petroleum Engineering and Professor Debjyoti Banerjee of the Department of Mechanical Engineering.

In Chapter II, the Eikonal solvers used in this study were developed by Jixiang Huang and Chen Li. Also, Atsushi Iino provided the FMM-based multi-phase and multi-component simulation. In Chapter IV, the history matching was collaborated with Hyun Min Kim

All other work conducted for the dissertation was completed by the student independently.

Funding Sources

This work was supported by the member companies of the Model Calibration and Efficient Reservoir Imaging (MCERI) consortium.

TABLE OF CONTENTS

	Page
ABSTRACT	ii
DEDICATION	iv
ACKNOWLEDGEMENTS	v
CONTRIBUTORS AND FUNDING SOURCES.....	vi
TABLE OF CONTENTS	vii
LIST OF FIGURES.....	x
LIST OF TABLES	xvii
CHAPTER I INTRODUCTION AND LITERATURE REVIEW	1
1.1 Introduction.....	1
1.2 Literature Review	2
1.2.1 Overview of Wettability Alteration.....	2
1.2.2 Overview of Fast Marching Method	4
1.2.3 Overview of CO ₂ Based Enhanced Oil Recovery	5
1.3 Dissertation Outline.....	6
CHAPTER II NUMERICAL SIMULATION OF EOR FROM WETTABILITY ALTERATION IN TIGHT OIL RESERVOIR WITH MULTIPLE HYDRAULIC FRACTURES.....	8
2.1 Chapter Summary.....	8
2.2 Background	9
2.2 Methodology	12
2.2.1 Simulation of Wettability Alteration.....	12
2.2.2 Mechanisms for Wettability Alteration.....	15
2.2.3 Procedure for Modeling Wettability Alteration in Simulations	16
2.3 Applications	18
2.3.1 Case 1: Simple Planar Hydraulic Fractures.....	19
2.3.2 The Effect of Wettability Alteration on Enhanced Oil Recovery	22
2.3.3 Sensitivity Analysis.....	26
2.3.4 Multi-Objective Optimization	30

2.3.5 Case 2: Multiple-stage Planar Hydraulic Fractures.....	37
2.3.6 Case 3: Complex Hydraulic Fractures.....	39
2.4 Sensitivity Studies.....	42
2.4.1 Effect of Different Injection Timing.....	43
2.4.2 Effect of Different Relative Permeability.....	45
2.5 Conclusions.....	47
CHAPTER III MULTI-WELL EXTENSION AND APPLICATION OF FAST MARCHING METHOD (FMM) TO FIELD EXAMPLES: HANSENS FIELD	49
3.1 Chapter Summary.....	49
3.2 Background.....	51
3.3 Methodology.....	54
3.3.1 Mathematical Formulation.....	54
3.3.2 Simulation Workflow For Multi-well FMM.....	55
3.3.3 Improved Workflow of Inter-partition Transmissibility Calculation.....	57
3.4 Field Application.....	60
3.4.1 Model Setting.....	60
3.4.2 Fluid and Rock Properties.....	62
3.4.3 Reservoir Partitioning.....	64
3.4.4 Comparison of Simulation Results.....	64
3.4.5 Comparison of CPU Time.....	67
3.5 Conclusions.....	68
CHAPTER IV UNDERSTANDING RESERVOIR MECHANISM USING HISTORY MATCHING: DOVER 33 FIELD CARBON DIOXIDE EOR	70
4.1 Chapter Summary.....	70
4.2 Background.....	71
4.3 Methodology.....	73
4.3.1 EOS Model Calibration Using Genetic Algorithm.....	73
4.3.2 Hierarchical History Matching Using Genetic Algorithm.....	76
4.4 EOS Model Calibration.....	78
4.4.1 Initial EOS model.....	79
4.4.2 Experimental Data to be Matched.....	80
4.4.3 Case 1: Low Oil Formation Volume Factor.....	82
4.4.4 Case 2: High Oil Formation Volume Factor.....	83
4.4.5 Case 3: Low Oil Formation Volume Factor with Low Gas-Oil Ratio.....	85
4.5 Reservoir Model Calibration.....	87
4.5.1 Initial Model Setting.....	87
4.5.2 Sensitivity Analysis.....	89
4.5.3 Primary Depletion.....	91
4.5.4 Enhanced Oil Recovery.....	98
4.5.5 CO ₂ Injection Only Period.....	105

4.5.6 Discussion	112
4.6 Conclusions	118
CONCLUSIONS	121
REFERENCES	124
APPENDIX A COMPARISON OF EIKONAL SOLVER BETWEEN CELL-CENTER FMM AND 27PT-STENCIL FMM.....	130
A.1 Validation Using 2D Synthetic Cases	131
A.1.1 Case Setting	131
A.1.2 Comparison of Diffusive Time of Flight and Simulation Results.....	134
A.1.3 Representation of Flow Through Vertex in Finite Difference Simulation...	141
A.2 3D Synthetic Example.....	144
A.2.1 Case Setting	144
A.2.2 Simulation Results.....	145
A.3 Field Application.....	148
A.3.1 Case Setting	148
A.3.2 Simulation Results.....	148
A.4 Summary	150
APPENDIX B GLOBAL (HISTORY MATCHING TOOL USING GENETIC ALGORITHM) MANUAL	152
B.1 Source Code and Compiling by Visual Studio.....	152
B.1.1 Source Code.....	152
B.1.2 Compiling by Visual Studio	153
B.2 Preparation of Input Files	154
B.2.1 Overview of Input Files and Their Structures	154
B.2.2 Inversion Input File (*.INP)	155
B.2.3 Template (.TMPL) Files and Include (.INC) Files	157
B.2.4 The Variable Distribution (.DISTR) File.....	160
B.3 How to Run GLOBAL	160
B.3.1 Run From Visual Studio	160
B.3.2 Run From the Command Line	161
B.3.3 Output Formats	162

LIST OF FIGURES

	Page
Figure 2.1 Representation of the different wettability in a reservoir rock formation (Y. Yuan et al. (2013)).....	11
Figure 2.2 Permeability distribution in x direction (a) entire reservoir, (b) SRV region and (c) hydraulic fractures (reprinted with permission from Jung et al. 2018).....	20
Figure 2.3 Relative permeability of oil and water for each wettability condition	21
Figure 2.4 Capillary pressure curve for each wettability condition	22
Figure 2.5 Cumulative oil recovery and injection rate (Top) and wellbore block pressure (Bottom) (reprinted with permission from Jung et al. 2018)	23
Figure 2.6 Comparison of cumulative oil recovery with and without surfactant injection (reprinted with permission from Jung et al. 2018)	24
Figure 2.7 Comparison of initial and final oil saturation with and without surfactant injection (reprinted with permission from Jung et al. 2018)	25
Figure 2.8 Adsorbed concentration of surfactant (left) and wettability alteration parameter (right) (reprinted with permission from Jung et al. 2018)	25
Figure 2.9 Surfactant adsorption curve (reprinted with permission from Jung et al. 2018)	27
Figure 2.10 Tornado chart (reprinted with permission from Jung et al. 2018).....	28
Figure 2.11 Oil relative permeability on grid (a) low adsorption (b) high adsorption (reprinted with permission from Jung et al. 2018).....	29
Figure 2.12 Interfacial tension difference between high adsorption and low adsorption	29
Figure 2.13 Conflicting performance between two objectives with increasing surfactant concentration (reprinted with permission from Jung et al. 2018).....	31

Figure 2.14 Multi-objective optimization results: Comparison between initial generation and final generation (reprinted with permission from Jung et al. 2018)	32
Figure 2.15 Cluster analysis: objective functions (left) and distribution of parameters (right) (reprinted with permission from Jung et al. 2018).....	32
Figure 2.16 Comparison of the distribution of parameters: Initial generation (left) and Final generation (right) (reprinted with permission from Jung et al. 2018).....	33
Figure 2.17 Histogram of control variables in final generation: Surfactant concentration (top) and Final generation (bottom).....	34
Figure 2.18 Histogram of control variables in optimal group: Surfactant concentration (top) and Final generation (bottom).....	35
Figure 2.19 Histogram of control variables in low UF group: Surfactant concentration (top) and Final generation (bottom).....	36
Figure 2.20 Histogram of control variables in high oil gain group: Surfactant concentration (top) and Final generation (bottom).....	37
Figure 2.21 Permeability distribution of matrix and hydraulic fractures (reprinted with permission from Jung et al. 2018)	38
Figure 2.22 Oil production rate (top) and cumulative oil recovery (bottom) (reprinted with permission from Jung et al. 2018)	39
Figure 2.23 Permeability distribution (Left) and conductivity of hydraulic fractures (Right) (reprinted with permission from Jung et al. 2018).....	41
Figure 2.24 Oil production rate (top) and cumulative oil recovery (bottom) (reprinted with permission from Jung et al. 2018)	42
Figure 2.25 Comparison of cumulative oil recovery.....	44
Figure 2.26 Comparison of the amount of adsorbed surfactant	44
Figure 2.27 Comparison of bottomhole pressure	45
Figure 2.28 New relative permeability.....	45
Figure 2.29 Comparison of cumulative oil production between different relative permeability	46

Figure 2.30 Effect of shorter primary depletion duration on the oil recovery	46
Figure 3.1 Simulation workflow for multi-well FMM using equal- τ interface (Iino, 2018)	55
Figure 3.2 Simulation workflow for multi-well FMM using inter-partition transmissibility (Iino, 2018).....	56
Figure 3.3 Workflow of inter-partition transmissibility calculation (Iino, 2018)	58
Figure 3.4 New method of performing FMM for each pair of partitions.....	59
Figure 3.5 Illustration for the accumulation of pore volume within each τ contour sequentially.....	60
Figure 3.6 Hydraulic fracture and SRV region in the field application case	61
Figure 3.7 Reservoir properties for field case: (a) permeability and (b) porosity	61
Figure 3.8 Location of wells and defined zones in the simulation model.....	62
Figure 3.9 Relative permeability for a field case	63
Figure 3.10 Rock compaction curves for a field case	63
Figure 3.11 Partitioning the reservoir using equal- τ interface: Diffusive time of flight (left) and determined partitions (right)	64
Figure 3.12 Comparison of simulation results for Well #1 (Symbol: FD simulation and line: FMM).....	65
Figure 3.13 Comparison of simulation results for Well #4 (Symbol: FD simulation and line: FMM).....	66
Figure 3.14 Diffusive time of flight in the hydraulic fracture plane (top) and pressure distribution after 1 year in the original 3-D model (bottom).....	66
Figure 3.15 CPU time comparison for a field case	67
Figure 3.16 CPU time breakdown for FMM (left) and comparison of CPU time for inter-partition transmissibility calculation only (right)	68
Figure 4.1 Flowchart of hierarchical model calibration	73

Figure 4.2 Examples of phase behavior: Physically correct (left) and physically incorrect (right).....	74
Figure 4.3 Workflow of fluid model calibration.....	75
Figure 4.4 Three production periods in the Dover 33 field.....	77
Figure 4.5 Comparison of the bottomhole pressure of the injector during CO ₂ injection only period.....	77
Figure 4.6 Basis functions using Grid Connectivity-based Transform (GCT).....	78
Figure 4.7 Phase behavior of the original fluid.....	80
Figure 4.8 Volumetric properties of the original fluids.....	80
Figure 4.9 Three different oil formation volume factor cases.....	81
Figure 4.10 Results of Genetic Algorithm for Case 1.....	82
Figure 4.11 Oil formation volume factor of the history matched model for Case 1.....	83
Figure 4.12 Results of Genetic Algorithm for Case 2.....	84
Figure 4.13 Oil formation volume factor of the history matched model for Case 2.....	84
Figure 4.14 Results of Genetic Algorithm for Case 3.....	86
Figure 4.15 Oil formation volume factor of the history matched model for Case 3.....	86
Figure 4.16 Reservoir properties: porosity (left) and permeability (right).....	88
Figure 4.17 Initial pressure (left) and initial water saturation (right).....	88
Figure 4.18 Three phase relative permeability curves provided by the operator.....	89
Figure 4.19 Tornado chart for all objective functions.....	91
Figure 4.20 Performance of MOGA for primary depletion.....	92
Figure 4.21 Comparison of simulation responses of the history matched model with the observed data for primary depletion.....	92

Figure 4.22 Three different groups in optimal solutions depending on the importance of objective functions	93
Figure 4.23 Histogram of EOS models for each group.....	94
Figure 4.24 Comparison of phase behavior	94
Figure 4.25 Box plots of calibrated parameters for primary depletion	95
Figure 4.25 Continued.....	96
Figure 4.26 Comparison of simulation responses of the best updated model with the observed data	97
Figure 4.27 Comparison of relative permeability before and after history matching during primary depletion	97
Figure 4.28 Comparison of cumulative oil production with the updated model from primary depletion	98
Figure 4.29 Comparison of phase diagram for different oil and CO ₂ mixtures	99
Figure 4.30 Determination of Minimum Miscibility Pressure (MMP).....	100
Figure 4.31 Swelling factor of EOS 5	100
Figure 4.32 Density of original fluid compared with oil and CO ₂ mixture (CO ₂ mole fraction of 50%).....	100
Figure 4.33 Performance of MOGA for CO ₂ EOR period.....	102
Figure 4.34 Comparison of simulation responses of the history matched model with the observed data for CO ₂ EOR period	102
Figure 4.35 Box plots of parameters associated with relative permeability: endpoints (left) and exponents (right).....	103
Figure 4.36 Comparison of relative permeability before and after history matching during CO ₂ EOR period.....	104
Figure 4.37 Comparison of distribution for parameters associated with permeability between after primary depletion and after EOR period.....	104
Figure 4.38 Comparison of distribution for pore volume multipliers between after primary depletion and after EOR period	105

Figure 4.39 Comparison of simulation responses of the history matched model with the observed data (BHP: prediction)	106
Figure 4.40 Difference in bottomhole pressure between simulation response and the measure data in comparison to the reduced gas injection rate	106
Figure 4.41 Performance of MOGA for CO ₂ injection only period.....	107
Figure 4.42 Comparison of simulation responses of the history matched model with the observed data for CO ₂ injection only period	108
Figure 4.43 Comparison of distribution for parameters associated with relative permeability between after EOR period and after CO ₂ injection only period: endpoints (top) and exponents (bottom).....	109
Figure 4.44 Comparison of distribution for parameters associated with permeability between after EOR period and after CO ₂ injection only period	110
Figure 4.45 Comparison of distribution for pore volume multipliers between after EOR period and after CO ₂ injection only period	111
Figure 4.46 Results of Genetic Algorithm with a single objective function.....	112
Figure 4.47 Comparison of bottomhole pressure between updated models and history data.....	112
Figure 4.48 Location of monitor wells.....	113
Figure 4.49 Comparison of the bottomhole pressure for two monitor wells: the history matched model from MOGA.....	113
Figure 4.50 Comparison of the bottomhole pressure for two monitor wells: the history matched model from GA	113
Figure 4.51 Comparison of distribution of pore volume multipliers between MOGA results and GA results.....	114
Figure 4.52 Comparison of the histograms of pore volume for the updated models.....	115
Figure 4.53 Comparison of the histograms of permeability for the updated models.....	116

Figure 4.54 Difference in permeability (CO ₂ injection only period (GA) and CO ₂ EOR period).....	117
Figure 4.55 Difference in permeability (CO ₂ injection only period (MOGA) and CO ₂ EOR period)	117
Figure 4.56 Permeability of CO ₂ injection only period after GA: (a) permeability distribution (b) and (c) with the high threshold (Perm > 50md) from two different perspective	118
Figure 4.57 Permeability of CO ₂ injection only period after GA: (a) permeability distribution (b) and (c) with the low threshold (Perm < 0.005md) from two different perspective	118

LIST OF TABLES

	Page
Table 2.1 Reservoir properties (reprinted with permission from Jung et al. 2018)	20
Table 2.2 Key parameters for wettability alteration (reprinted with permission from Jung et al. 2018)	21
Table 2.3 Parameters and their range for sensitivity analysis (reprinted with permission from Jung et al. 2018)	26
Table 2.4 Statistical properties of natural fractures (reprinted with permission from Jung et al. 2018)	40
Table 2.5 Pumping schedule summary (reprinted with permission from Jung et al. 2018)	40
Table 4.1 Summary of hierarchical history matching	76
Table 4.2 Composition of the original fluid	79
Table 4.3 Comparison of experimental data with the calculated values from the history matched model for Case 1	83
Table 4.4 Comparison of experimental data with the calculated values from the history matched model for Case 2	85
Table 4.5 Comparison of experimental data with the calculated values from the history matched model for Case 3	86
Table 4.6 Pore volume and fluid in place of the reservoir	89
Table 4.7 List of parameters to be considered for history matching	90

CHAPTER I

INTRODUCTION AND LITERATURE REVIEW

1.1 Introduction

Over the years, the rapid increase in energy consumption in developing countries and the decline of readily accessible reserves have shifted attention to the various mechanisms of enhanced oil recovery for unconventional resources. Because of the low formation permeability, estimated oil recovery from primary production is normally between 5-10 % of initial oil in place from tight oil reservoirs with steep decline curves (Mohammad et al. 2017). EOR techniques can be commonly divided into three types including chemical EOR, gas EOR and thermal EOR. Especially, CO₂ injection plays a pivotal role in gas EOR for unconventional plays and shows promising results in the previous studies. Gas injection EOR, in general, shows possibility to improve oil recovery because it is favorable in terms of large injectivity with low viscosity whereas waterflooding might cause injection problems. Even though CO₂ injection EOR has been extensively performed and is well understood in conventional resources (Jarrell et al. 2002), it is still necessary to further investigate applications in tight oil reservoirs.

In addition, there have been experimental studies focusing on EOR techniques based on wettability alteration to overcome challenges in oil-wet tight oil reservoirs. It shows that the modification of the reservoir wettability can affect the eventual production rates, production fluid ratios and the residual saturations. However, most of the previous works have been primarily investigated in the laboratory with limited field application.

Therefore, better understanding of EOR mechanisms through wettability changes in the field scale tight oil reservoir is required.

This dissertation shows a practical feasibility of EOR using surfactant in unconventional resources and provides basic guidance to address appropriate usage of chemicals in the field application. This dissertation also outlines an efficient approach to modeling unconventional reservoirs accounting for multiwell interference. Finally, a systematic approach for history matching a CO₂ EOR field case is presented for understanding the underlying reservoir mechanisms.

1.2 Literature Review

In the following sections, we review literatures on the Enhanced Oil Recovery (EOR) techniques, such as wettability alteration and carbon dioxide injection.

1.2.1 Overview of Wettability Alteration

Wettability, defined as the interaction between the fluid and solid phases, affects the flow distribution of fluids in the porous medium. The surfactants enhance this interaction by placing themselves at the interface and increasing the continuity between the nanoparticles and the base fluid. Anderson W.G. (1987) and Morrow (1990) reported the role of wettability through experiments, for oil recovery by water flooding. Binshan J. et al. (2006) reported a theoretical analysis of wettability change in porous media using lipophobic and hydrophilic polysilicon nanoparticles, and stated that the water-wet formations are better than the oil wet reservoirs in terms of productivity. Dong H. et al.

(2006) on the contrary emphasized on the neutral wet formations as better producers in comparison to the water wet formations, by utilizing the alkali-surfactant-polymer (ASP) flooding. Ogolo et al. (2012) used experiments to confirm Aluminum oxide and Silicon oxide nanoparticles as good EOR agents. The authors underlined the importance of the appropriate selection strategies for choosing the base fluid for the target nanofluids to contribute positively or negatively in oil recovery. Sheshdeh (2015) discussed the popular methods for wettability alterations and emphasized the efficiency of nanotechnology for altering the wettability of the reservoir rock surface.

G. Cheraghian et al. (2014) also reports reservoir wettability alteration by using nanofluids as one of the most effective measures to increase the oil recovery as it helps in changing the fluid properties, reduces the advanced drag, reduces the interfacial tension (IFT) and increases the mobility of capillary trapped oil.

The surfactants, polymers and alkaline chemicals proved to be the appropriate choices of base fluids for nanofluids. Surfactants reduce the interfacial tension and increase the capillary number, whereas the polymers enhances the sweep efficiency. R. Ponnampati et al. (2011) found the silica-tethered polymer nanohybrids with attached water-soluble polymers to be effective in the mobilization of waterflood residual oil. The alkaline chemicals assist in reduction of interfacial tension and spontaneous emulsification. A. Karimi et al. (2012) experimentally explored the enhancement of surfactant properties by adding nanoparticles, and they achieved a substantial amount of oil recovery by free imbibition of nanofluids. M. Salehi et al. (2008) emphasized the importance of surfactants for altering wettability by proposing an alternative mechanism, where the ion-pair

formation between the charged head groups of surfactant molecules and oil components on the rock surface alter the wettability of rock surface to water-wet in comparison to the adsorbed surfactant molecules on the rock surface. Several groups [T. Zhang et al. (2010), C.R. Miranda et al. (2012), R. Hashemi et al. (2013), L. Hendraningrat et al. (2013), J. Giraldo et al. (2013)] have experimented with a variety of nanofluids in order to establish the nanofluids as strong, cheap and environment friendly EOR agent.

1.2.2 Overview of Fast Marching Method

The fast marching method (FMM) based rapid simulation has offered significant speed-up, commonly two to three orders of magnitude, for modeling unconventional reservoirs. The key concept here is a coordinate transformation from 3-D to 1-D using the ‘Diffusive-Time-of-Flight’ (DTOF) as the spatial coordinate. The DTOF represents the travel time for pressure front propagation and generalizes the concept of depth of investigation for heterogeneous reservoirs and hydraulically fractured wells. The DTOF can be efficiently computed by solving the Eikonal equation using the Fast Marching Method (FMM). While the FMM-based simulation has shown great potential for single well problems, application to multi-well problems with well-interference has remained a challenge to date.

Previous efforts to extend the FMM-based simulation to multi-well problems partitioned the flow domain based on well drainage boundaries. Within each of the subdomain, 1-D flow simulations are carried out using DTOF as the spatial coordinate. This method was shown to be a good approximation as long as the drainage boundaries

do not change significantly during the simulation period. However, most of the time in actual field cases, drainage volume partitions are not constant due to the different levels of withdrawal typically associated with differences in productivity amongst producers caused by local variations in reservoir quality and effectiveness of hydraulic fractures. Such well interference has been widely observed in the unconventional reservoirs. In addition, as well spacing is gradually decreased, the importance of well interference has received increasing attention. There are many previous studies that focused on the impact of well interference and associated optimization of well spacing (Yaich et al., 2014) as well as the mechanism of well interference by investigating the subsurface stress distribution (Wu et al., 2018).

1.2.3 Overview of CO₂ Based Enhanced Oil Recovery

Main mechanisms of EOR using CO₂ injection are well understood in conventional reservoirs. These mechanisms are widely known as oil swelling, oil viscosity/ density reduction and repressurization. In addition to pressure maintenance, high solubility of CO₂ in crude oil leads to swelling of the oil, which in turn lowers the oil viscosity as well as density . When the reservoir pressure is above Minimum Miscibility Pressure (MMP), injected CO₂ and hydrocarbons become miscible, resulting in improved oil recovery. However, the miscible flooding can only be applied under certain circumstances in terms of pressure and temperature. In cases where the reservoir is not able to withstand pressure higher than the estimated MMP, an immiscible process occurs which is mainly dependent

upon reduction in viscosity and oil phase swelling without CO₂ and hydrocarbons forming a single phase.

In unconventional reservoirs, dominant mechanisms of CO₂ injection are slightly different from the ones in conventional reservoirs due to low matrix permeability where a CO₂ diffusion effect plays a key role along with other well-known mechanisms. However, a greater of experimental studies need to be conducted to achieve a better understanding for mechanisms of CO₂ in tight oil formation. In addition to laboratory works, numerical simulations on pilot/field scale studies have been investigated to evaluate and improve the performance of CO₂ based EOR using either history matching workflow or optimization.

1.3 Dissertation Outline

This research mainly focuses on the application of EOR techniques for history matching and optimization on unconventional reservoirs using the multi-objective Genetic Algorithm (MOGA). The rest of this dissertation is organized by the following three major chapters and conclusions. The specific objectives of each chapter are outlined as follows:

In Chapter II, we present the potential applications of nanofluids in the field scale and examines the effectiveness of surfactant-based nanofluids for wettability alteration to improve oil recovery in tight oil reservoirs.

In Chapter III, we demonstrate the applicability and efficiency of multi-well Fast Marching Method simulation in conjunction with the introduction of inter-partition transmissibility. We further improve the workflow of calculating inter-partition

transmissibility, which consequently allows for performance assessment and prediction of unconventional reservoir in a practical manner.

In Chapter IV, we integrate historical production and pressure data into a reservoir model by using hierarchical history matching method with multi-objective Genetic Algorithm (MOGA), resulting in the better understanding on each production period from the primary production, EOR and duration of the CO₂ injection only.

CHAPTER II

NUMERICAL SIMULATION OF EOR FROM WETTABILITY ALTERATION IN TIGHT OIL RESERVOIR WITH MULTIPLE HYDRAULIC FRACTURES*

2.1 Chapter Summary

The focus of this paper is the application of colloidal suspensions of nanoparticles, commonly known as “nanofluids” for enhanced oil recovery in tight oil reservoirs. Nanofluids are specialized colloidal solvents, compatible with various types of fluids used in oil reservoirs and they have the potential to enhance the recovery of oil and gas from a variety of rock pores (EOR). Nanofluids can be used as an important tool to alter the properties of the formations. We examine here the underlying mechanisms, including the wettability alterations and reduction of the interfacial tension driving enhanced oil recovery in tight oil reservoirs using compositional numerical simulation.

We start with a review of the nanofluid properties critical to mobilize oil in the reservoir pore network by wettability alteration. We then demonstrate the effectiveness of surfactant-based nanofluids for wettability alteration using a comprehensive chemical flooding simulation. The modeling of wettability modification depends on a shift in relative permeability and capillary pressure curves during simulation. Altered wettability affects the residual phase saturations that, in turn, influences the relative permeability and

* Part of data reported in this chapter is reprinted with permission from “Numerical Simulation of EOR from Wettability Alteration in Tight Oil Reservoir with Multiple Hydraulic Fractures” by Jung et al. 2018: Paper SPE-191409-MS Presented at the SPE Annual Technical Conference and Exhibition held in Dallas, Texas, USA, 24-26 September 2018. Copyright 2018 Society of Petroleum Engineers.

causes oil mobilization. Moreover, capillary imbibition promotes oil recovery as the wettability is altered towards water-wet conditions. We investigate the major factors in wettability modification and how they influence the oil recovery through exhaustive sensitivity studies and a Pareto-based multi-objective optimization approach.

This study concentrates on the nanofluids mechanisms in enhanced oil recovery, including the permeability alterations, rock wettability alterations and reduction of the interfacial tension. A comprehensive simulation sensitivity study and a multi-objective optimization approach are utilized to identify the dominant parameters affecting oil recovery in tight oil reservoirs using complex surfactant based nanofluids. Based on the results, a set of guidelines are suggested for selection and application of nanofluids for improving oil recovery in tight oil reservoirs stimulated with multiple hydraulic fractures.

2.2 Background

Nanoparticles consist of precisely engineered nanostructures that have at least one geometric dimension less than $\sim 100\text{nm}$. Nanofluids are engineered colloidal suspensions of nanoparticles in a chosen solvent. The conventional base fluids are water, ethylene glycol, oil, lubricants, and various types of polymer solutions. The most commonly used nanoparticles are sourced from different types of materials: oxides (SiO_2 , Al_2O_3 , CuO , Fe_2O_3 , Fe_3O_4), metal carbides (SiC), nitrides (AlN , SiN), metals (Al , Cu , W) and organics (Fullerenes, Graphene, Carbon Nanotubes/CNT).

The recent progress in the nanoparticle synthesis methods has triggered the application of nanofluids in a wide variety of industries. The primary focus of this paper

is the application of nanofluids in the oil & gas industry. A stable nanofluids characterized by the controlled dispersion of the nanoparticles overcoming sedimentation, and eventually enhancing the properties of the base fluid, is the key to increased oil and gas production. The nanofluids are primarily attractive due to their size (e.g., less than 100 nm diameter, high surface to volume ratio, augmented surface energy, etc.) and their ability for tuning the properties of the base fluid (e.g., by varying the concentration, size, shape, and material of the nanoparticles). The nano-meter scale size allows the nanoparticles in the nanofluids to flow easily through the tight reservoir pore spaces, which in turn reduces potential for the pore spaces from getting clogged and minimizes the loss of the nanoparticles. Hence, nanotechnology based approaches provide viable option for improving recovery from tight oil reservoirs. The properties of the injected fluids in the reservoirs for oil recovery can be manipulated with the help of nanofluids to ensure enhanced oil recovery (EOR). Various types of nanofluids can be customized according to the wide variety of needs in the E&P applications. The applications of the nanofluids have garnered considerable attention in contemporary literature for the oil & gas industry. However, these studies have been primarily investigated in the laboratory with limited field application.

Nanofluids play a key role in the chemical EOR techniques and have proven to enhance the oil recovery significantly. The ultra-small size and high surface area to volume ratio enables the nanoparticles to penetrate the pores more effectively than the conventional recovery methods (T. Skauge et al. (2010), G. Cheraghian (2015)). Nanofluids increase the viscosity of the injected fluid, which results in a lower and

favorable mobility ratio. Some of the blends of nanoparticle and surfactants possess possibility for promising EOR application because of their ability to change the wettability of the rock surface. The modification of the reservoir wettability can affect the eventual production rates, production fluid ratios and the residual saturations. Hence, the tendency of the nanofluids to spread over the rock surface, relative to the other existing immiscible fluids in the reservoir, can be manipulated to enhance the recovery factor of the reservoir. The enhanced recovery factor is enabled by the nanofluids by minimizing the residual oil saturation. Wettability is determined by the contact angle of the fluid on the surface, resulting from the adhesion forces between the fluid and the solid surface. The wettability of the rock ranges from strongly water wet to strongly oil wet, and it mainly depends on the composition of the fluid and the mineralogy of the rock. A reservoir rock surface can be called neutrally wet when its surface does not have a marked preference for oil or water. The oil-wet reservoir is characterized by water contact angle values greater than 90° , the water-wet reservoir represents water contact angle values smaller than 90° and the neutral wet reservoirs are determined by water contact angle values equal to 90° as illustrated in Figure 2.1.

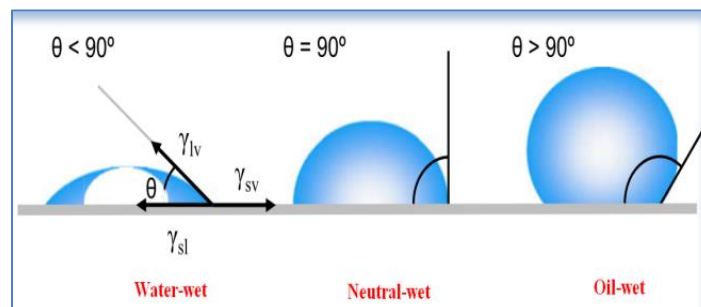


Figure 2.1 Representation of the different wettability in a reservoir rock formation (Y. Yuan et al. (2013))

Y. Yuan et al. (2013) reviewed contact angle measurement (basic and advanced) techniques for wettability determination of the materials at the macro, micro and nanoscale. The contact angle measurements are sensitive to contamination. G. Sharma et al. (2013) attempted to choose the effective wettability altering surfactants by contact angle experiments, in order to select the most promising surfactants to withstand the high temperature and high salinity environment. Contact angle measurement techniques have been used frequently by various research groups (J.S. Buckley et al. (1995), D.N. Rao (1997), N.S. Kaveh et al. (2012), O.O. Adejare et al. (2012), T.W. Teklu et al. (2015)) for accurate predictions of wettability alterations in reservoir rocks and establishing it as an essential mechanism for EOR.

Sometimes the wettability distribution of the rock surface can be classified as a mixed wettability, due to the small pores being water wet and the larger pores being oil wet, thus the surface having a variety of preferences. However, due to the coexistence of different mineralogy in an oil reservoir, we can expect different wettability, leading to a heterogeneous wettability behavior that can be classified as fractional wettability. The individual minerals comprising the reservoir rock have their respective wettability, which makes it difficult to describe the wetting nature of the reservoir rock as a whole.

2.2 Methodology

2.2.1 Simulation of Wettability Alteration

In this chapter, simulation works have been performed using UTCHEM, which is a multicomponent, multiphase, compositional model of chemical flooding processes

developed by Petroleum and Geosystems Engineering at The University of Texas at Austin (Pope and Nelson (1978), Datta-Gupta et al. (1986), Delshad et al. (1994)). UTCHEM has the ability to simulate several user-specified chemical components and solid minerals, such as water, oil, surfactant, polymer, alcohols, cations and anions. In addition, complex phase behavior, major chemical and physical phenomena are modeled, including the effects of surfactant on interfacial tension, surfactant adsorption, relative permeability and capillary pressure.

In this part, model formulations used in UTCHEM are briefly described. The details can be found elsewhere (Delshad et al. (1994)). There are three balance equations: Mass conservation equations (Eqs. (2.1)), Pressure equation (Eqs. (2.3)) and Energy balance equation (Eqs. (2.5)). Those equations are solved with the IMPES method (implicit in pressure and explicit in overall concentration/saturation) using a finite difference approach.

The mass conservation equation is expressed for each component k with respect to overall volume of component k per unit pore volume (\tilde{C}_k), which is calculated by the sum over all phases including the solid phase (Eqs. (2.2)). The pressure equation is expressed in terms of aqueous phase by summing up the mass balance on volume-occupying components (Eqs. (2.4)). Other phase pressures are obtained by accounting for the capillary pressure. The energy equation takes into account the advection and heat conduction for energy flux in the reservoir.

The conservation equation is as follows:

$$\frac{\partial}{\partial t}(\phi \tilde{C}_k \rho_k) + \vec{\nabla} \cdot \left[\sum_{l=1}^{n_p} \rho_k (C_{kl} \vec{u}_l - \vec{D}_{kl}) \right] = R_k. \quad (2.1)$$

$$\tilde{C}_k = \left(1 - \sum_{k=1}^{n_{cv}} \hat{C}_k \right) \sum_{l=1}^{n_p} S_l C_{kl} + \hat{C}_k, \text{ for } k = 1, \dots, n_c. \quad (2.1)$$

where \vec{D}_{kl} represents dispersive flux, \vec{u}_l is the phase flux from Darcy's law and R_k is the source term.

The pressure equation is given as follow:

$$\phi C_t \frac{\partial P_w}{\partial t} + \vec{\nabla} \cdot \vec{k} \cdot \lambda_{rTc} \vec{\nabla} P_w = -\vec{\nabla} \cdot \sum_{l=1}^{n_p} \vec{k} \cdot \lambda_{rlc} \vec{\nabla} h + \vec{\nabla} \cdot \sum_{l=1}^{n_p} \vec{k} \cdot \lambda_{rlc} \vec{\nabla} P_{clw} + \sum_{k=1}^{n_{cv}} Q_k, \quad (2.2)$$

$$\sum_{k=1}^{n_{cv}} C_{kl} = 1. \quad (2.3)$$

where C_t is the total compressibility and λ_{rTc} indicates total relative mobility.

The energy equation is as follows:

$$\frac{\partial}{\partial t} \left[(1-\phi) \rho_s C_{vs} + \phi \sum_{l=1}^{n_p} \rho_l S_l C_{vl} \right] T + \vec{\nabla} \cdot \left[\sum_{l=1}^{n_p} \rho_l C_{pl} u_l T - \lambda_r \vec{\nabla} T \right] = q_H - Q_L. \quad (2.4)$$

where Q_L is the heat loss to formations.

2.2.2 Mechanisms for Wettability Alteration

Nanofluids have been proposed for Enhanced Oil Recovery (EOR) where the primary mechanism for their efficacy has been described in terms of wettability alteration (Li et al. (2015), Li and Torsaeter (2015)). Since changes in wettability can affect distribution, location and mobilization of residual oil in reservoir (Delshad et al. (2006)), a deeper cognizance of fundamental mechanisms for wettability modification is important. Penny et al. (2012) conducted Ammot tests on oil saturated Bakken cores and successfully demonstrated increased oil recovery by the surfactant-based nanofluids. In the experiment, the nonionic water wetting surfactant and the nanofluids demulsifier released up to 58% of the oil, compared to the case using 2% KCL, which resulted in a displacement of 28% of the oil. Li et al. (2015) performed experimental study to investigate the impact of adsorption of nanofluids on wettability alteration and its effect on oil recovery. The authors reported that the interface between rock and liquid was replaced by hydrophilic nanoparticles adsorption layer on the rocks. Based on the experimental results, it can be concluded that wettability is determined by hydrophilicity or hydrophobicity of the nanoparticle suspensions (i.e., the nanofluids). Therefore, wettability alteration is modeled by incorporating the appropriate level of adsorption in our simulation.

In modeling the adsorption of surfactant-based nanofluids, the main characteristics of the adsorption isotherm can be represented by using a Langmuir-type isotherm. In general, the surfactant isotherm tends to reach a plateau at some threshold surfactant concentration, which is termed as the Critical Micelle Concentration (CMC). Since the injected surfactant concentration is often 100 times or more than the CMC, a Langmuir-

type isotherm is suitable to represent the adsorption process. This isotherm is characterized by salinity, surfactant concentration and permeability, as shown in Eqs. (2.6) (Delshad et al. (1996)). In this model, adsorption is irreversible with respect to concentration whereas it is reversible with salinity.

$$\hat{C}_n = \min \left(C_n, \frac{a_3 (C_n - \hat{C}_n)}{1 + b_3 (C_n - \hat{C}_n)} \right). \quad (2.5)$$

$$a_3 = (ad_{31} + ad_{32} C_{sep}) \left(\frac{k_{ref}}{k} \right)^{0.5} \quad (2.6)$$

where C_n is total concentration of nanofluids, \hat{C}_n is adsorbed concentration of nanofluids, C_{sep} is effective salinity and k_{ref} is reference permeability, while ad_{31}, ad_{32}, b_3 are input parameters in the simulation.

2.2.3 Procedure for Modeling Wettability Alteration in Simulations

Wettability is significant in defining the fluid saturation and their distribution in the pore spaces of the reservoir rocks. Wettability is not directly related to determine the saturation state of the reservoir, instead it modulates the preference of the rock surface for wetting by a particular reservoir fluid. The wettability of the reservoir rock is dependent on the properties of the deposited minerals on their surfaces that have the capability to govern the location, flow and distribution of the reservoir fluids. Wettability alteration leads to changing the relative permeability and capillary pressure of the reservoir to enhance the oil recovery.

Wettability alteration is modeled by varying the relative permeability and the capillary pressures because the residual phase saturation values are influenced by oil mobilization due to wettability alteration, which in turn affects the relative permeability (Delshad et al. (2006)). In addition, capillary imbibition promotes recovery as the wettability is altered towards water-wet conditions. Therefore, the relative permeability and capillary pressure curve can be determined by interpolation using the initial and final wetting states (Eqs. (2.8) and Eqs. (2.9)). For instance, an initial wetting state can be an oil-wet system and a final wetting state can be represented as a water-wet system. As mentioned before, since the level of adsorption determines the degree of wettability alteration, the amount of adsorbed concentration of nanoparticles is associated with the scaling factor ω (Wettability Alteration Parameter) for interpolation (Eqs. (2.10)). The multiphase relative permeability is modeled with the Corey-type function with the endpoint and exponent (Eqs. (2.11)). The scale of Brooks-Corey type capillary pressure is changed with the interfacial tension (Eqs. (2.15)) (Delshad et al. (1996)).

$$k_{rl} = \omega k_{rl}^{final} + (1 - \omega) k_{rl}^{initial}, \quad (2.7)$$

$$P_C = \omega P_C^{final} + (1 - \omega) P_C^{initial}, \quad (2.8)$$

$$\omega = \frac{\hat{C}_n}{C_n + \hat{C}_n}, \quad (2.9)$$

where k_{rl} is relative permeability for phase l and P_C is capillary pressure.

$$k_{rl} = k_{rl}^o S_{nl}^{n_l}, \quad (2.10)$$

where k_{rl}^o is relative permeability endpoint, n_l is relative permeability exponent and S_{nl} is normalized saturation for phase l as follows:

$$k_{rl}^o = k_{rl}^{o^{low}} + \frac{S_{l'r}^{low} - S_{l'r}}{S_{l'r}^{low} - S_{l'r}^{high}} \left(k_{rl}^{o^{high}} - k_{rl}^{o^{low}} \right), \quad (2.11)$$

$$n_l = n_l^{low} + \frac{S_{l'r}^{low} - S_{l'r}}{S_{l'r}^{low} - S_{l'r}^{high}} \left(n_l^{high} - n_l^{low} \right), \quad (2.12)$$

$$S_{nl} = \frac{S_l - S_{l'r}}{1 - \sum_{l=1}^3 S_{l'r}}, \quad (2.13)$$

where $S_{l'r}$ is the residual phase saturation.

$$P_C = P_{COW} \frac{\sigma_{om}}{\sigma_{ow}}. \quad (2.14)$$

$$P_{COW} = C_{pc} (1 - S_{nl})^{E_{pc}} \quad (2.15)$$

where C_{pc} is the capillary pressure endpoint and E_{pc} is the capillary pressure exponent.

2.3 Applications

In this section, we demonstrate applications of the wettability alteration using nanofluids in tight oil reservoirs with multiple hydraulic fractures. Three synthetic reservoir models have been built to show the feasibility of wettability alteration in

unconventional reservoirs where each of cases has different hydraulic fracture geometry from planar to complex fractures.

2.3.1 Case 1: Simple Planar Hydraulic Fractures

We first present a synthetic tight oil reservoir model stimulated by multiple hydraulic fractures. The size of the model is 1000 ft, 928 ft, and 110 ft along x, y, and z direction respectively, consisting of 50×50×11 grid blocks. There is one horizontal well in the middle with a length of 688ft. In this model, one stage of hydraulic fracturing has been performed with four clusters where each of the clusters has half-length of 180 ft, 300 ft, 280 ft and 180 ft respectively. The horizontal matrix permeability is 0.015 md. Vertical permeability is 0.1 times the horizontal permeability. In the hydraulically fractured grid, the permeability is 100 md, which results in the fracture conductivity of 200 md-ft. In order to consider the area stimulated by hydraulic fractures, a Stimulated Reservoir Volume (SRV) region has been included with the increased permeability of 0.175 md (Figure 2.2). In this example, hydraulic fractures are represented by an elliptical plane and SRV regions are considered by ellipsoidal shape. Initial reservoir pressure at the depth of 9000 ft is 7000 psi. Table 2.1 summarizes the key properties of the reservoir.

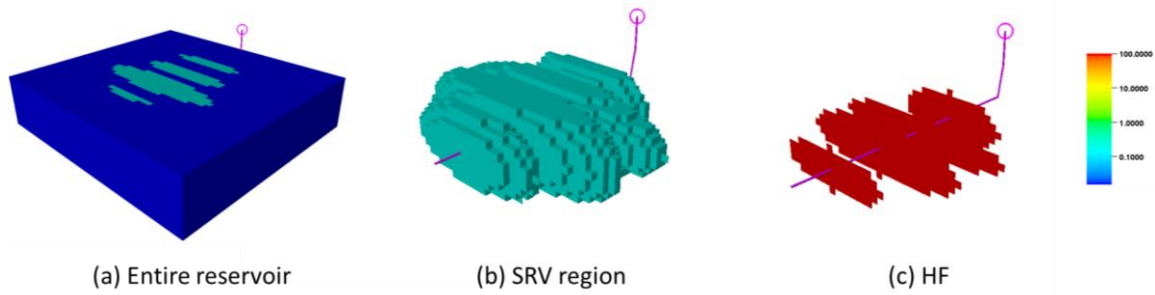


Figure 2.2 Permeability distribution in x direction (a) entire reservoir, (b) SRV region and (c) hydraulic fractures (reprinted with permission from Jung et al. 2018)

Table 2.1 Reservoir properties (reprinted with permission from Jung et al. 2018)

Reservoir properties		
Reservoir dimension	(ft)	1000 × 928 × 110
The number of grid block		50 × 50 × 11
Depth	(ft)	9000
Initial pressure	(psi)	7000
Matrix properties		
Porosity	(fraction)	0.1
Permeability	(md)	0.015
k_v/k_h	(fraction)	0.1
EPA	(md)	0.175
Initial water saturation	(fraction)	0.14
Fracture properties (4 fractures)		
Half Length	(ft)	180, 300, 280, 180
Width	(ft)	2
Porosity	(fraction)	0.3
Permeability	(md)	100
Initial water saturation	(fraction)	0.65

In addition, the set of important parameters for modeling the wettability alteration is shown in **Table 2**, followed by the graphs of relative permeability and capillary pressure for each wettability condition (Figure 2.3 and Figure 2.4). The relative permeability and capillary pressure parameters in the model were based on the results derived from the previous reports in the literature (Masalmeh (2002)) and also based on the simulation of

chemical flooding which included the effects of reservoir wettability (Anderson (2006)).

Table 2.2 summarizes corresponding parameters.

Table 2.2 Key parameters for wettability alteration (reprinted with permission from Jung et al. 2018)

Parameters	Symbol	Oil-wet		Water-wet	
		Water	Oil	Water	Oil
Residual saturation	S_{lr}	0.1	0.2	0.1	0.3
Relative permeability endpoint	k_{rl}^o	water	0.8	Water	0.1
		Oil	0.3	Oil	0.9
Relative permeability exponent	n_l	Water	3	Water	4.5
		Oil	5	Oil	2.5
Capillary pressure endpoint	C_{pc}	-2		6	
Capillary pressure exponent	E_{pc}	6		2	

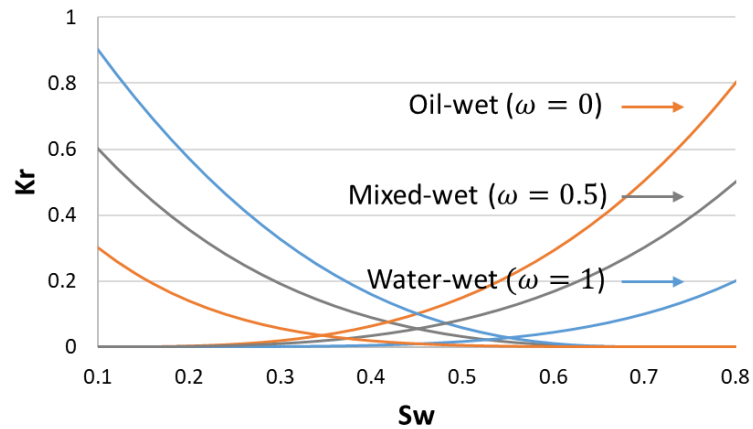


Figure 2.3 Relative permeability of oil and water for each wettability condition

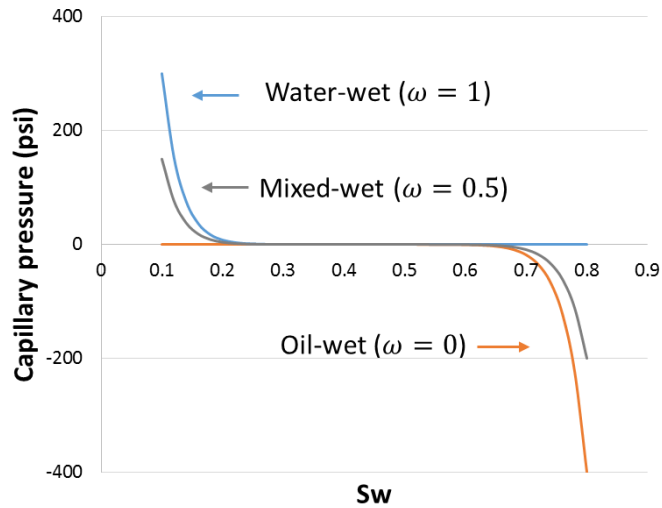


Figure 2.4 Capillary pressure curve for each wettability condition

2.3.2 The Effect of Wettability Alteration on Enhanced Oil Recovery

Figure 2.5 shows the effectiveness of wettability alteration through the injection of surfactant based nanofluids. After the 1000 days of primary depletion with the constant bottomhole pressure of 500 psi, we start injection with surfactant based nanofluids for 200 days and shut-in the well for 100 days. Injection has been constrained at the rate of 1.7% PV/year with 2% of surfactant concentration (volume fraction). During the injection period, wellbore block pressure was not allowed to exceed the initial reservoir pressure of 7000 psi (Figure 2.5). The oil-wet system has been altered toward more water-wet by injecting surfactant-based nanofluids followed by 100 days of soaking time. As a result, follow-up production for 1200 days results in additional 0.6% of oil recovery.

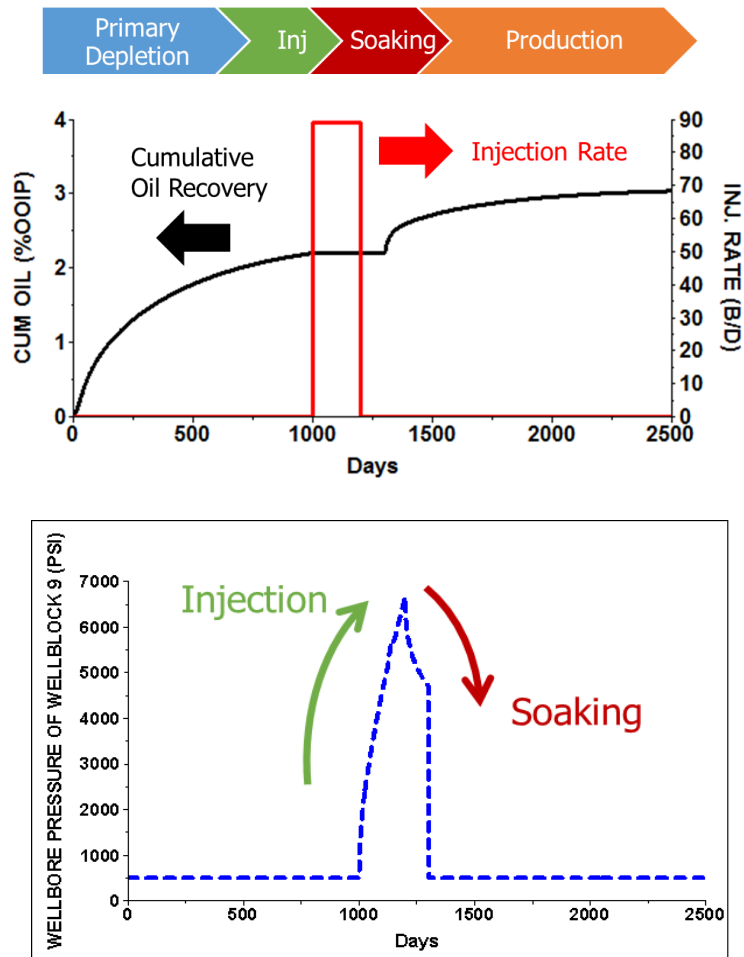


Figure 2.5 Cumulative oil recovery and injection rate (Top) and wellbore block pressure (Bottom) (reprinted with permission from Jung et al. 2018)

The comparison of the simulation results for cumulative oil recovery between the cases with and without surfactant injection are presented in Figure 2.6. The figure shows incremental oil production by the effect of wettability alteration. In the case without surfactant, we have simulated pressure depletion with the same bottomhole pressure constraint of 500 psi throughout the whole simulation time. After the first primary depletion, there is practically no difference with respect to cumulative oil recovery. However, the case with surfactant injection shows better performance in terms of not only

cumulative oil recovery but also a faster production rate. It gives about 0.6% more oil recovery. Even though the above results do not show significant increase in oil recovery, the full benefit of injecting surfactant-based nanofluids can be realized once we have more number of cycles, which include multiple injection, soak and production periods. Furthermore, if more realistic reservoir models with several hundred hydraulic fractures are considered, the impact of incremental oil production would be more substantial.

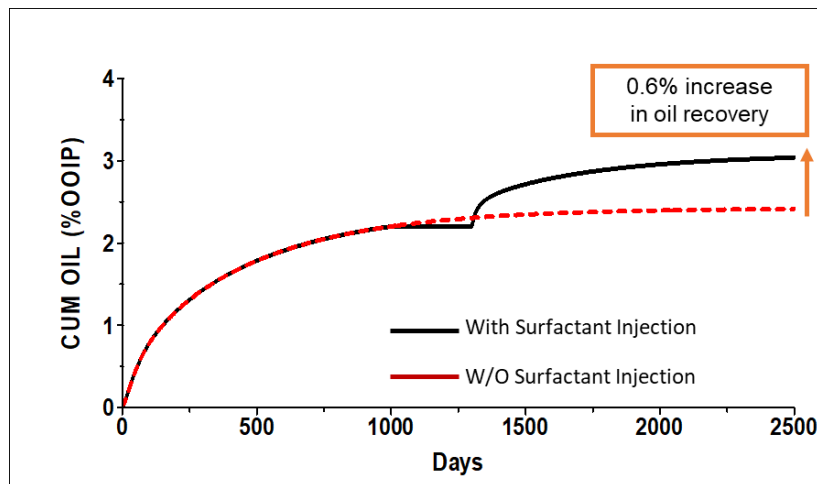


Figure 2.6 Comparison of cumulative oil recovery with and without surfactant injection (reprinted with permission from Jung et al. 2018)

Distribution of oil saturation on the grid also indicates that more oil has been produced from the case with surfactant injection than without the surfactant (Figure 2.7). Initial and final oil saturation were compared. In the case with surfactant injection, oil saturation decreases, especially in the Stimulated Reservoir Volume (SRV) region. In addition, the adsorbed concentration of surfactant and the value of wettability alteration parameter (ω) at each grid has been shown in Figure 2.8. This figure can be used to

identify the degree of wettability change as a result of adsorption. It can be seen that the area where adsorption occurs corresponds to the grid blocks having higher value of Wettability Alteration Parameter.

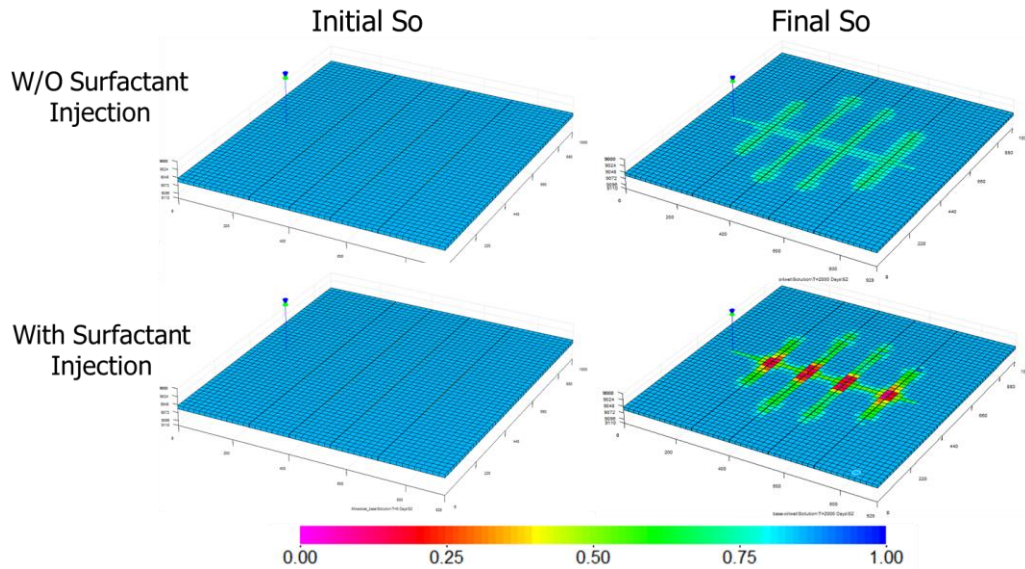


Figure 2.7 Comparison of initial and final oil saturation with and without surfactant injection (reprinted with permission from Jung et al. 2018)

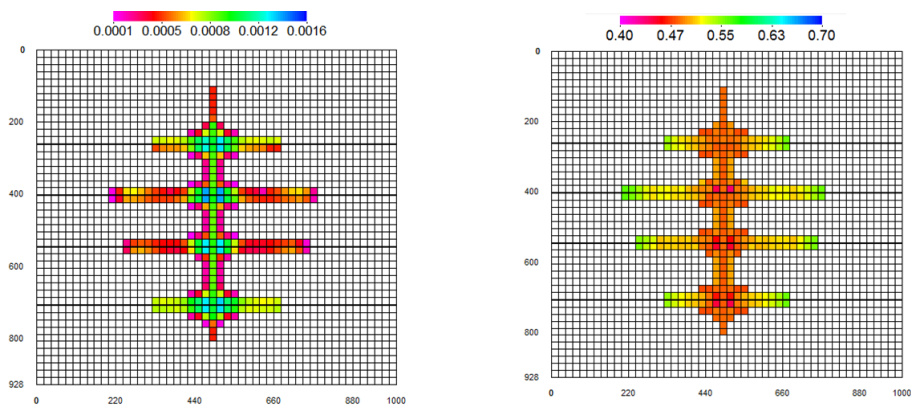


Figure 2.8 Adsorbed concentration of surfactant (left) and wettability alteration parameter (right) (reprinted with permission from Jung et al. 2018)

2.3.3 Sensitivity Analysis

To investigate the role of influential parameters in optimization of wettability alteration, a sensitivity study was performed. In this work, the effect of various parameters, such as slug size, soaking time, surfactant concentration and surfactant adsorption on the cumulative oil recovery was analyzed using numerical simulation. The ranges for each parameter are selected based on literature review. However, the upper bound of slug size has been restricted when the near-well bore block pressure reaches the maximum injection pressure. Maximum injection pressure is set to be around 8000 psi, based on fracture pressure gradient of 0.9 psi/ft. Table 2.3 summarizes the base as well as the low and high values for each parameter. For the adsorption parameter, corresponding surfactant adsorption curves are presented in Figure 2.9.

Table 2.3 Parameters and their range for sensitivity analysis (reprinted with permission from Jung et al. 2018)

	Uncertainty	Base	High	Low	Description
Slug size	$T_{injecting}$	200	270	50	Injection slug (days)
Soaking time	$T_{soaking}$	100	200	0	Soaking time (days)
Surfactant concentration	C_n	0.02	0.04	0.005	Total concentration of surfactant based nanofluids (volume fraction)
Surfactant adsorption	$ad31$	1.5	2.5	0.5	Surfactant adsorption parameters for Langmuir-type isotherm curve

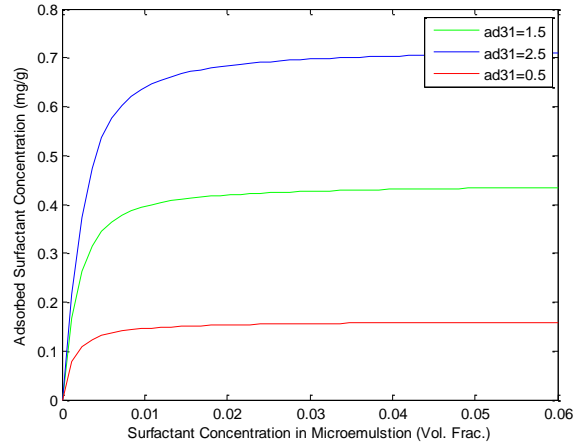


Figure 2.9 Surfactant adsorption curve (reprinted with permission from Jung et al. 2018)

To evaluate the relative impact of the parameters, a tornado chart is plotted by adjusting each parameter from the base model to the lower and upper extreme values (Figure 2.10). Dimensionless sensitivities are calculated as represented in Eqs. (2.17).

$$Sensitivity = \frac{Relative\ Difference\ in\ Objective\ Function}{Relative\ Perturbation\ in\ Parameters} = \frac{\Delta J / J}{\Delta x / x} \quad (2.17)$$

The parameter that has the widest relative change in cumulative oil recovery is the slug size. On the other hand, the results show that the impact of adjusting soaking time is almost negligible in terms of cumulative oil recovery. For the adsorption parameter, surfactant adsorption curve used in the sensitivity analysis is shown in Figure 2.9. Since the wettability alteration depends upon the level of adsorption, the simulation results were expected to be highly sensitive to the adsorption parameter. However, changes in the degree of adsorption show relatively low impact on the oil recovery. That is because surfactant injection is also associated with interfacial tension reduction, which causes the

mobilization of oil. Because of increased adsorption, surfactant concentration can fall below the level required to sustain the needed micellar solution for achieving low interfacial tension between oil and water. In other words, if large amounts of retention and relatively large amounts of adsorption of surfactant occurs, residual oil can be retrapped in the reservoir due to increased interfacial tension.

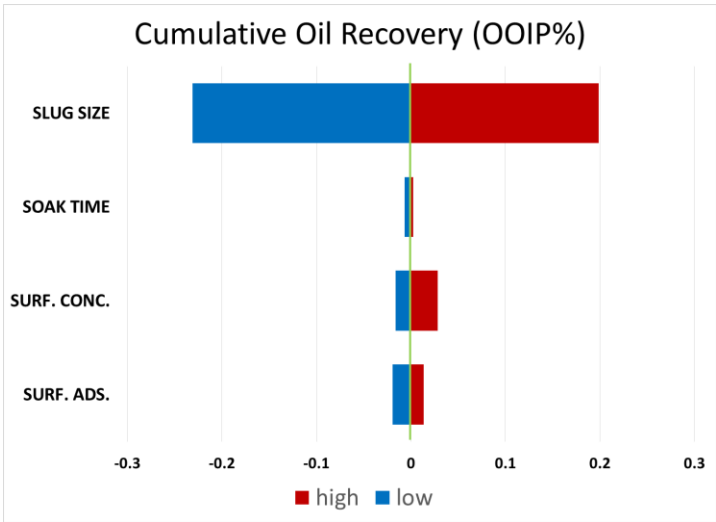


Figure 2.10 Tornado chart (reprinted with permission from Jung et al. 2018)

In Figure 2.11, oil relative permeability distribution from wettability alteration for a high adsorption case and a low adsorption case have been showed. We can see that as the adsorption increases, higher oil relative permeability is achieved. On the other hand, the difference in interfacial tension between the two cases shows some grid blocks having positive numbers, (Figure 2.12) indicating that high level of adsorption leads to an increase in interfacial tension and prevents oil from flowing in the reservoir. Adsorption level is one of the major uncertain parameters in the reservoir. Therefore, once a better

understanding of the behavior of this parameter is achieved through history matching, further optimization studies can be performed by varying both the wettability alteration and the interfacial tension as a function of surfactant concentration and slug size.

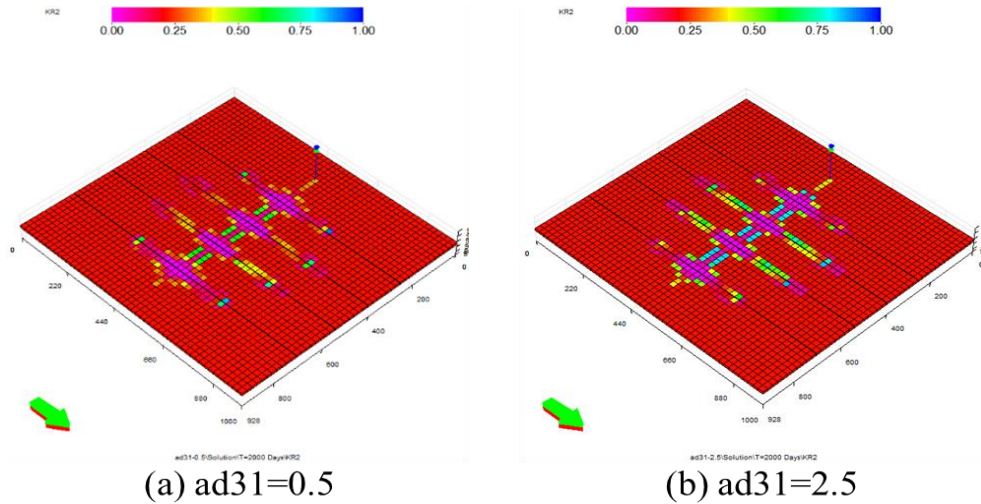


Figure 2.11 Oil relative permeability on grid (a) low adsorption (b) high adsorption (reprinted with permission from Jung et al. 2018)

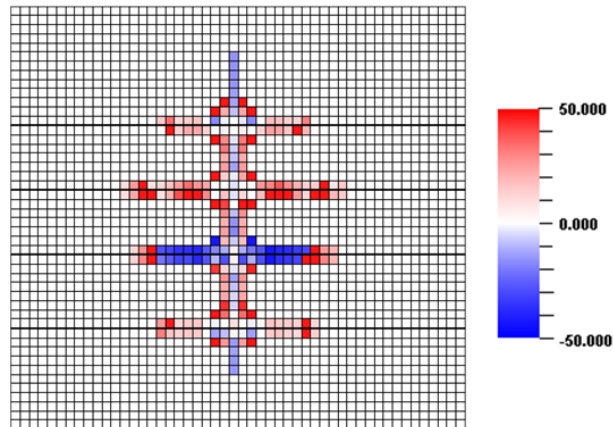


Figure 2.12 Interfacial tension difference between high adsorption and low adsorption

2.3.4 Multi-Objective Optimization

Sensitivity analysis has shown that oil production can be maximized by adjusting the slug size and surfactant concentration. A Pareto-based multi-objective optimization (Park et al. (2015)) has been performed for this purpose using a genetic algorithm. Instead of a conventional single-objective genetic algorithm, which aggregates all the objective functions into one scalar value, the multi-objective optimization allows for a trade-off among conflicting objectives. Therefore, this algorithm is well suited to simultaneously consider multiple conflicting objectives. In this example, the goal is to maximize oil production while minimizing the usage of chemicals through the optimization process. Two objective functions, which are incremental oil production (ΔN_p) and surfactant utility factor (UF) respectively, are defined as shown in Eqs. (2.18) and Eqs. (2.19). While the incremental oil production represents the amount of oil that can be produced through injecting surfactant, the utility factor quantifies the efficiency of the injected chemical to improve oil recovery. Increasing surfactant concentration shows high utility factor as well as incremental oil recovery, a conflict between the two objectives (Figure 2.13). Low utility factor is desirable whereas incremental oil recovery needs to be maximized.

$$\Delta N_p = N_p (\text{with surfactant}) - N_p (\text{Do nothing}). \quad (2.18)$$

$$UF = \frac{\text{surfactant required} (ft^3)}{x \text{ STB of incremental oil}} \quad (2.19)$$

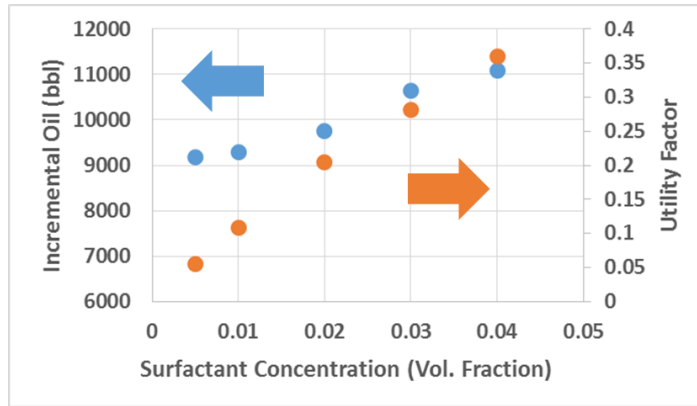


Figure 2.13 Conflicting performance between two objectives with increasing surfactant concentration (reprinted with permission from Jung et al. 2018)

Figure 2.14 shows the performance of the multi-objective optimization. After 6 generations with a population of 70 members per generation, the initial population has reached a Pareto-front, which indicates a set of optimal solutions considering the two objective functions. Depending on the importance of each objective function, optimal solutions can be divided into three clusters. Figure 2.15 has been generated through the cluster analysis using the k-Means clustering. A set of optimized models from the cluster 1, which represents low utility factor as well as low incremental oil recovery, have not only low surfactant concentration but also small slug size. On the other hand, models in the cluster 3 have higher surfactant concentration that is greater than that of the base case. Note that, most of the models from the cluster 2 and the cluster 3 have large slug size, which almost reach the upper bound. The models in cluster 2 represent the optimal combination of high incremental recovery and low surfactant usage. In addition to the comparison of objective function, the range of parameters that has been adjusted through the optimization has been presented in Figure 2.16. In the initial generation, both the

parameters are evenly distributed within the given ranges. However, as a result of optimization process, the distribution of surfactant concentration has been shifted with a median of 1% and the range of slug size has been significantly reduced.

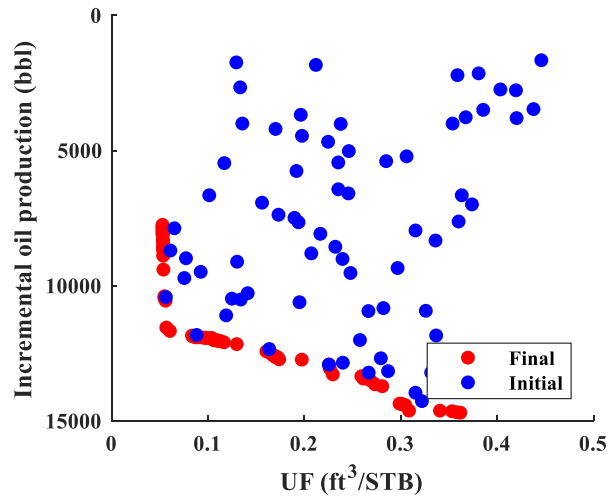


Figure 2.14 Multi-objective optimization results: Comparison between initial generation and final generation (reprinted with permission from Jung et al. 2018)

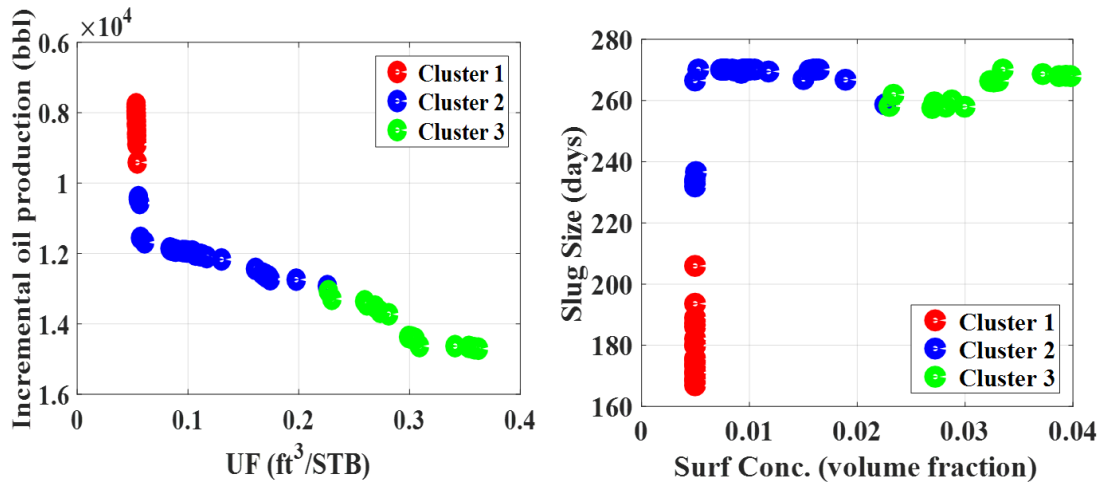


Figure 2.15 Cluster analysis: objective functions (left) and distribution of parameters (right) (reprinted with permission from Jung et al. 2018)

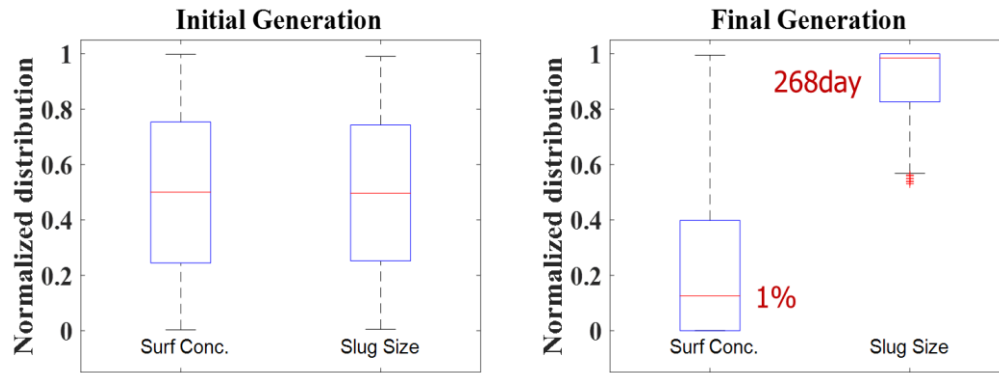


Figure 2.16 Comparison of the distribution of parameters: Initial generation (left) and Final generation (right) (reprinted with permission from Jung et al. 2018)

Box plots in Figure 2.16 are able to show how the range of control variables is largely reduced in comparison with initial generation and imply that optimal solutions tend to have lower surfactant concentration with larger slug size. The shape of histogram in Figure 2.17 also confirms that lower concentration and more injection duration have a positive impact on not only incremental oil recovery but also efficient utilization of chemicals. However, the spread of control variables for each cluster that is generated through the cluster analysis is also investigated to see the difference depending on the importance of objective functions. Each group has a distinct characteristic compared to the others for both parameters. First, it is noticed that achieving higher oil recovery with low utility factor results from low surfactant concentration combined with longer injection duration (Figure 2.18). Second, models that keep minimal usage of surfactant as well as poor incremental oil production prefers small slug size with low concentration, which can result in less amount of adsorption (Figure 2.19). On the other hand, a third group indicating high oil gain have a tendency to be in a higher range of surfactant concentration

compared with the base case (Figure 2.20). Not only that, it requires longer injection duration, which leads to more wettability alteration in the reservoir.

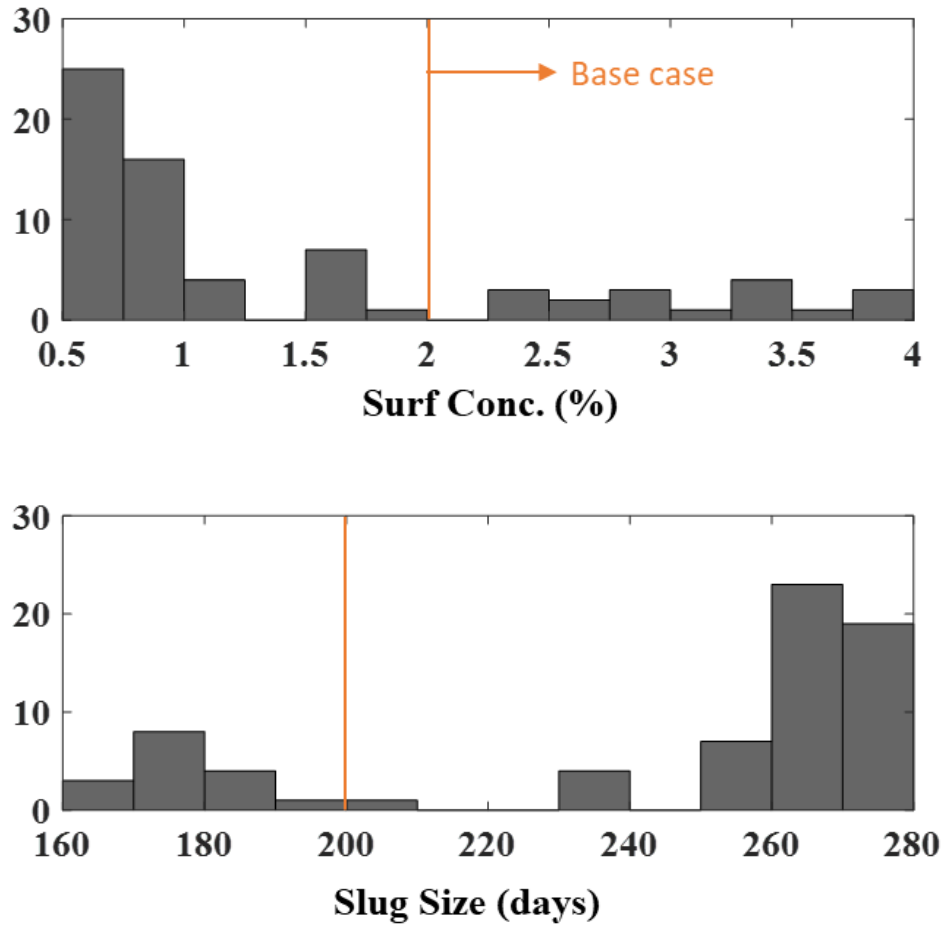


Figure 2.17 Histogram of control variables in final generation: Surfactant concentration (top) and Final generation (bottom)

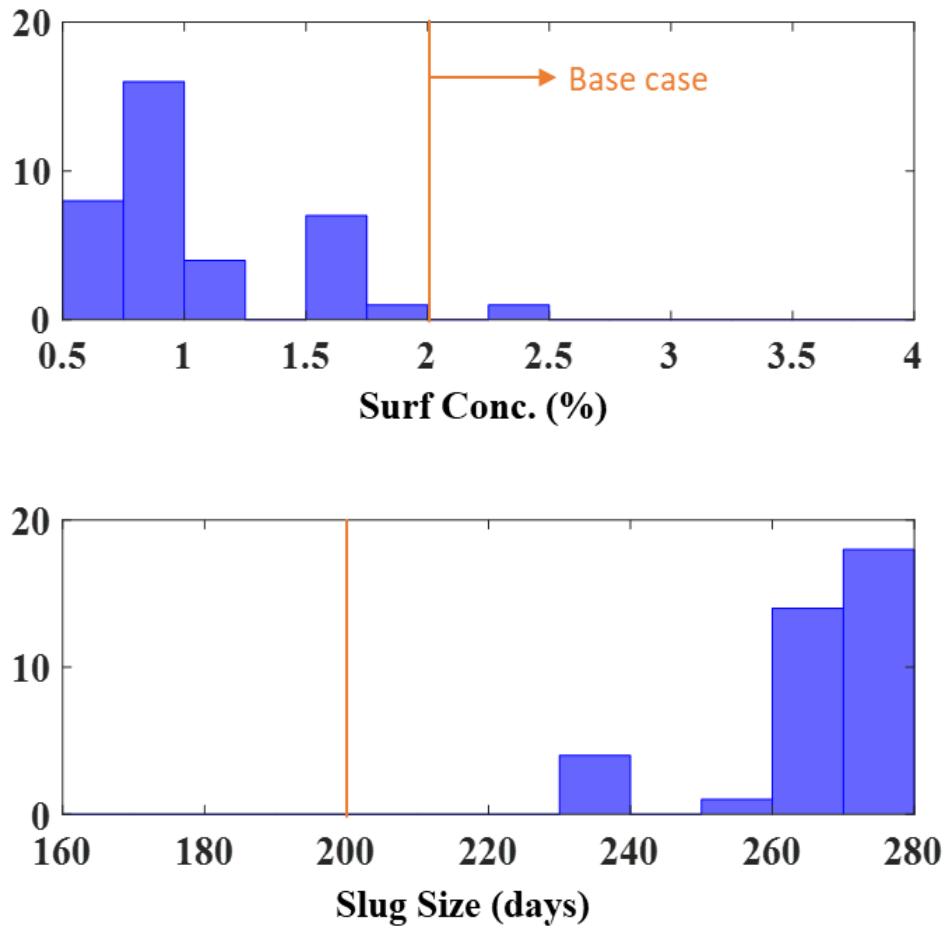


Figure 2.18 Histogram of control variables in optimal group: Surfactant concentration (top) and Final generation (bottom)

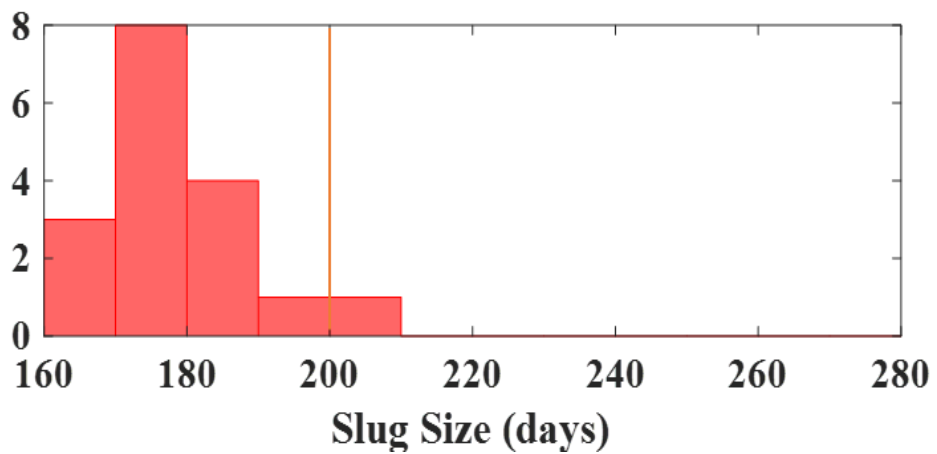
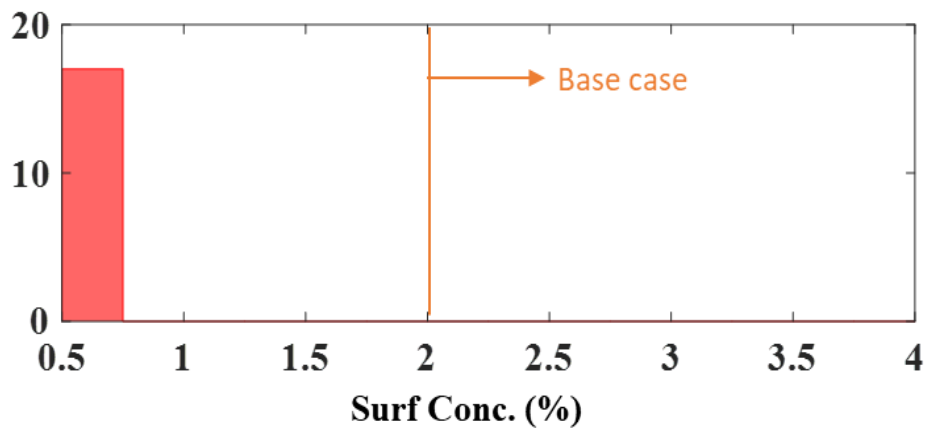


Figure 2.19 Histogram of control variables in low UF group: Surfactant concentration (top) and Final generation (bottom)

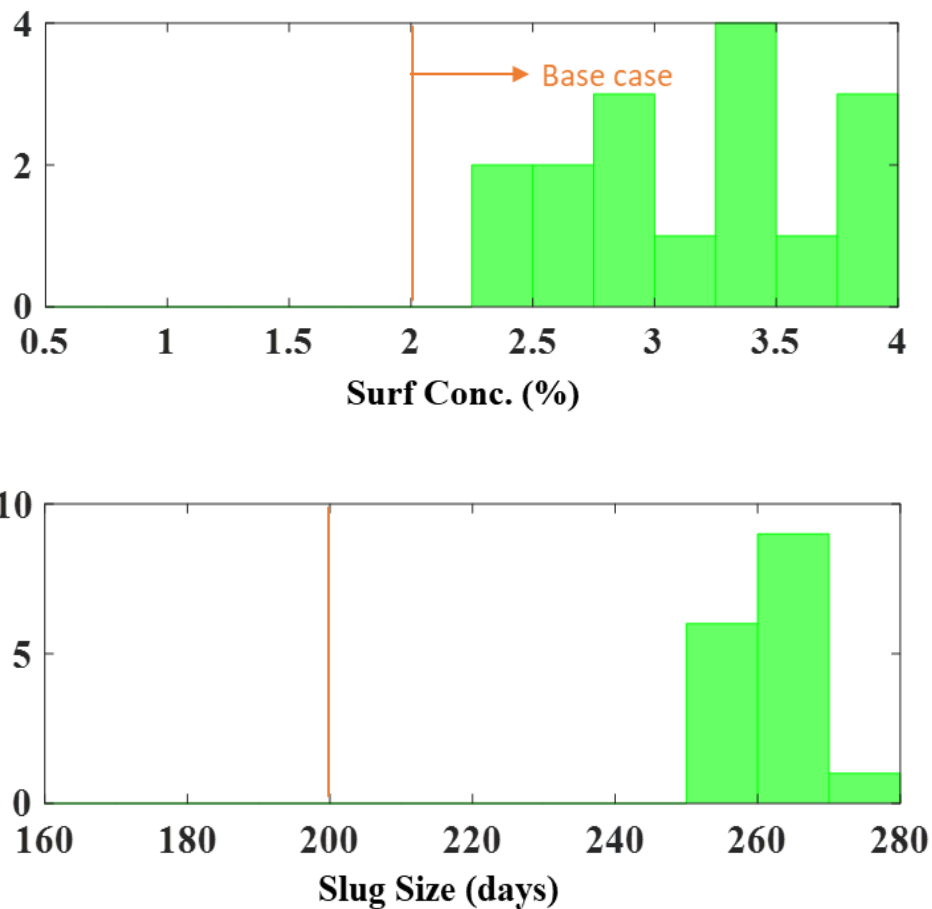


Figure 2.20 Histogram of control variables in high oil gain group: Surfactant concentration (top) and Final generation (bottom)

2.3.5 Case 2: Multiple-stage Planar Hydraulic Fractures

In this section, we demonstrate the wettability alteration through a synthetic case with multiple-stage hydraulic fractures. The reservoir model has 58,500 grid cells (225×52×5) grid blocks in x, y and z direction and the reservoir domain size is 1080'×410'×50'. In addition, it contains one horizontal well with three stages of hydraulic fractures, which has five clusters per stage (Figure 2.21). The geometry of hydraulic fractures is uniform with a fracture half-length of 150 ft and a fracture spacing of 60 ft.

The horizontal matrix permeability is 0.015 md. In the hydraulically fractured grid, the permeability is 10 md, which leads to a fracture conductivity of 20 md-ft. Other than the reservoir and hydraulic fracture properties, the parameters associated with the wettability alteration are identical to the previous application, such as relative permeability and capillary pressure. Total simulation time is 900 days.

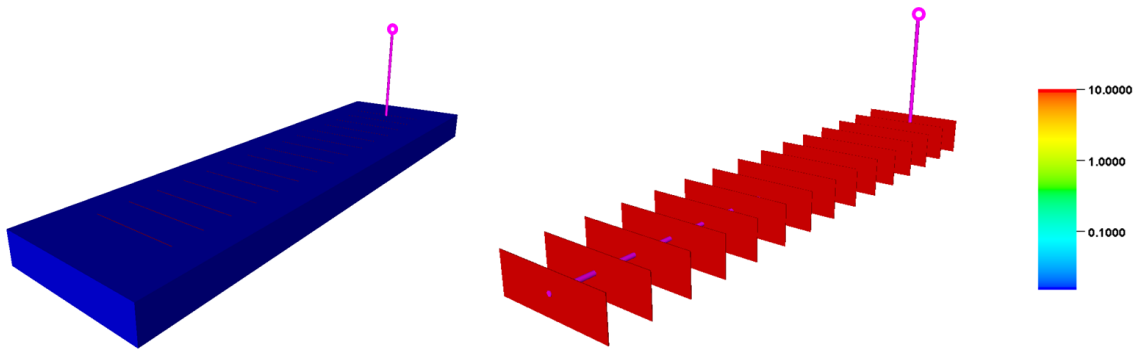


Figure 2.21 Permeability distribution of matrix and hydraulic fractures (reprinted with permission from Jung et al. 2018)

The process of applying surfactant-based nanofluids is the same as the previous application. We start with primary depletion (300 days), followed by the injection (200 days) and the soaking period (100 days) and eventually simulate a second pressure depletion with a constant bottomhole pressure (300 days). Bottomhole pressure of 500 psi is used as a constraint during the production period whereas injection is controlled by injection rate of 4.2% PV/year with 2% of surfactant concentration (volume fraction). Figure 2.22 shows the oil production rate and cumulative oil recovery by comparing the results with those from the ‘Do Nothing’ case, which only simulates primary depletion for the total simulation time. As a result of injecting surfactant-based nanofluids, the initially

oil-wet system has been altered toward more water-wet, which allows production for 300 days to have additional 1.6 % oil recovery.

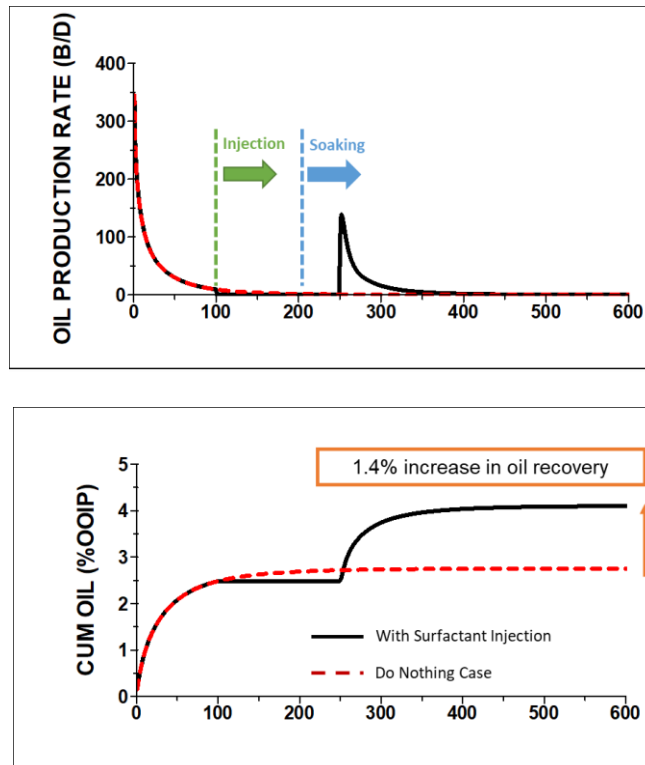


Figure 2.22 Oil production rate (top) and cumulative oil recovery (bottom) (reprinted with permission from Jung et al. 2018)

2.3.6 Case 3: Complex Hydraulic Fractures

In this last application, we present an example with complex hydraulic fracture geometry and natural fractures to show the effectiveness of the wettability modification. Except for the geometry of hydraulic fractures and the size of the model, other reservoir properties and parameters for wettability alteration are the same as previous examples because our focus here is to show the applicability of wettability alteration for different

conditions of hydraulic fractures. The reservoir consists of 218×115×5 grid blocks (0.13 million cells) with a model dimension of 436' × 230' × 50' (Figure 2.23). Two sets of Discrete Fracture Network (DFN) of natural fractures are generated based on the statistical properties shown in Table 2.4. The hydraulic fracture propagation is simulated by a commercial software (MANGROVE[®]) and in this particular example, a pumping schedule representative of Eagle Ford is used as presented in Marongju-Porcu et al. (2016). For simplicity, one stage of hydraulic fracture with five clusters has been generated. While generating one stage of hydraulic fractures with the spacing of 50 ft, the 20/40 proppant with cross-linked gel is used. As summarized in

Table 2.5, hydraulic fracturing treatment starts with slick water and subsequently proppant is injected with cross-linked gel fluid.

Table 2.4 Statistical properties of natural fractures (reprinted with permission from Jung et al. 2018)

Natural Fracture 1	Average	Standard Deviation
Length (ft)	100.0	10.0
Orientation (deg)	60.0	10.0
Spacing (ft)	100.0	10.0
Natural Fracture 2	Average	Standard Deviation
Length (ft)	50	10
Orientation (deg)	150	10
Spacing (ft)	100	10

Table 2.5 Pumping schedule summary (reprinted with permission from Jung et al. 2018)

Fluid Type	Pump Rate (bpm)	Fluid Volume (gal)	Proppant	Proppant Conc. (PPA)	Prop. Mass (lb)
Slick water	10	300	-	-	-
Slick water	50	500	-	-	-
30# X-linked gel	50	800	-	-	-
30# X-linked gel	50	300	20/40 sand	0.50	150

30# X-linked gel	50	300	20/40 sand	0.75	225
30# X-linked gel	50	300	20/40 sand	1.00	300
30# X-linked gel	50	300	20/40 sand	1.50	450
30# X-linked gel	50	300	20/40 sand	2.00	600
30# X-linked gel	50	300	20/40 sand	2.50	750
30# X-linked gel	50	300	20/40 sand	3.00	900
30# X-linked gel	50	300	20/40 sand	3.50	1050
30# X-linked gel	50	300	20/40 sand	4.00	1200
30# X-linked gel	50	300	20/40 sand	4.50	1350
Flush	50	String Volume	-	-	-

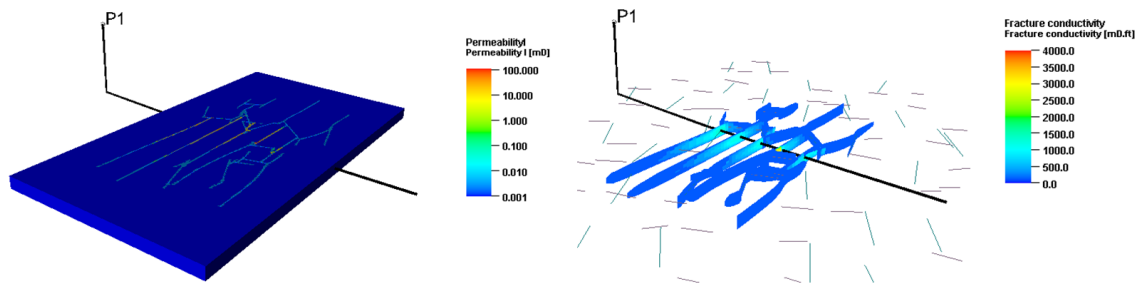


Figure 2.23 Permeability distribution (Left) and conductivity of hydraulic fractures (Right) (reprinted with permission from Jung et al. 2018)

Figure 2.24 shows the comparison of oil production rate and cumulative oil recovery between a surfactant injection case and a ‘Do Nothing’ case. Again, we repeat the same procedure as explained in the previous examples, such as primary depletion, injection period, soaking period and subsequent production. By injecting surfactant-based nanofluids at the rate of 3.5% PV/year and with a surfactant concentration of 2%, an additional 1.0% increase in oil recovery has been achieved at the end of the secondary production period.

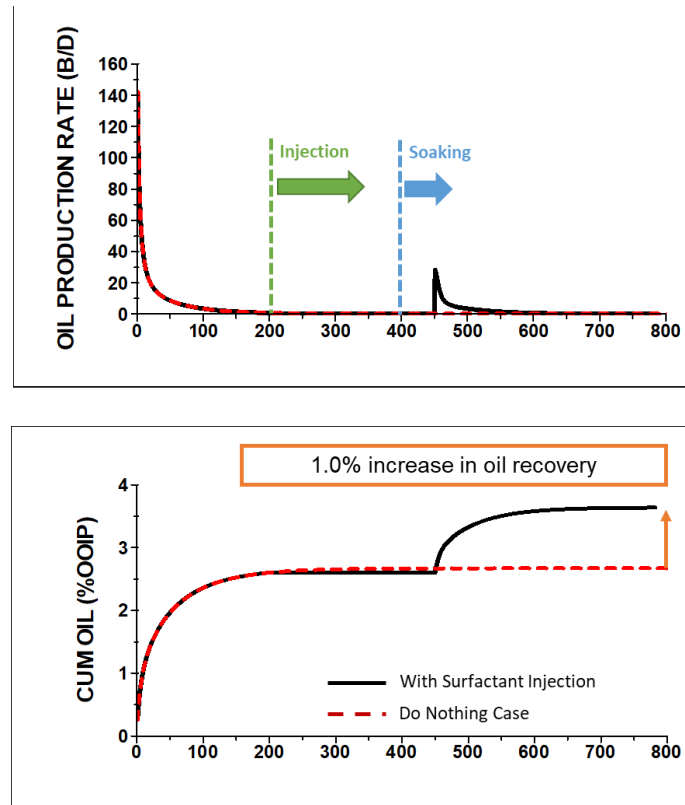


Figure 2.24 Oil production rate (top) and cumulative oil recovery (bottom) (reprinted with permission from Jung et al. 2018)

2.4 Sensitivity Studies

In the previous section, primary production duration was determined when there is almost no more increase in oil recovery by reservoir pressure depletion. Subsequently, surfactants are applied to exploit the rest of oil trapped in the tight formations. However, those selected injection timing may not be preferred from the economic point of view. Therefore, the effect of various injection timing on the oil recovery will be discussed in this part.

In addition, different relative permeability for each wettability condition will be investigated because incremental oil recovery by surfactant injection strongly depends on

the initial and final relative permeability that we specify in the beginning. In the following section, smaller endpoint changes between oil-wet and water-wet system will be considered to demonstrate the feasibility of wettability changes through surfactant injection.

For both sensitivity studies, we used the same reservoir model as Case 1 with simple planar type of hydraulic fractures. However, relative permeability curves and duration of primary depletion are adjusted respectively for each corresponding sensitivity study.

2.4.1 Effect of Different Injection Timing

Primary production duration of the base case was 1000 days. In this section, two other cases are compared, which are Case (a) with 500 days of duration and Case (b) with 300 days of duration respectively. As shown in Figure 2.25, the difference of cumulative oil recovery between all three cases are almost negligible at the end of simulation. However, as we begin with surfactant injection earlier, faster production rate can be achieved, which enable us to perform EOR method more economically. Figure 2.26 shows that there has been similar degree of wettability alteration by observing the amount of adsorbed surfactant in the reservoir. Since all other parameters are set to be identical except for the timing of surfactant injection, the level of adsorption for both Case (a) and Case (b) is equal to the base case. Therefore, it seems appropriate to select early injection timing, considering efficient reservoir management. However, one of the assumptions that we specified in this study is that there is a maximum injection pressure, which is typically

regarded as one of the operational parameters. Although the Case (b) with shorter primary production duration indicates better performance in terms of faster production rate, Figure 2.27 shows that it exceeds the maximum injection pressure. Taking this factor into account, Case (b) would not perform better because the amount of injected surfactant will be smaller than the other cases, which results in less change in wettability. Optimal injection timing needs to be investigated depending on operational parameters during injection.

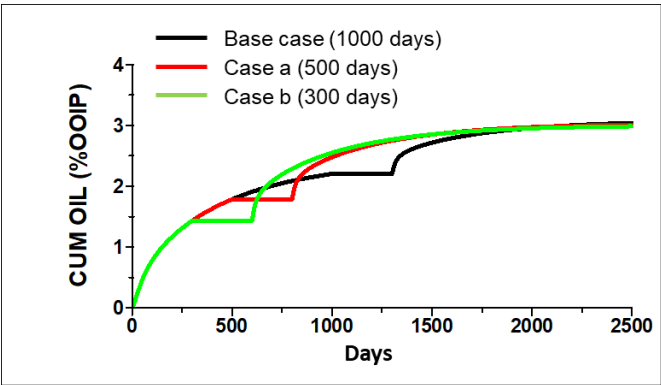


Figure 2.25 Comparison of cumulative oil recovery

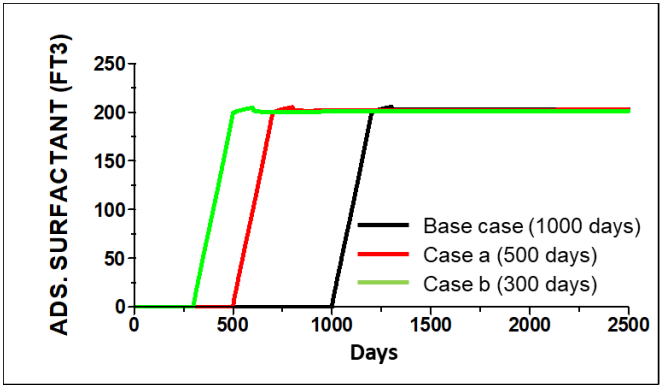


Figure 2.26 Comparison of the amount of adsorbed surfactant

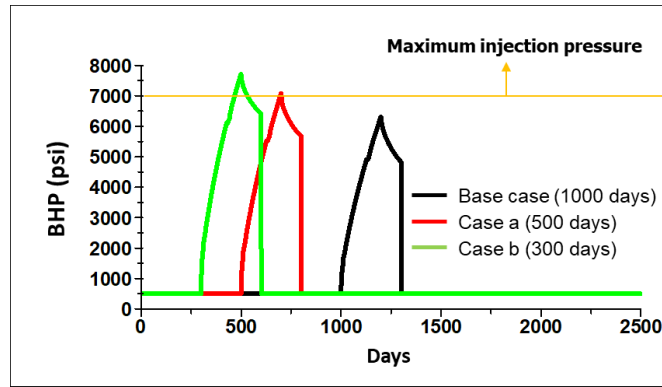


Figure 2.27 Comparison of bottomhole pressure

2.4.2 Effect of Different Relative Permeability

Effect of wettability alteration on incremental oil recovery is highly dependent upon the relative permeability curves for each wettability system. In the previous application shown in Section 2.3, endpoint for oil and water relative permeability was quite different between oil-wet and water-wet systems, leading to significant influences on the oil recovery due to the wettability changes. In this part, another example of relative permeability (Figure 2.28) is studied where the endpoint between each wettability condition is closer than the previous application in Figure 2.3.

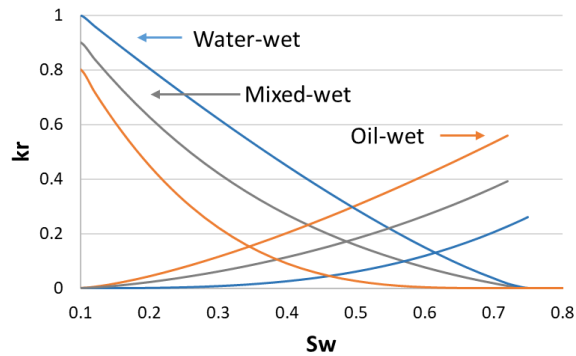


Figure 2.28 New relative permeability

In Figure 2.29, the oil recovery from the primary production by reservoir pressure depletion increases, compared to the previous application (Case 1). Subsequently, incremental oil production after surfactant injection period also decreases, which indicates less effective performance of using surfactant for wettability alteration. However, as examined in the section 2.7.1 regarding the timing of injection, wettability change still has a positive impact on incremental oil recovery with shorter primary production time (Figure 2.30).

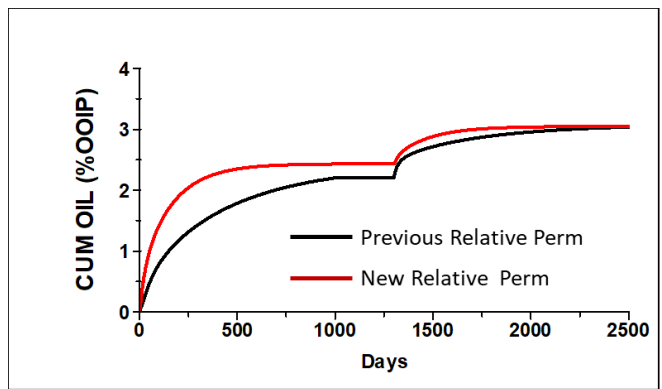


Figure 2.29 Comparison of cumulative oil production between different relative permeability

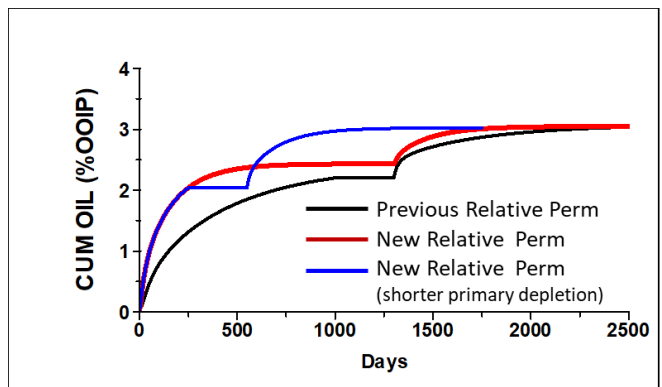


Figure 2.30 Effect of shorter primary depletion duration on the oil recovery

2.5 Conclusions

The applications of nanofluids can provide a technologically advanced solution for EOR to counter the problem of the rapid production decline of unconventional wells. Various research groups have reported the use of nanofluids as a useful tool for EOR purposes in the laboratory, but it is vital to establish their use and optimize their performance in the field scale as well. Nanofluids are expected to play a significant role in enhanced oil recovery with the capability of altering the wettability of rocks, especially in tight formations.

- In this chapter, applications to tight oil reservoirs have been established as a potential technique for wettability alteration using surfactant based nanofluids in the field scale. Even though the primary depletion in tight oil reservoirs drops rapidly due to the low matrix permeability, surfactant based nanofluids can be used successfully to change the wettability from oil-wet to more water-wet. As a result, the capillary pressure and the relative permeability are changed, which eventually contribute to additional oil recovery.
- By performing a sensitivity analysis, the major influential parameters and the fewer sensitive parameters were identified. The observed behavior in the numerical simulations that the adsorption parameter does not significantly affect the oil recovery beyond the threshold can be explained by accounting for the balancing effects of interfacial tension.
- A multi-objective optimization to not only maximize oil recovery but also minimize the chemical usage was carried out by adjusting slug size and surfactant

concentration. From a set of optimal solutions, the guidance for chemical injection can be suggested for field applications. Finally, the applicability of the chemical EOR process through wettability alteration is demonstrated for reservoirs with complex hydraulic fractures and natural fractures.

CHAPTER III
MULTI-WELL EXTENSION AND APPLICATION OF FAST MARCHING
METHOD (FMM) TO FIELD EXAMPLES: HANSENS FIELD

3.1 Chapter Summary

The simulation of multiphase flow in unconventional reservoirs is a challenging problem but it is often required due to the limitation of analytical solutions. This flow simulation involves not only horizontal wells with complex geometry of hydraulic fractures, but also complicated flow mechanisms between reservoir formations, natural fractures and hydraulic fractures. As a result, a high-resolution simulation plays an important role, which typically takes a substantial amount of computational time. However, because of excessive run time, it frequently prevents efficient reservoir management in a reasonable timeframe.

The prior research has utilized the concept of Fast Marching Method (FMM) to aid fast numerical simulation with the acceptable agreement of simulation results, compared to the commercial simulator. FMM is the efficient way to solve the Eikonal equation that governs the representation of pressure front propagation. Once the Diffusive Time of Flight (DTOF) is generated on the grid using FMM, the 3-D flow equation could be converted into the equivalent 1-D equation by using DTOF as a spatial coordinate. Since reservoir heterogeneities are already incorporated in DTOF, the 1-D flow equation improves the simulation runtime while it still reproduces the well performance of the original simulation models.

Although applications of FMM to single well cases have been widely investigated, there has been a limited research regarding the extension to multi-well cases. The ‘equal- τ ’ interface, where the pressure front marching from one well encounters the others (Huang 2017), determines drainage boundaries. After that, an individual 1-D simulation associated with each sub-domain is performed without communication between wells in the reservoir. This approach was able to show a good performance compared with original simulation models only if drainage partitions do not change significantly over time. Unfortunately, most of the time in actual field cases, drainage volume partitions are not constant due to the different operations of each well. Recently, Iino (2018) proposed a novel approach to account for dynamic change of drainage volume during simulation period using a concept of inter-partition transmissibility that allows for cross-flow between partitions. As a result, the FMM-based simulation is now in the form of 2-D models where each row in the model represents a 1-D simulation model corresponding to one well and an associated partition in the reservoir, and these 1D models are connected via Non-Neighbor Connection (NNC), which is the inter-partition transmissibility, if necessary. However, a multi-well FMM-based simulation using inter-partition transmissibility has not been applied to an actual field example yet.

In this chapter, the goal here is to demonstrate the advantages of the FMM-based flow simulation in terms of visualization of well drainage volume and computational efficiency. Furthermore, the application will be extended to multi-well simulation to investigate the feasibility of multi-well FMM to the real field example. The workflow for the calculation of inter-partition transmissibility has been improved and applied to the field

case. The results will be compared with a full 3-D simulation to demonstrate the power and utility of the inter-partition transmissibility method for multi-well FMM.

3.2 Background

During the past decade, unconventional reservoirs have been widely developed with the growing energy demand. The supply of energy from unconventional resources involves the improvement of technologies, such as horizontal wells and multi-stage hydraulic fractures (Alexander et al. 2011). However, it has been found that transport mechanisms in unconventional formation do not follow the conventional ones, which requires novel techniques to better understand their characteristics.

Previous studies for performance assessment of unconventional reservoirs have used the traditional numerical simulation to accurately account for not only reservoir heterogeneity but also interaction between fractures and reservoir rocks (Cipolla et al. 2011). Even though the conventional numerical simulations have the capability to evaluate all the relevant physics incorporating the complex fracture geometry (Cipolla et al. 2010a, 2010b; Diaz de Souza et al. 2012; Novlesky et al. 2011), there have been challenges with respect to a substantial amount of computational time, which hinders efficient reservoir management. As a result, a novel approach, which is able to consider complex physical mechanisms and perform rapid simulation simultaneously, is needed.

Recently, Fast Marching Method (FMM)-based 1-D simulation has been proposed for a rapid and efficient simulation for unconventional reservoirs. This approach is based on the concept of the depth of investigation that is further generalized to the Eikonal

equation using Diffusive Time of Flight (DTOF) to apply for heterogeneous reservoirs. The DTOF represents the travel time of pressure propagation (Datta-Gupta et al. 2011; Vasco and Datta-Gupta 2016) which embeds reservoir heterogeneity. Therefore, DTOF can be obtained on every grid by solving the Eikonal equation for the DTOF using FMM that is a class of front tracking algorithm (Sethian 1996; Sethian 1999).

The production profile from unconventional reservoirs can be characterized by the concept of radius of investigation that has been applied for homogeneous reservoirs (Datta-Gupta et al. 2011). Using the depth of investigation in Eqs. (3.1), the arrival time for the pressure to propagate a certain distance can be obtained.

$$r = \sqrt{\frac{4kt}{\phi\mu c_t}} \quad (3.1)$$

In heterogeneous reservoirs, the concept can be generalized by the ‘Eikonal’ equation that governs pressure front propagation by introducing the ‘Diffusive Time of Flight’ (Vasco and Datta-Gupta 2016). The Eikonal equation in Eqs. (3.2) results from a high frequency asymptotic solution of the diffusivity equation, which involves reservoir heterogeneity.

$$\sqrt{\frac{k(\mathbf{x})}{\phi(\mathbf{x})\mu c_t}} |\nabla\tau| = 1 \quad (3.2)$$

where $\alpha = k/\phi\mu c_t$ represents the diffusivity that is spatially varied and τ corresponds to DTOF.

Previous studies (Datta-Gupta et al. 2011; Xie et al. 2015; Zhang et al. 2016; Iino et al. 2017) show the feasibility of the Eikonal equation to the unconventional reservoirs where a high contrast has been observed in diffusivity between hydraulic fractures and formation. Fast Marching Method (FMM) is the efficient technique to solve the Eikonal equation for DTOF, which performs sequential calculation from the source outwards to find the shortest path (Sethian 1996; Sethian 1999; Hassouna and Frag 2007).

Once DTOF on each grid is calculated, the coordinate transformation based on DTOF from 3-D pressure diffusion equation to an equivalent 1-D equation can be performed. Mathematical details of the derivation can be found in previous works (Zhang et al. 2016; Fujita et al. 2016; Iino et al. 2017a, 2017b). Using Eqs. (3.3), the pressure diffusivity equation can be written as follows:

$$\frac{\partial(\rho\phi)}{\partial t} + \rho\tilde{q} = \frac{\phi_{ref}}{w(\tau)} \frac{\partial}{\partial \tau} \left[w(\tau) \rho \frac{(\mu c_t)_{ref}}{\mu} \frac{\partial p}{\partial \tau} \right] \quad (3.3)$$

where the sink/source terms are expressed in flow rate per unit bulk volume.

$w(\tau)$, which is introduced during the coordinate conversion, represents the derivative of pore volume with respect to DTOF as shown in Eqs. (3.4) and will be used in 1-D transmissibility calculation.

$$w(\tau) = \frac{dV_p(\tau)}{d\tau} \quad (3.4)$$

This chapter concentrates on the application of multi-well FMM-based 1-D simulation to an actual unconventional reservoir with a novel approach to account for dynamic changes in drainage partitions. First, we present the improved calculation of

inter-partition transmissibility and associated workflow. Next, we show the field case to demonstrate the efficiency of the newly proposed workflow.

3.3 Methodology

In this section, we present a mathematical formulation for single-porosity and blackoil system and a simulation workflow for the multi-well FMM-based simulation with the improved inter-partition transmissibility calculation.

3.3.1 Mathematical Formulation

In this chapter, we focused on the single-porosity and blackoil simulation for the multi-well FMM. As 3-D flow equations are decoupled into 1-D equations along the DTOF (Iino 2018), we obtain the following governing equations on the 1-D DTOF coordinate:

$$\frac{\partial}{\partial t} \left(\phi \frac{S_w}{B_w} \right) = \frac{\phi_{ref}}{w(\tau)} \frac{\partial}{\partial \tau} \left(w(\tau) \left(\frac{c_t}{\lambda_t} \right) \frac{k_{rw}}{B_w \mu_w} \frac{\partial p}{\partial \tau} \right) + \frac{\tilde{q}_w}{B_w} \delta(\tau_{wb}) \text{ (Water)}, \quad (3.5)$$

$$\frac{\partial}{\partial t} \left(\phi \frac{S_o}{B_o} \right) = \frac{\phi_{ref}}{w(\tau)} \frac{\partial}{\partial \tau} \left(w(\tau) \left(\frac{c_t}{\lambda_t} \right)_{ref} \frac{k_{ro}}{B_o \mu_o} \frac{\partial p}{\partial \tau} \right) + \frac{\tilde{q}_o}{B_o} \delta(\tau_{wb}) \text{ (Oil)}, \quad (3.6)$$

$$\begin{aligned} \frac{\partial}{\partial t} \left[\phi \left(\frac{S_g}{B_g} + R_s \frac{S_o}{B_o} \right) \right] &= \frac{\phi_{ref}}{w(\tau)} \frac{\partial}{\partial \tau} \left[w(\tau) \left(\frac{c_t}{\lambda_t} \right)_{ref} \left(\frac{k_{rg}}{B_g \mu_g} + R_s \frac{k_{ro}}{B_o \mu_o} \right) \frac{\partial p}{\partial \tau} \right] \\ &+ \left(\frac{\tilde{q}_g}{B_g} + R_s \frac{\tilde{q}_o}{B_o} \right) \delta(\tau_{wb}) \text{ (Gas)}. \end{aligned} \quad (3.7)$$

3.3.2 Simulation Workflow For Multi-well FMM

Previous studies to perform multi-well FMM have an assumption that there is no well interference during the simulation. Therefore, once drainage volume partitions that are associated with each well are determined, we apply the same workflow of FMM-based simulation where a 1-D simulation model is constructed for each well within an individual sub-domain (Figure 3.1). The important step in this workflow is to divide the reservoir into several sub-domains based on the ‘equal- τ ’ interfaces that can approximate no flow boundary between partitions. Huang (2017) also showed that partitions defined by the ‘equal- τ ’ interfaces correspond to the flow partitions obtained from finite difference simulation. This result supports the assumption of no interference between wells during the simulation.

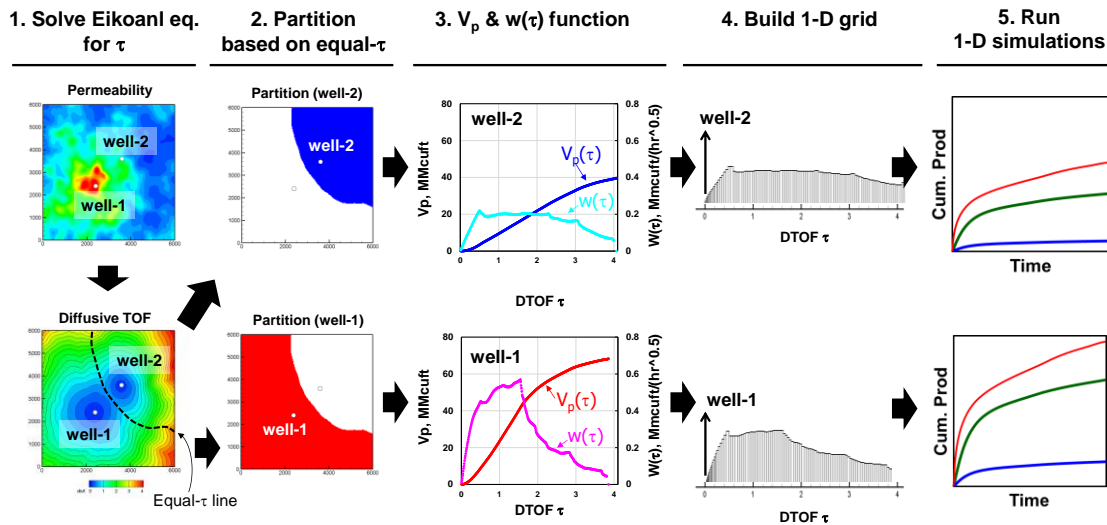


Figure 3.1 Simulation workflow for multi-well FMM using equal- τ interface (Iino, 2018)

However, this assumption is valid only when wells are controlled by the same bottomhole pressure. This is because τ -contours are assumed to be aligned with pressure contours so that equal- τ represents the same pressure. Huang (2017) and Iino (2018) investigated such cases that all wells are controlled by different constant rate and found that drainage volume partitions vary over time, which implies that equal- τ cannot be used to partition the reservoir. Therefore, Iino (2018) proposed a novel approach to account for the communication between partitions with inter-partition transmissibility while each 1-D simulation model is still built based on the partition using equal- τ interfaces (Figure 3.2). This method enables us to have the transmissibility between τ -contours that are contacting each other as a non-neighbor connection (NNC) in the simulation model.

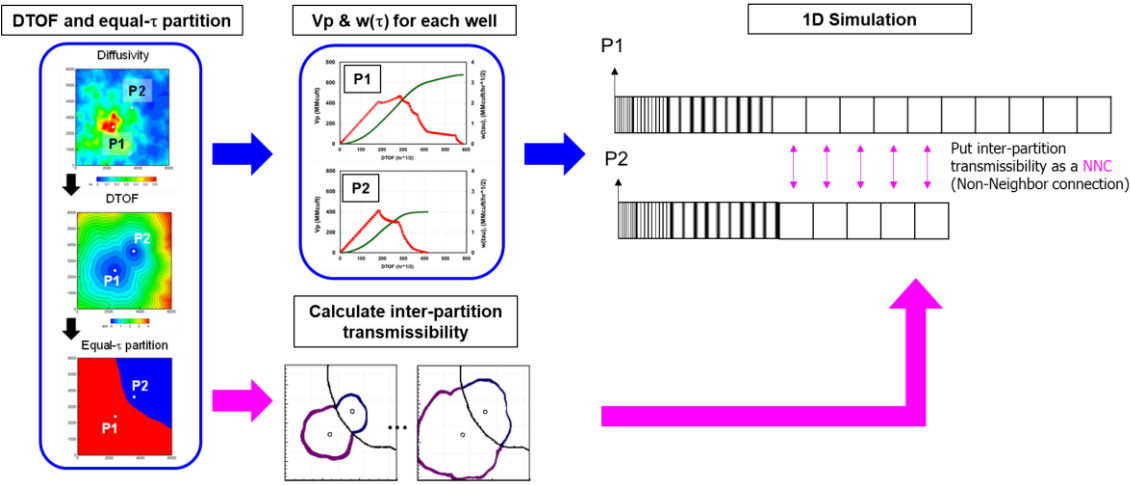


Figure 3.2 Simulation workflow for multi-well FMM using inter-partition transmissibility (Iino, 2018)

3.3.3 Improved Workflow of Inter-partition Transmissibility Calculation

This section describes the improvement on the computation of inter-partition transmissibility. Figure 3.3 shows the previous workflow of the inter-partition transmissibility calculation proposed by Iino (2018). For each pair of partitions, we pick up a τ -contour and calculate the transmissibility between contours using FMM-based pressure calculation. Basically, we run the Fast Marching Method starting from the partition interface, and then the pressure profile will be calculated based on Darcy's law as described in Step-6 in Figure 3.3. Even though this proposed workflow leads to a good agreement with a 3-D Finite Difference simulation, which improves the accuracy of FMM-based simulation, the computational time increases accordingly since we now have additional steps to calculate the inter-partition transmissibility. In addition, the efficiency of FMM-based simulation with the inter-partition transmissibility becomes worse as there are more pairs of partitions to be considered with more wells. This increased portion of computational time mainly is attributed to running the Fast Marching Method one by one for each pair of τ -contours that also requires preparation of the input data for each FMM run. It is not only computationally expensive but also complicated.

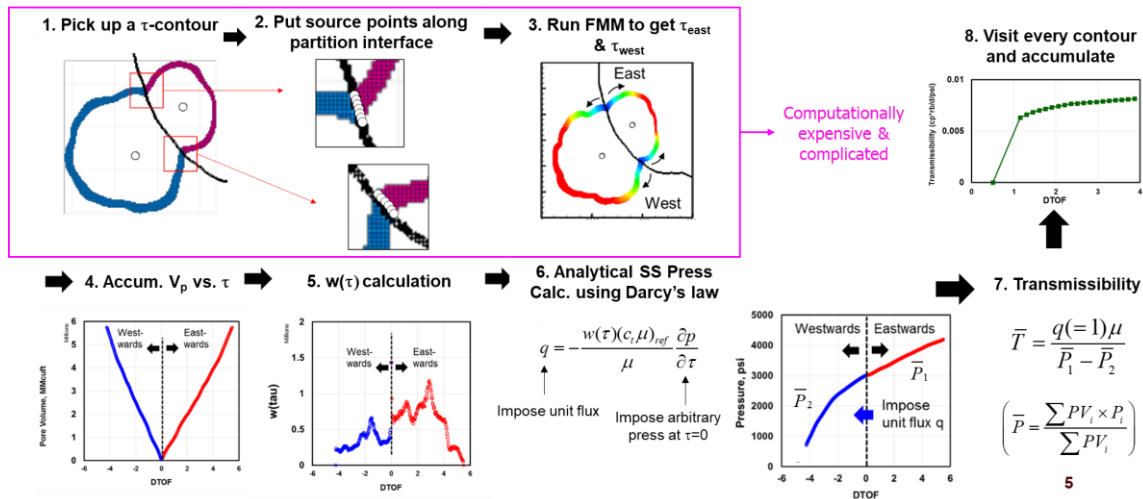


Figure 3.3 Workflow of inter-partition transmissibility calculation (Iino, 2018)

As described before, Step-1 to Step-3 take a significant amount of time during the computation of the inter-partition transmissibility. Therefore, a new method of running FMM for each pair of partitions is proposed in Figure 3.4. After we partition the reservoir based on the DTOF solution from the FMM, source points are placed on the partition interface (Step-1). Next, we start FMM from the partition interface to get the DTOF for each partition (Step-2). Calculation of inter-partition transmissibility starts with the first pair of τ -contours that are contacting each other as shown in Step-3. Figure 3.5 presents the specific workflow from choosing τ -contours to accumulate pore volume in detail. We identify the underlying grid blocks for the τ -contours of interest (Step 3-1). The DTOF solution obtained from Step-2 are then mapped onto the grid blocks (Step 3-2). Next, we compute the pore volume as a function of DTOF for these grid blocks (east and west direction) as shown in Step 3-3. Then, the rest of the workflow is identical as shown in Figure 3.3: we first calculate the $w(\tau)$ function (Step-5). Assuming steady-state conditions

with unit flux across the partition interface, pressure profiles in each side of the partition will be calculated along the DTOF based on Darcy's law (Step-6). The steady-state transmissibilities are computed based on the pore-volume averaged pressures across the partition (Step-7). Next, we select next pair of τ -contours and return to the Step 3-1. The same steps from Step-3 to Step-7 will be repeated for every τ -contour and the inter-partition transmissibility will be accumulated as a function of the DTOF (Step-8).

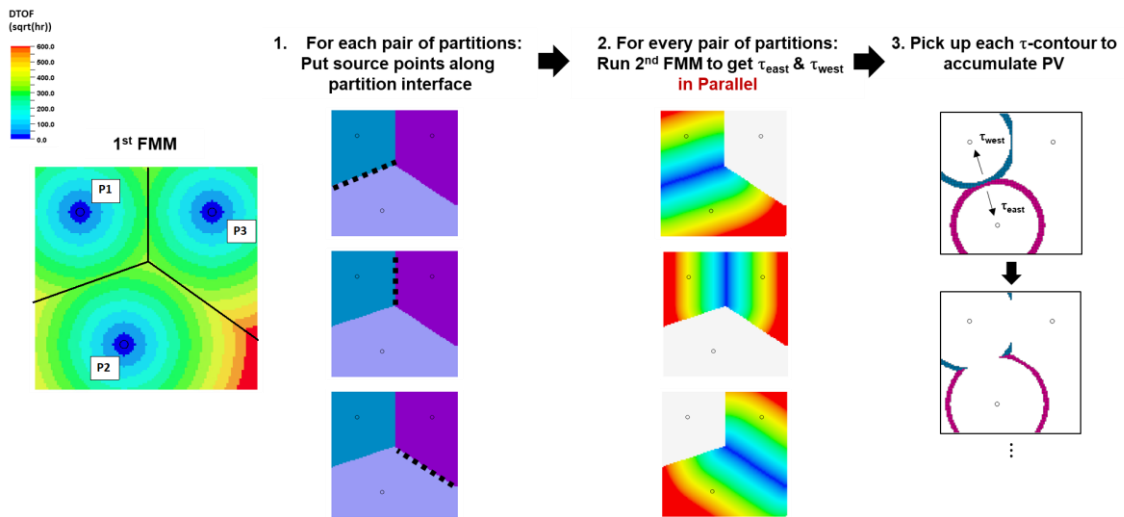


Figure 3.4 New method of performing FMM for each pair of partitions

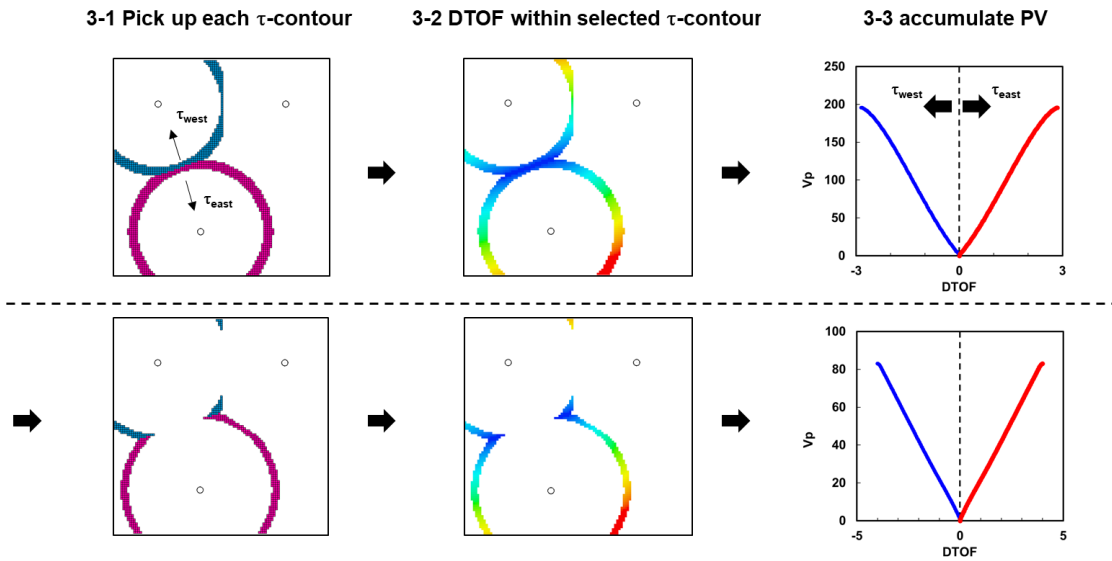


Figure 3.5 Illustration for the accumulation of pore volume within each τ contour sequentially

3.4 Field Application

In this section, we present a field application of multi-well FMM-based simulation using the improved workflow of inter-partition transmissibility. Our objective here is to demonstrate the accuracy and efficiency of the multi-well FMM-based simulation.

3.4.1 Model Setting

The simulation model, which is a single-porosity and 3 phase blackoil system, is provided by an operator. The reservoir domain of 5,280'×5,280'×495' was gridded into cells of 264×1267×46 (15,386,448). Tartan grid is used in x and y direction where there is refined grids around wells and hydraulic fractures. Each well has a planar type of hydraulic fractures where there are 35 stages with four clusters per stage. High permeability (120 md) is assigned to the grid blocks of hydraulic fractures, leading to a

fracture conductivity of 120 md-ft. In addition, Stimulated Reservoir Volume (SRV) regions are defined near wells (Figure 3.6) and hydraulic fractures with higher permeability compared to matrix in the reservoir. Figure 3.7 shows some of reservoir properties, such as permeability and porosity. Permeability is in micro-darcy scale, representing the tight formation. This reservoir has seven horizontal wells that are drilled into two zones defined in the model as shown in Figure 3.8.

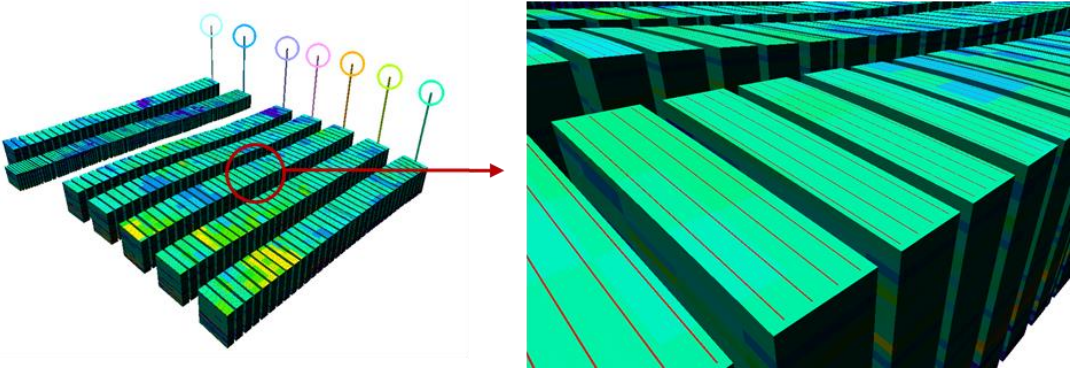


Figure 3.6 Hydraulic fracture and SRV region in the field application case

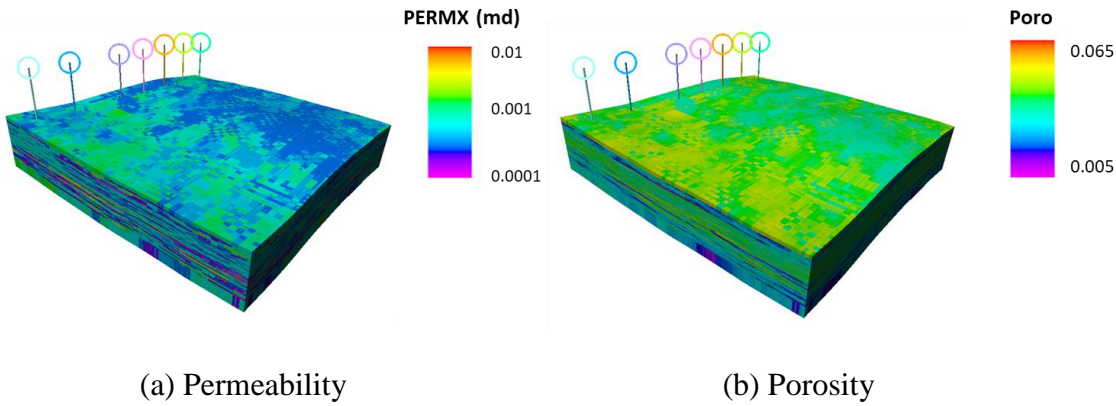


Figure 3.7 Reservoir properties for field case: (a) permeability and (b) porosity

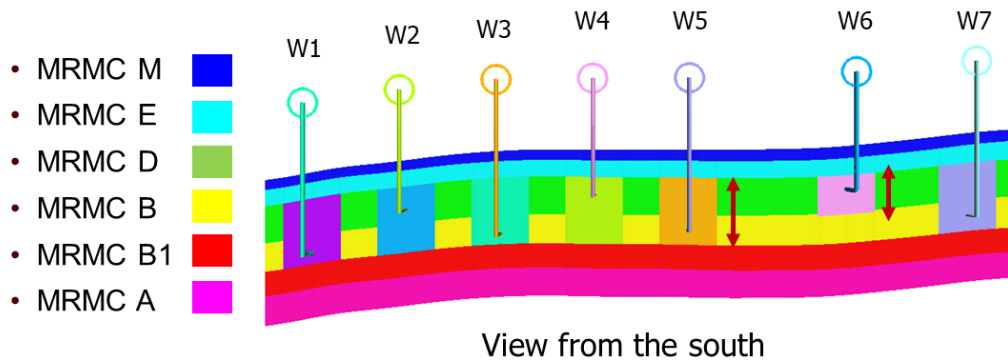
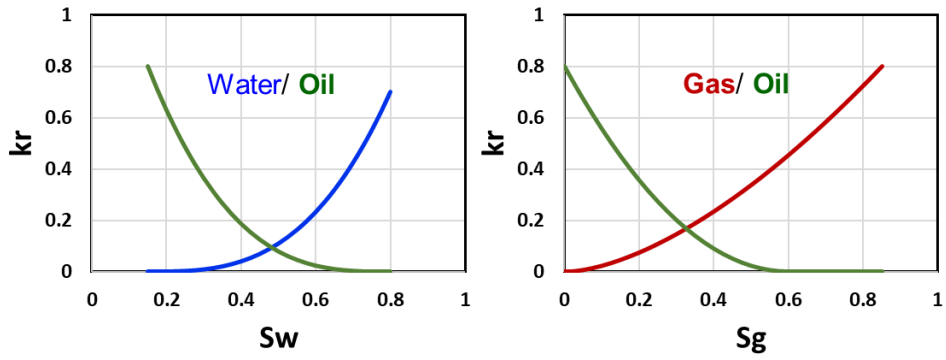


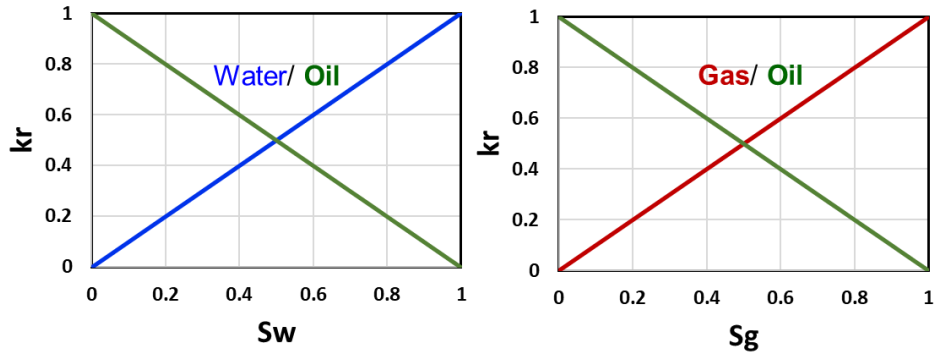
Figure 3.8 Location of wells and defined zones in the simulation model

3.4.2 Fluid and Rock Properties

In this application, three-phase relative permeability curves are used for matrix/SRV and hydraulic fractures respectively as shown in Figure 3.9. In particular, a linear relationship between saturation and relative permeability is used for the hydraulic fracture region due to the high conductivity. This is because capillary pressure is negligible (due to high permeability), which indicates low interfacial tension resulting in straight line in the relative permeability curves. In addition, the reduction in permeability and pore volume with respect to pressure depletion is considered by using compaction table (Figure 3.10). Similar to the relative permeability, two different rock compaction curves are assigned to Matrix/SRV and hydraulic fracture regions respectively.



(a) Matrix and SRV region relative permeability



(b) Hydraulic fracture relative permeability

Figure 3.9 Relative permeability for a field case

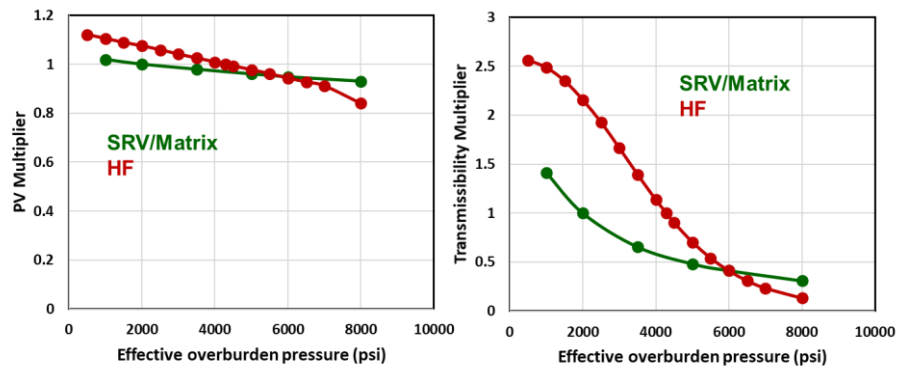


Figure 3.10 Rock compaction curves for a field case

3.4.3 Reservoir Partitioning

We first run the Fast Marching Method for the entire reservoir and determine the equal- τ interfaces to divide the reservoir into independent sub-domains associated with each well (Figure 3.11). Based on the partitions, 1-D simulation models for individual well can be created by considering pore volume in each partition. Afterwards, the inter-partition transmissibility is calculated as discussed in Section 3.3.3 to account for the communication between partitions.

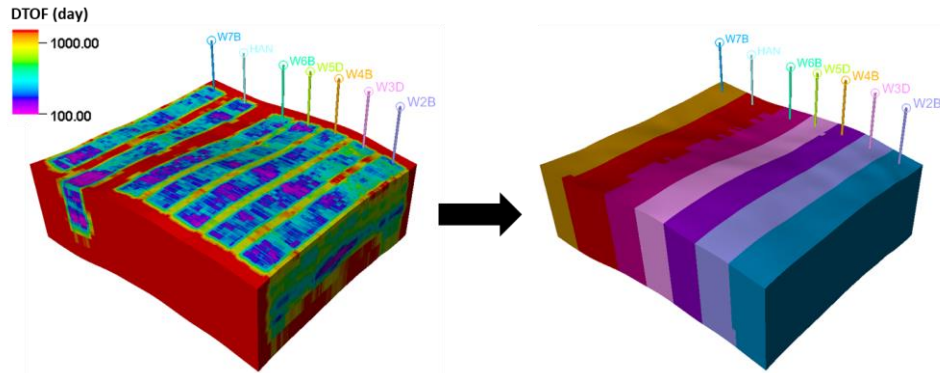


Figure 3.11 Partitioning the reservoir using equal- τ interface: Diffusive time of flight (left) and determined partitions (right)

3.4.4 Comparison of Simulation Results

We perform the multi-well FMM-based 1-D simulation using the improved calculation of the inter-partition transmissibility, which is compared with results from a 3-D Finite Difference simulation to demonstrate the accuracy and feasibility of the FMM-based simulation. We first simulated production period for 300 days, where wells are controlled by gas rate until 150 days and later they are constrained by BHP for the rest of 150 days. Figure 3.12 and Figure 3.13 show simulation responses of selected wells (Well

#1 and Well #4), such as oil production rate, water cut, gas-oil ratio and bottomhole pressure. In general, they show a good agreement with each other, except for the water cut. The mismatch in water production can result from the effect of gravity because the pressure is no longer aligned with DTOF contours in the planar type of hydraulic fractures where high permeability is assigned as illustrated in Figure 3.14. In addition, the FMM-based simulation transforms a 3-D reservoir model into an equivalent 1-D model, and consequently the effect of gravity cannot be evaluated properly. Therefore, Onishi (2019) suggested the new approach to deal with the gravity in hydraulic fractures while the rest of reservoirs are converted into the corresponding 1-D grid blocks.

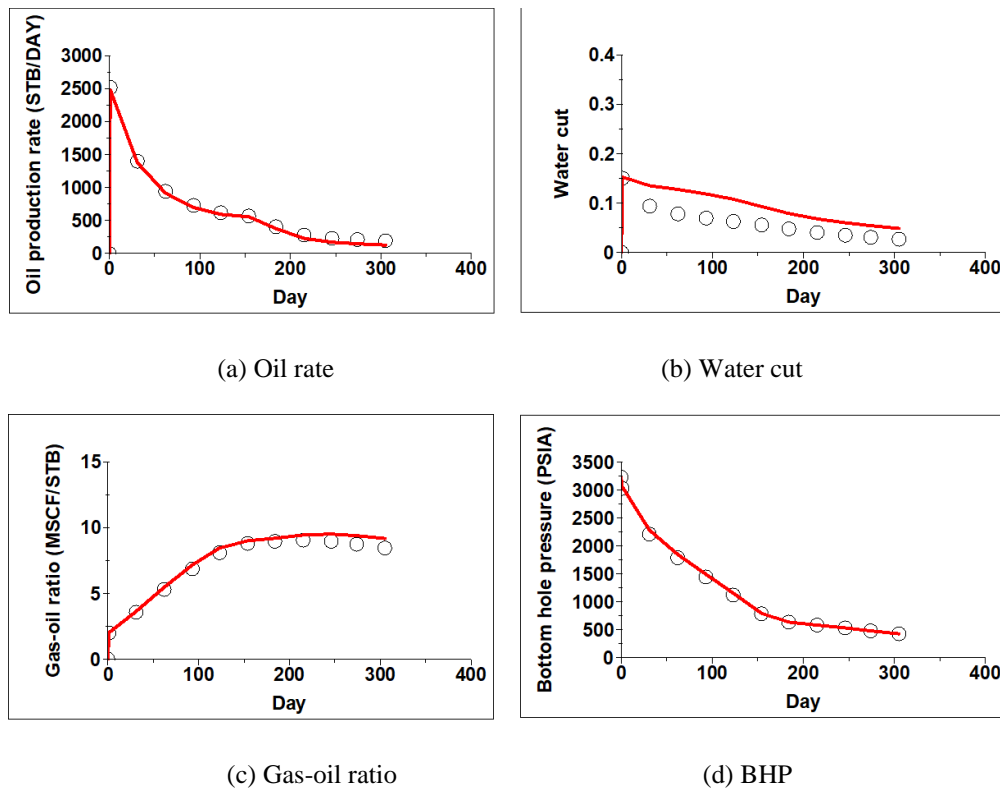


Figure 3.12 Comparison of simulation results for Well #1 (Symbol: FD simulation and line: FMM)

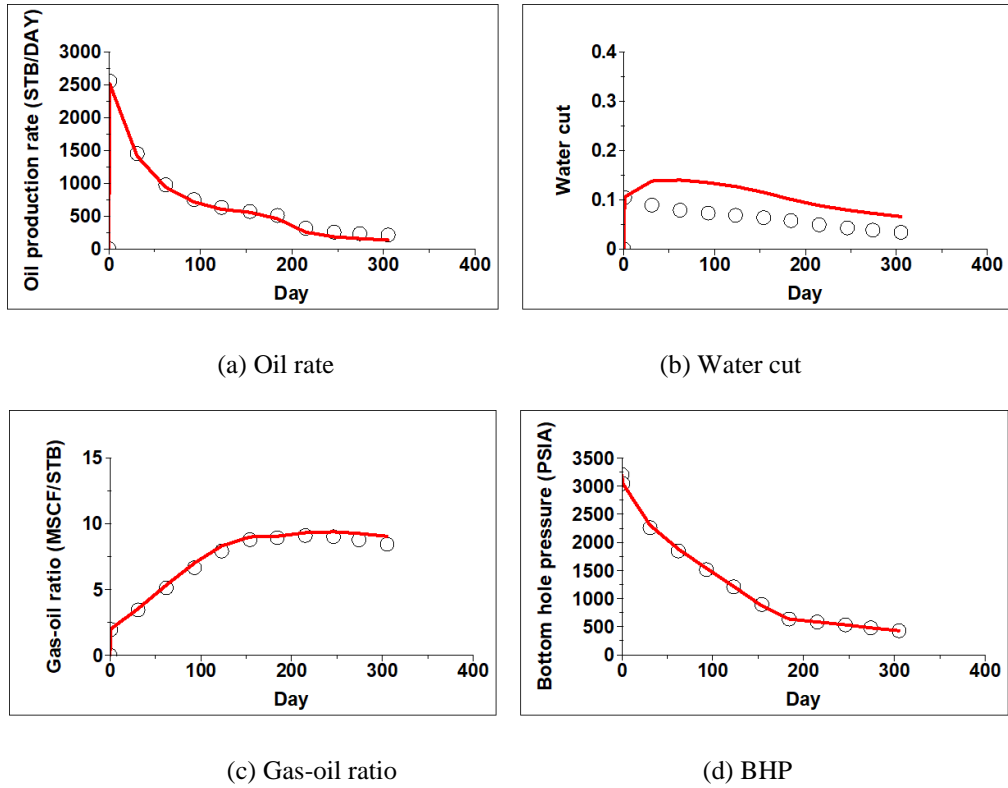


Figure 3.13 Comparison of simulation results for Well #4 (Symbol: FD simulation and line: FMM)

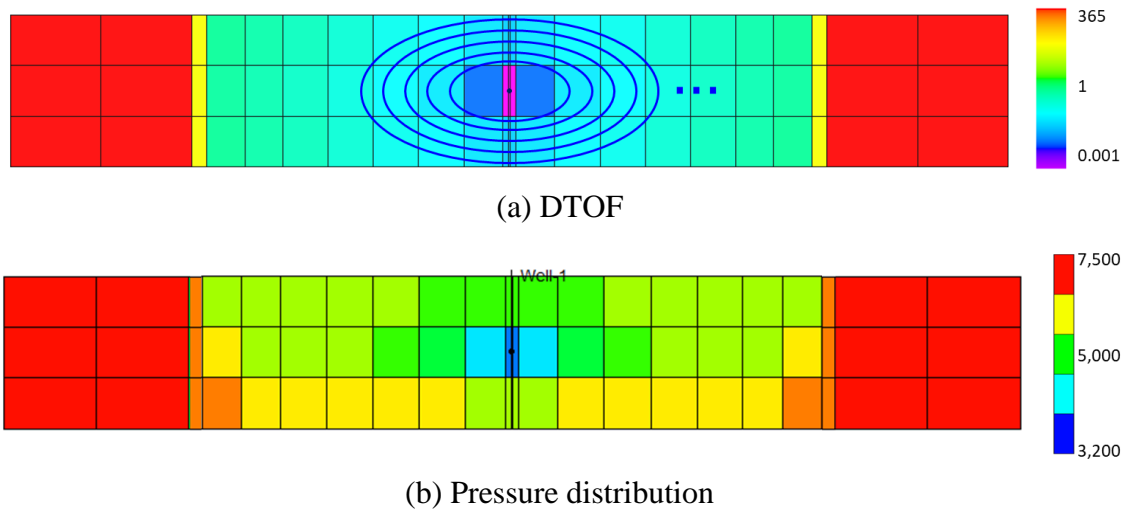


Figure 3.14 Diffusive time of flight in the hydraulic fracture plane (top) and pressure distribution after 1 year in the original 3-D model (bottom)

3.4.5 Comparison of CPU Time

The computational efficiency of the multi-well FMM-based simulation using the improved inter-partition transmissibility calculation (FMM_New) is compared with the FMM with the previous workflow (FMM_Old) as well as a Finite Difference simulation (Figure 3.15). Overall, both FMM-based simulations are able to achieve faster computation compared to a Finite Difference simulation (FDsim) even though the FDsim used four cores in parallel. Therefore, it is expected to be significantly efficient if the FMM-based simulations are used in either history matching or optimization workflow. It is also noted that the FMM_New performs better in terms of CPU time than the FMM_Old due to the optimized workflow when we compute the inter-partition transmissibility. As shown in Figure 3.16, running the FMM once for each pair of partitions provides significant computational efficiency, instead of dealing with each τ -contour respectively.

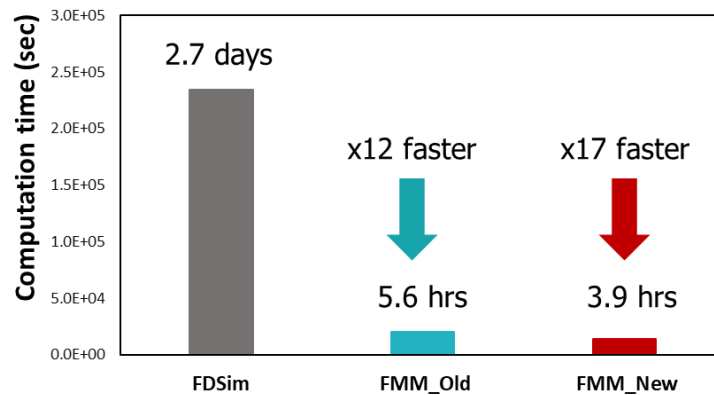


Figure 3.15 CPU time comparison for a field case

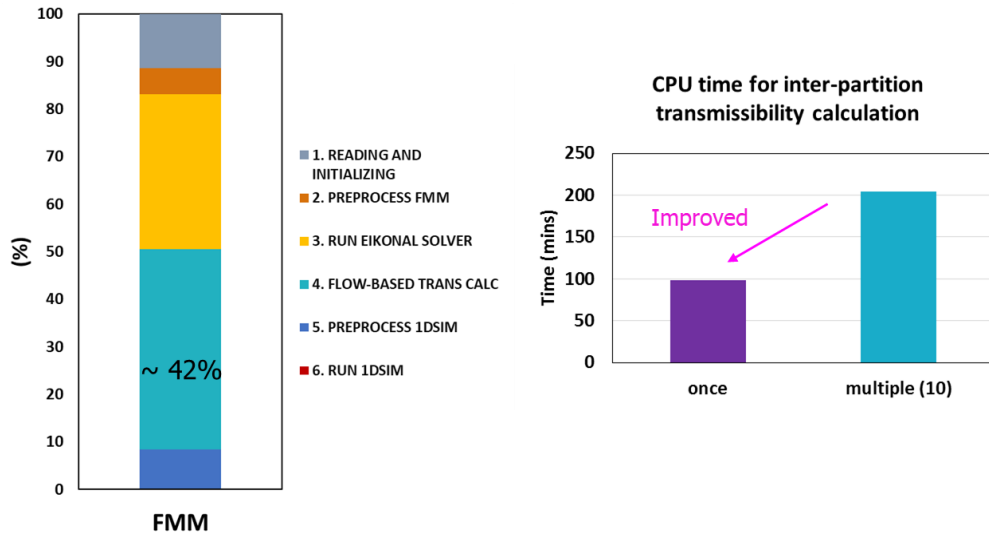


Figure 3.16 CPU time breakdown for FMM (left) and comparison of CPU time for inter-partition transmissibility calculation only (right)

3.5 Conclusions

The extension of the Fast Marching Method (FMM) based flow simulation to multi-wells has shown significant effects in modeling and performance assessment of unconventional reservoirs (Huang 2017, Iino 2018). It has provided viable solutions for efficient modeling and simulation of unconventional reservoirs while tackling a computational limitation of simulation models with multi-million cells. However, most of previous efforts were limited to synthetic cases especially for multi-well applications. Therefore, in this chapter, we concentrated on the power and utility of a novel approach using inter-partition transmissibility on the actual field application. Major conclusions in this chapter are summarized below.

- For the field application presented in this chapter, we demonstrated the feasibility of the FMM-based approach in terms of not only the accuracy but also efficiency.

The comparison of simulated responses with the ones from a Finite Difference simulation has shown a good agreement. In addition, depending on the production schedule, the slow convergence in a conventional 3-D Finite Difference simulation can hinder successful development of unconventional field in a practical timeframe. However, a novel approach using the FMM-based simulation enables us to evaluate the well performance in a more robust way by eliminating stability issues that are involved with 3-D simulation models, resulting in a faster computational time. Consequently, more savings in time can be expected when it is applied to either the history matching workflow or the optimization process, which requires a large number of simulations.

- The revised procedure for the computation of the inter-partition transmissibility has enhanced the efficiency of the FMM-based simulation. In the previous workflow, the communication between partitions is based upon the interaction between τ grids that are associated with each other. As a result, the inter-partition transmissibility is calculated for every pair of τ grids in sequence, leading to a lot of FMM runs respectively. Instead, the current workflow performs the FMM once per each pair of partitions, which simplifies steps engaged in the calculation of the inter-partition transmissibility as well as reduces overall computation time. The field example in this chapter indicated that there is the improvement in CPU time in conjunction with the new workflow. Also, it can be expected to be more substantial with a greater number of wells/partitions.

CHAPTER IV

UNDERSTANDING RESERVOIR MECHANISM USING HISTORY MATCHING:

DOVER 33 FIELD CARBON DIOXIDE EOR

4.1 Chapter Summary

CO₂ injection in hydrocarbon reservoirs contributes to not only improvement in oil recovery but also climate changes by reducing the amount of CO₂ in the atmosphere. Even though CO₂ injection has been considered as one of the most effective EOR methods in the conventional reservoir, applying it to unconventional resources still remains uncertain in various aspects. In addition, subsurface systems can be understood by learning from the reservoir response through a history matching process, which involves the integration of observed data into a prior geologic model.

In the development of Dover 33 field, which is located in the Northern Michigan, there have been mainly three production periods: primary depletion, CO₂ EOR and CO₂ injection only period for storage purposes. Previous efforts of manual history matching process achieved a reasonable match quality until a certain point of the CO₂ injection period. However, a steeper pressure buildup near the end of CO₂ injection period is not being captured successfully. The major issue in the CO₂ injection only period is that a sharp increasing trend of bottomhole pressure takes place even with the reduced injection rate. This indicates that changing reservoir properties and adjusting relative permeability curves in the previous production periods were not sufficient to identify the reservoir mechanism that is involved in the pressure rise during the CO₂ only injection period.

In this chapter, we develop the workflow of a multi-stage model calibration by incorporating fluid model adjustment as well as reservoir model calibration using Genetic Algorithm. First, parameters of the Equations of State (EOS) will be calibrated with available experimental data. Then, several sets of EOS models will be carried over to the history matching process for primary depletion where reservoir properties including permeability multiplier, pore volume multiplier and relative permeability will be changed to match the observed data such as oil and gas production, and bottomhole pressure. Once the process of history matching is successfully finished for primary depletion, further adjustment will continue for CO₂ EOR period and CO₂ injection only period with the reduced ranges from the primary depletion period.

4.2 Background

Dover 33 field is one of the oil-bearing pinnacle reefs in Northern Michigan. It is a small reservoir with approximately 3 MM STB original oil in place. It has been developed since 1975 starting from primary depletion followed by an enhanced oil recovery (EOR) using carbon dioxide. After the EOR, there is a CO₂ injection only period without producers for storage purposes. Previous studies focused on the investigation of CO₂ EOR and associated storage issues by updating a reservoir model manually to match the history data for primary depletion and CO₂ EOR period respectively. They also have used different geologic conceptual model realizations from homogeneous to heterogeneous models. Various realizations were able to achieve reasonable match during primary depletion and CO₂ EOR period but not during CO₂ injection only period where

the pressure build up is steeper even with a decreasing injection rate. In addition, the way of adjusting parameters during manual history matching is more or less local where box-type areas are specified, especially near the wells.

Therefore, the objective of this project is to perform an assisted history matching for primary depletion as well as CO₂ EOR, rather than a manual history matching. Once acceptable history matched models are obtained, they are used to predict the behavior of pressure response during CO₂ injection only period. In case that prediction of bottomhole pressure of an injector does not follow the observed data, an additional history matching incorporating CO₂ injection only period will be performed to investigate and understand the behavior of pressure response.

In this chapter, we present a hierarchical workflow of the model calibration to understand the reservoir mechanism of the Dover 33 field. Prior to a reservoir model calibration, the EOS model is calibrated using a population-based approach to obtain several sets of updated EOS models, which lead to improved fluid characterization and reduces uncertainty in various phases of productions. Then, a hierarchical history matching using Genetic Algorithm is conducted including three stages of model calibrations in sequence (1st stage history matching for primary depletion period, 2nd stage history matching for CO₂ EOR period and 3rd stage history matching for CO₂ injection only period).

4.3 Methodology

This section describes the simulation methodology for the hierarchical model calibration using a population-based approach, which includes a fluid model calibration as well as a reservoir model calibration as shown in Figure 4.1.

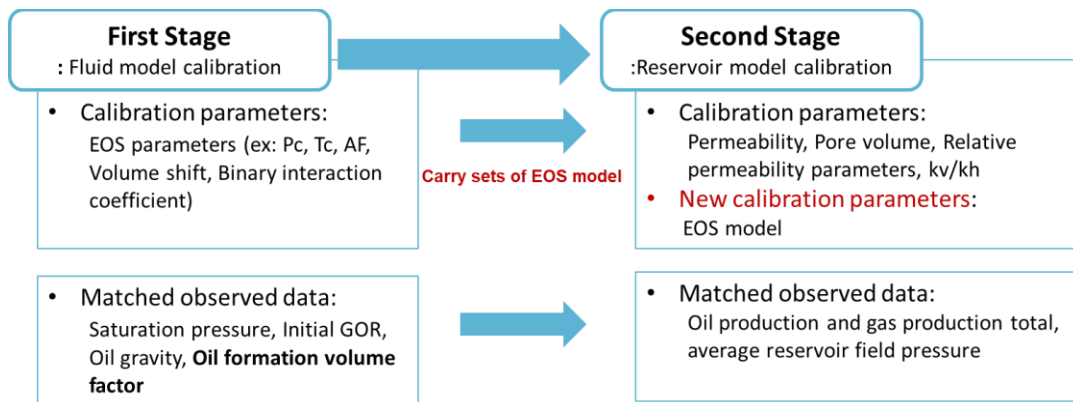


Figure 4.1 Flowchart of hierarchical model calibration

4.3.1 EOS Model Calibration Using Genetic Algorithm

In this chapter, Equations of State (EOS), which predicts multi-phase behavior of fluids and volumetric properties, is considered as one of the calibration parameters during the history matching process because current fluid model has some level of uncertainty. This is because reservoir fluid samples are not collected at the beginning of primary production. Then, the composition of reservoir fluids is characterized based on the fluid samples from the end of primary depletion by adding the lighter components to match the available experimental data, which are bubble point pressure, initial oil gravity and initial GOR. However, there are several limitations to directly change parameters of an EOS model during the reservoir model calibration. First, the number of parameters in EOS

model is considerable since each component in a fluid model has several associated parameters, such as critical properties (critical pressure and critical temperature), binary interaction coefficient, volume shift and acentric factor. If those parameters are incorporated in the history matching process using Genetic Algorithm, the population for each generation is required to increase proportionally to explore the parameter space, which might cause severe computational inefficiency. Second, a set of parameters are randomly selected for each model during the Genetic Algorithm, which is typically not an issue for most of parameters. However, arbitrarily selected parameters in an EOS model are able to generate non-monotonicity, especially for critical pressure/temperature and acentric factor, which leads to unphysical phase behavior as shown in Figure 4.2. Therefore, in order to avoid the complexity involved in EOS parameters, the fluid model calibration is performed separately prior to the reservoir model calibration to obtain several sets of EOS models. Then, we take those EOS models as one of the tuning parameters in primary depletion history matching.

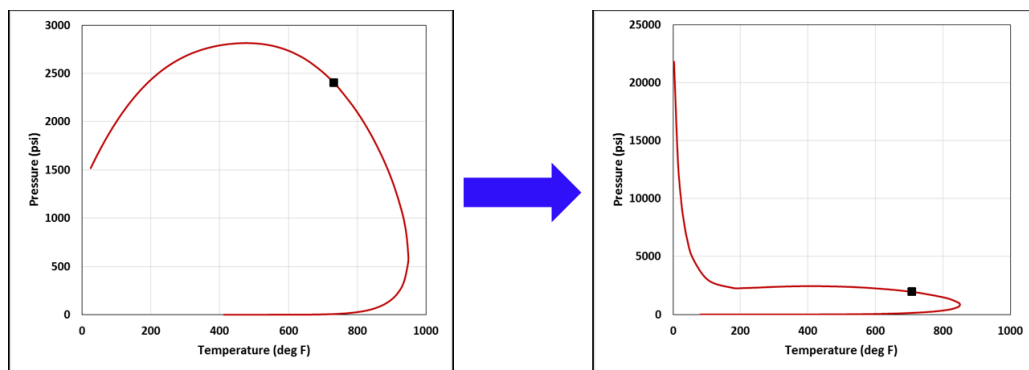


Figure 4.2 Examples of phase behavior: Physically correct (left) and physically incorrect (right)

Furthermore, in order to achieve several fluid models efficiently, a population-based approach is used for the EOS model calibration. It is common to apply the regression method for most of fluid model calibration because this gradient-based approach shows faster convergence than stochastic methods. Even though it is computationally expensive to employ Genetic Algorithm, it is useful to search for several optimal solutions. Figure 4.3 represents the workflow of the fluid model calibrations in detail. The Objective function during Genetic Algorithm is to minimize the misfit of experimental data and simulated responses, which is calculated as shown in Eqs. (4.1) and Eqs. (4.2).

$$f(x) = \sum_{i=1}^n r_i(x)^2. \quad (4.1)$$

$$r_i = \frac{e_i(x) - y_i}{y_i} \quad \& \quad x = [x_1, x_2, \dots, x_m] \quad (4.2)$$

Where $e_i(x)$ represents Equations of state results, y_i is experimental data points and x is regression parameters.

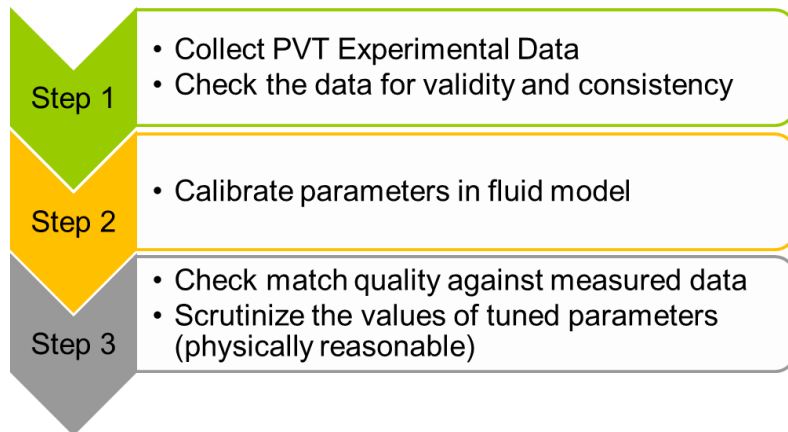


Figure 4.3 Workflow of fluid model calibration

4.3.2 Hierarchical History Matching Using Genetic Algorithm

Assisted history matching using multi-objective Genetic Algorithm has been performed for the Dover 33 field. As compared to a manual history matching process where parameters are selected by human subject each time and the quality of match is evaluated qualitatively by visualizing simulation responses, the GA-based automatic history matching provides a systematic and efficient way to evaluate possible sets of parameters. In addition, instead of using single-objective GA, which aggregates all objective functions into one scalar value, multi-objective GA is well suited to simultaneously consider multiple objective functions allowing for trade-off between them (Park et al (2015)). The methodology of the history matching is summarized in Table 4.1.

Table 4.1 Summary of hierarchical history matching

Method	Multi-objective Genetic Algorithm
Forward Simulation	Eclipse (e300: compositional simulator)
Simulation Constraint	Reservoir fluid volume production rate
Objective Function	Misfit of Well cumulative oil production, Well cumulative gas production and Average field pressure
History Matching Period	Hierarchical history matching 1 st stage HM: Primary depletion 2 nd stage HM: CO ₂ EOR period 3 rd stage HM: CO ₂ injection only period

In this Dover 33 field, there are three different field development plans, which consist of primary depletion, CO₂ enhanced oil recovery and CO₂ injection only period (Figure 4.4). Therefore, the history matching process includes these three phases in a hierarchical manner. In other words, all the initial parameters are varied to obtain the

desired match during the primary depletion. Subsequently, a further tuning with reduced ranges from the previous history match will be conducted by incorporating the following production period and additional parameters added, if needed. Then, if updated models with the calibrated parameters from the first two stages of the history matching are not able to predict the behavior of pressure responses during the CO₂ injection only period (Figure 4.5), which demonstrate a sharp increasing trend, an additional history match will be required.

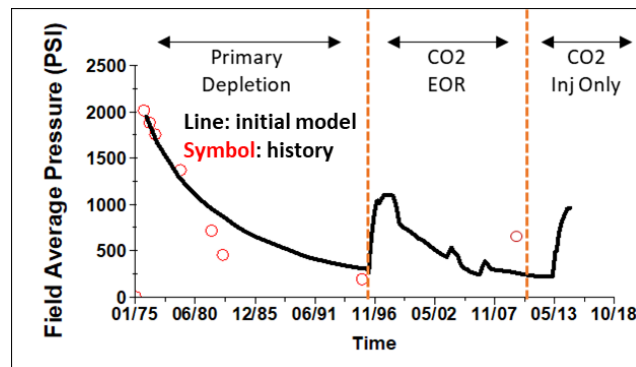


Figure 4.4 Three production periods in the Dover 33 field

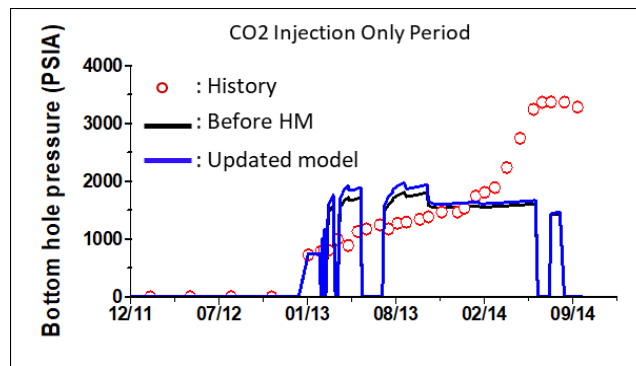


Figure 4.5 Comparison of the bottomhole pressure of the injector during CO₂ injection only period

As for the adjustment of reservoir permeability during the GA, the parameterization using the Grid Connectivity-based Transform (GCT) has been performed instead of using a uniform multiplier that is applied to artificially cropped regions. A variety of parameterization methods has been widely used in the petroleum engineering where parameters are represented as a linear combination of basis functions. The GCT has been developed by only accounting for grid connectivity information which is independent of grid properties (Bhark et al. 2011). For the Dover 33 field, 10 basis functions have been generated (Figure 4.6), which results in smooth changes in permeability field with a geological continuity using a small number of parameters.

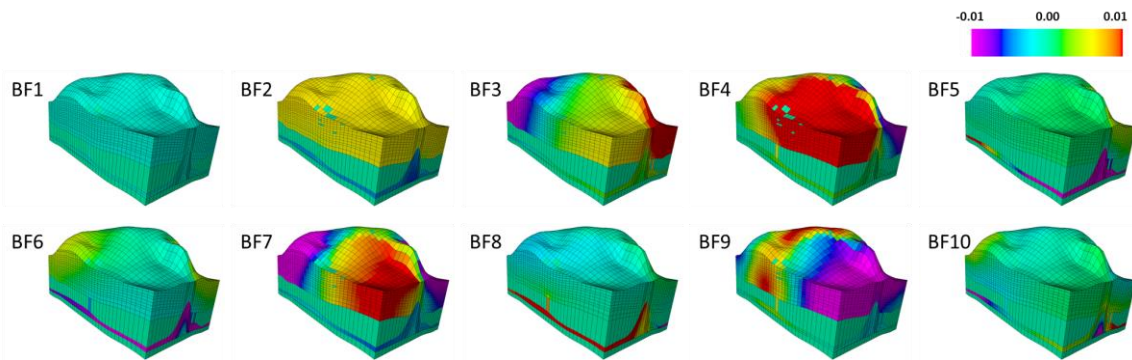


Figure 4.6 Basis functions using Grid Connectivity-based Transform (GCT)

4.4 EOS Model Calibration

In this section, we demonstrate the workflow of the fluid model calibration utilizing a population-based approach. Based on the oil formation volume factor and the initial gas-oil ratio, three different GA runs are evaluated in order to tune parameters in the EOS model.

4.4.1 Initial EOS model

For an initial case, reservoir fluids are characterized through the Equations of State model. Although original fluid samples were not taken in this field when primary depletion begins, analysis of the produced gas from the field has been obtained and performed periodically. Later, the first fluid sample was collected in order to prepare the enhanced oil recovery project. Based upon the fluid sample at the end of primary production and analyses of the produced gas, composition of the original fluids (Table 4.2) are predicted to match some of fluid properties that will be described in the following section 4.4.2. In the Table 4.2, components are listed as pseudo components which have been lumped from the original fluid components to prevent expensive computations that can be caused by detailed fluid description and the lumping has been performed by the field operator. The phase behavior of initial reservoir fluids is shown in Figure 4.7 and associated volumetric properties for oil and gas phases are presented in Figure 4.8. Since this fluid characterization was conducted with the limited data without the original fluid sample, there are still uncertainties inherent in an initial fluid characterization, which will be discussed in the following sections from 4.4.3 to 4.4.4.

Table 4.2 Composition of the original fluid

Component	ZI (%)
F1	40.912
F2	0.1019
F3	20.235
F4	17.389
F5	14.725
F6	2.7514
F7	3.8855

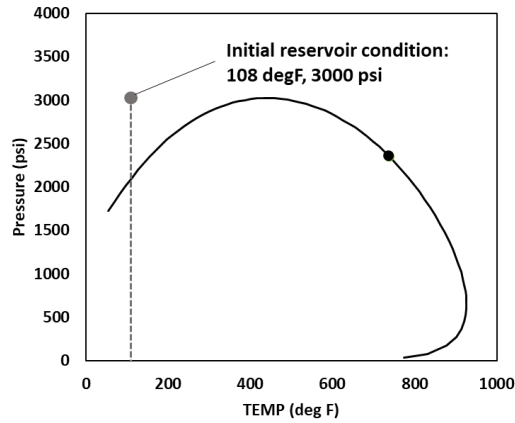


Figure 4.7 Phase behavior of the original fluid

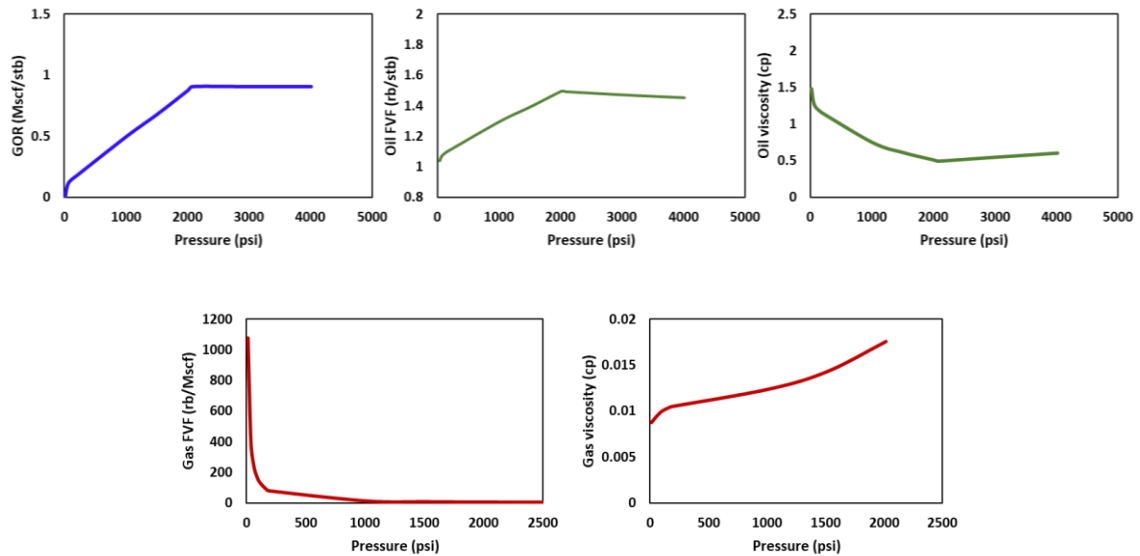


Figure 4.8 Volumetric properties of the original fluids

4.4.2 Experimental Data to be Matched

As explained before, there were limited experimental data for fluid properties due to the lack of original fluid samples. According to the operator, three properties are available in this study: initial oil gravity (43.6 API), initial producing gas-oil ratio (600-800 scf/stb) and approximated bubble point pressure (2017 psi) from the material balance

calculation. Since the reservoir was indicated to be under-saturated, the initial producing gas-oil ratio should approximate the original solution gas-oil ratio. In addition to the available data for the fluid model calibration, the oil formation volume factor from the initial fluid model has been adjusted to represent different behaviors of oil with respect to pressure changes (Figure 4.9). Typically, when checking and correcting fluid data, bubble point properties can be altered while the trend of properties can be preserved. Therefore, oil formation volume factor at the bubble point pressure has been changed with the same oil compressibility above the bubble point pressure. On the other hand, the gradient below the bubble point pressure is different to see the effect of change of oil volume in the reservoir. In the following sections, all three data including the initial oil gravity, a producing gas-oil ratio and bubble point pressure are used with the different oil formation volume factor to perform the fluid model calibration respectively. As a result, multiple updated fluid models are obtained from each model calibration, which will be one of parameters for history matching during primary depletion.

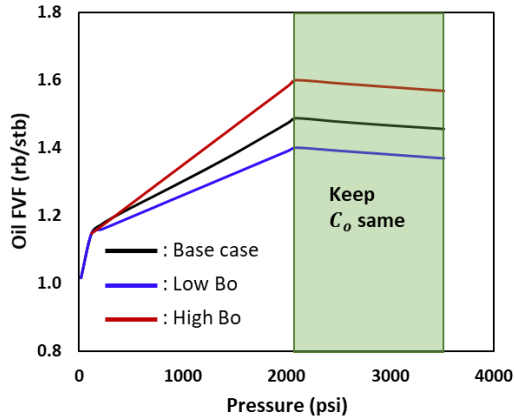


Figure 4.9 Three different oil formation volume factor cases

4.4.3 Case 1: Low Oil Formation Volume Factor

We first performed Genetic Algorithm for the low oil formation volume factor case in this section. Parameters of Equations of State are adjusted including critical properties, binary interaction coefficients, volume shift and acentric factor. As shown in Figure 4.10, misfit between experimental data and simulated responses is reduced over the generation. After finishing the model calibration using Genetic Algorithm, four fluid models are selected as an input for reservoir model calibration in the next step. Figure 4.11 and Table 4.3 show the match quality for one of the selected models.

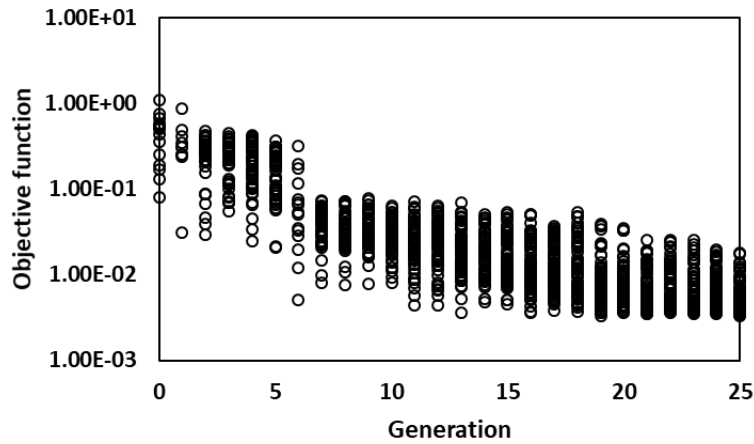


Figure 4.10 Results of Genetic Algorithm for Case 1

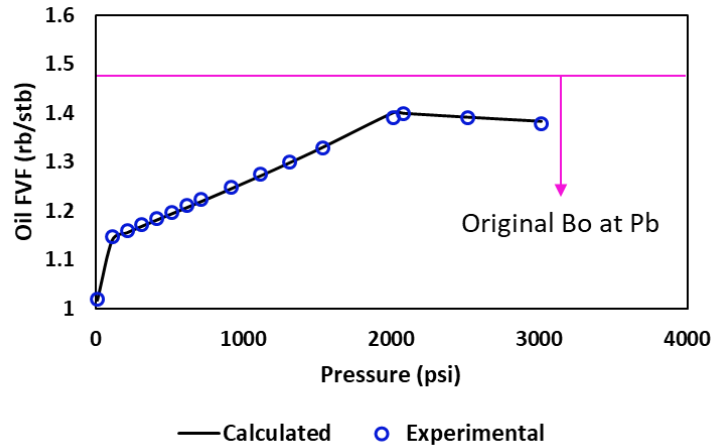


Figure 4.11 Oil formation volume factor of the history matched model for Case 1

Table 4.3 Comparison of experimental data with the calculated values from the history matched model for Case 1

	Experimental	Calculated
Bubble point pressure (psi)	2017	2015
Initial oil gravity (API)	43.6	43.998
Initial GOR (scf/stb)	700	698.46

4.4.4 Case 2: High Oil Formation Volume Factor

In this section, we have used high oil formation volume factor as depicted in the section 4.4.2. Similarly, the model calibration is performed by changing the parameters of the EOS model. As demonstrated in Figure 4.12, objective function has been reduced as the generation goes. We also choose four updated models from this fluid model calibration and properties of one of chosen models are presented in Figure 4.13 and Table 4.4. It has been noticed that the reasonable match quality of the high oil formation volume factor is

achieved even though it is not excellent as we have seen in the case of the low oil formation volume factor.

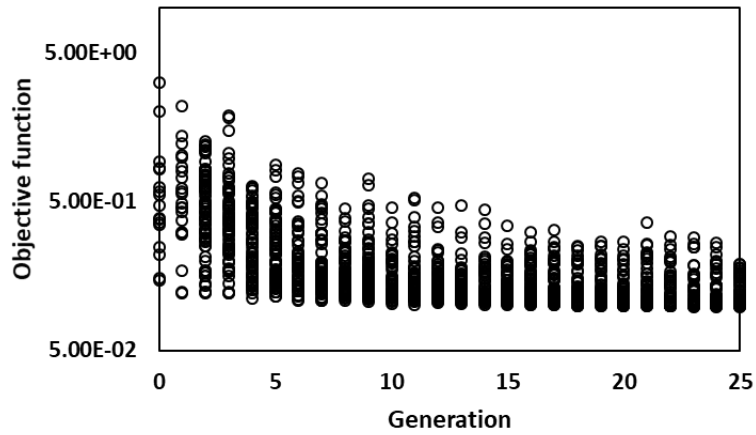


Figure 4.12 Results of Genetic Algorithm for Case 2

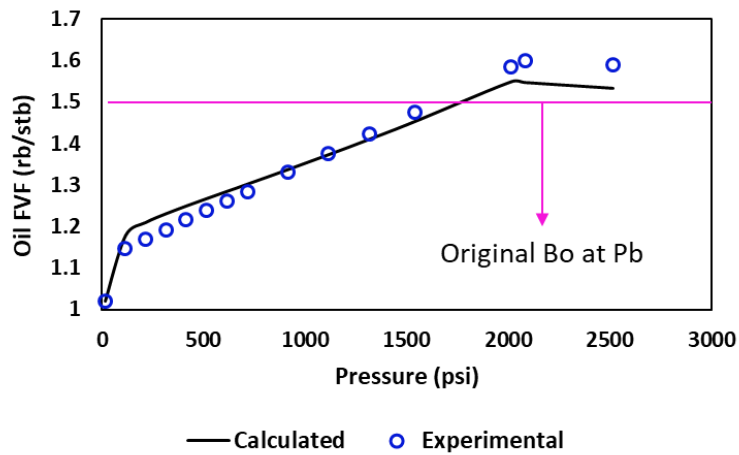


Figure 4.13 Oil formation volume factor of the history matched model for Case 2

Table 4.4 Comparison of experimental data with the calculated values from the history matched model for Case 2

	Experimental	Calculated
Bubble point pressure (psi)	2017	2015
Initial oil gravity (API)	43.6	46.037
Initial GOR (scf/stb)	700	865.73

4.4.5 Case 3: Low Oil Formation Volume Factor with Low Gas-Oil Ratio

In addition to the first case where the fluid model calibration has been performed with the low oil formation volume factor, one more case has been studied with low gas-oil ratio. In the report provided by an operator, the initial gas-oil ratio has been observed between 600-800 scf/stb so that initial GOR has been setup as 700 scf/stb for the first two fluid model calibrations. However, in the observed data, the initial GOR that is available for the well during primary production is between 628 and 667 scf/stb which seems slightly lower than what we used. Therefore, another model calibration with the low oil formation volume factor as well as the low gas-oil ratio (600 scf/stb) has been conducted to obtain several updated fluid models. The progress of objective functions and comparison of fluid properties for the selected model are presented in Figure 4.14, Figure 4.15 and Table 4.5. As you can see, the obtained initial GOR from this GA runs is lower than the one from the Case 1 while achieving reasonable match quality for the other properties.

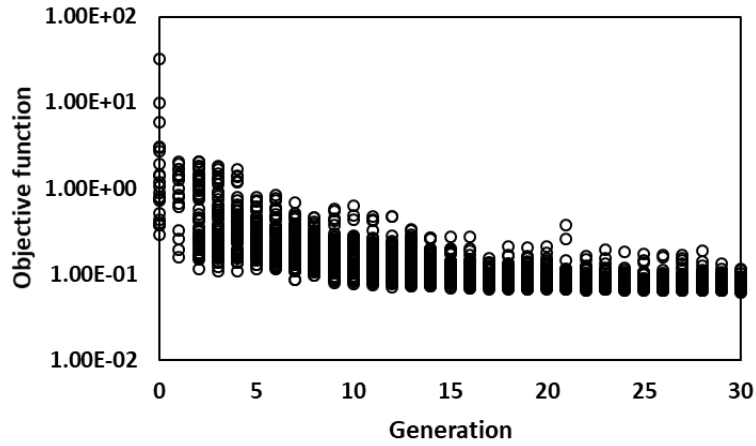


Figure 4.14 Results of Genetic Algorithm for Case 3

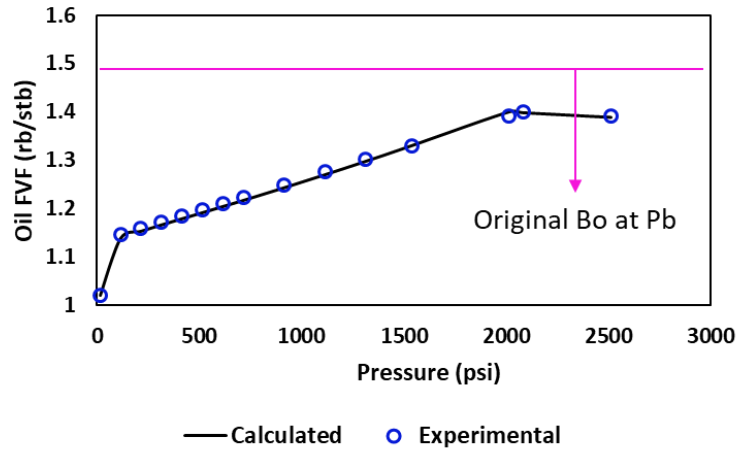


Figure 4.15 Oil formation volume factor of the history matched model for Case 3

Table 4.5 Comparison of experimental data with the calculated values from the history matched model for Case 3

	Experimental	Calculated
Bubble point pressure (psi)	2017	1999
Initial oil gravity (API)	43.6	46.2
Initial GOR (scf/stb)	600	663

4.5 Reservoir Model Calibration

In this section, we present a hierarchical history matching that has been done in several stages that are associated with different production periods. Our focus is to show the applicability of multi-stages of history matching, narrowing down uncertainties of reservoir properties.

4.5.1 Initial Model Setting

We first present an initial model that is provided by the operator. The reservoir model is modeled using about 68,000 grid blocks and each grid cell is about 80 ft in x and y direction. The simulation model is a heterogeneous reservoir as shown in porosity and permeability distribution (Figure 4.16) with an approximate dome shape. There is one vertical well in the center of the reservoir, which is an originally producer and will be converted to an injector during the enhanced oil recovery process. Figure 4.17 also shows initial saturation and initial pressure distribution of the field. Due to the lack of information, water saturation below subsea level is set to one whereas the other area has water saturation of between 0.2 and 0.3, which is close to the critical water saturation. In addition, water saturation will not be included during the history matching process since the water production data is not reliable according to an operator. In this field case, three phase relative permeability curves are used as presented in Figure 4.18. Although it is provided by the operator, we will use Corey type relative permeability curves in the following history matching process to adjust the relative permeability. Therefore, the overall shape of the relative permeability will be different from the current one. Lastly, pore volume of the reservoir as well as fluid in place are listed in Table 4.6. Because the operator is

confident with the original volume of oil in place, we try to keep changes small in pore volume during the history matching process.

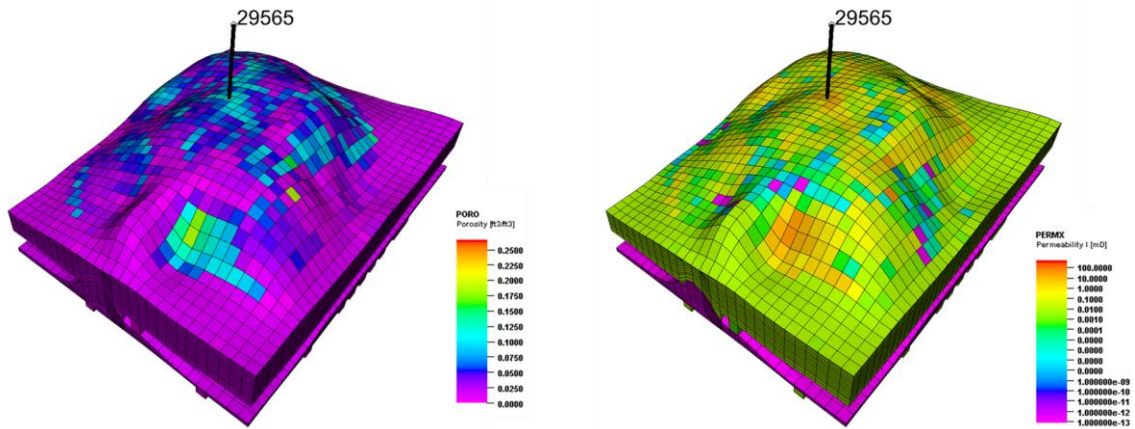


Figure 4.16 Reservoir properties: porosity (left) and permeability (right)

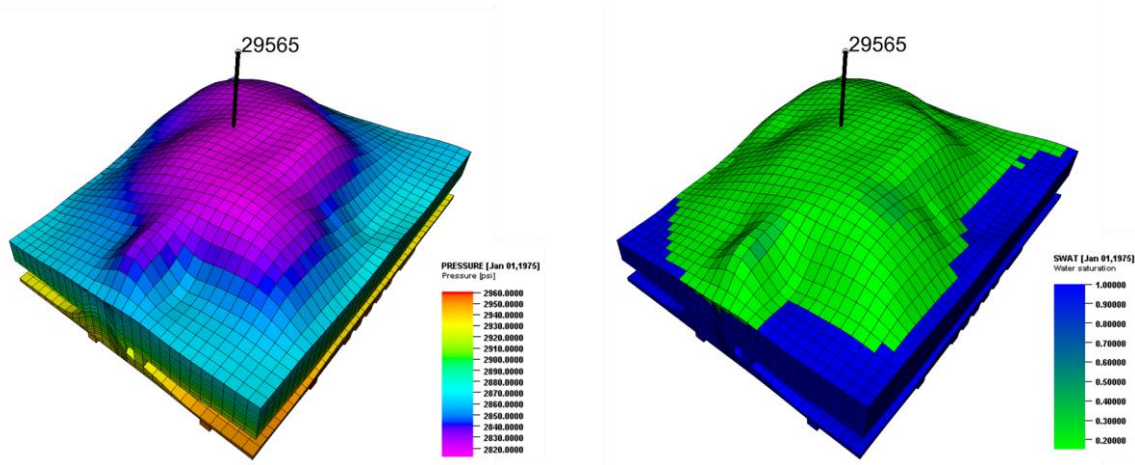


Figure 4.17 Initial pressure (left) and initial water saturation (right)

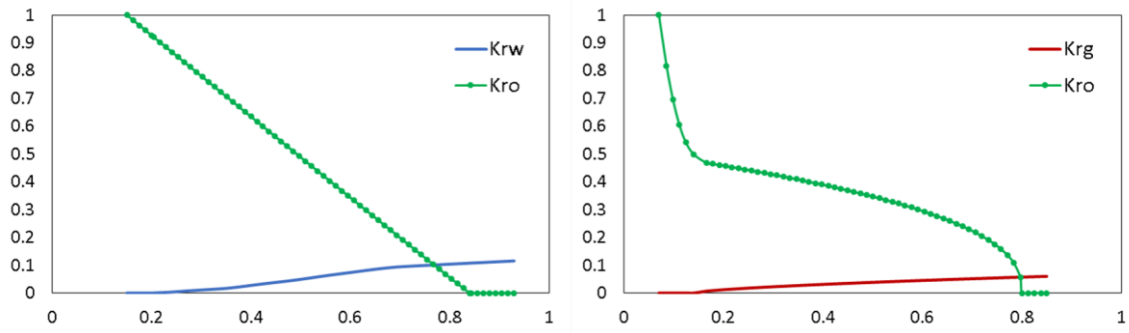


Figure 4.18 Three phase relative permeability curves provided by the operator

Table 4.6 Pore volume and fluid in place of the reservoir

	Finite Difference Simulation
Pore volume (<i>MM res ft³</i>)	118.76
Reservoir volume of oil (<i>MM STB</i>)	3.28
Reservoir volume of water (<i>MM STB</i>)	16.41
Reservoir volume of gas (<i>MM SCF</i>)	3.13

4.5.2 Sensitivity Analysis

The list of parameters in Table 4.7 is considered before history matching to evaluate the impact of each parameter. For this sensitivity study, permeability, pore volume and water saturation are varied using multipliers for the entire reservoir. The relative permeability is modeled using Corey correlation by specifying exponents and endpoints for each phase respectively. As a result, the tornado charts are plotted for the all objective function (oil production rate, gas production rate and average reservoir pressure) by perturbing each parameter from the given base value to low and high values respectively (Figure 4.19). The range of parameters are determined based on experimental data and it is also discussed with an operator. The tornado chart shows that the effect of the endpoint for oil relative permeability is significant and reservoir permeability is also

influential compared to the other parameters. On the other hand, rock compressibility is nearly insensitive to the objective function. Therefore, the rock compressibility was removed from the list of parameters that will be used for history matching. By reducing the number of parameters, the population of each generation during Genetic Algorithm can be decreased accordingly, which can result in more efficient history matching with the fewer number of total simulation runs.

Table 4.7 List of parameters to be considered for history matching

		Base	Low	High
Permeability multiplier		1	0.3	3
Pore volume multiplier		1	0.3	3
Initial water saturation multiplier		1	0.5	2
Rock compressibility (1/psi)		0.1e-6	0.1e-6	3.0e-5
kvkh		0.1	0.05	1.0
Relative permeability endpoint	kro	0.8	0.5	1.0
	krog	0.8	0.5	1.0
	krw	0.7	0.35	0.9
	krg	0.1	0.01	0.5
Relative permeability exponent	no	3	1	5
	nog	3	1	5
	nw	3	1	5
	ng	3	1	5

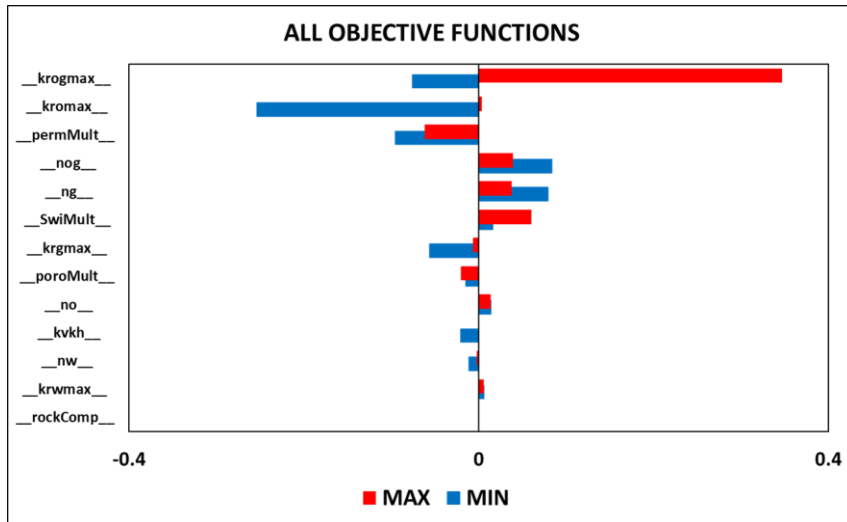


Figure 4.19 Tornado chart for all objective functions

4.5.3 Primary Depletion

Beginning with 1st stage of hierarchical history matching for the primary depletion period, Figure 4.20 shows the performance of Multi-objective Genetic Algorithm. Compared to an initial generation, the misfit of average reservoir pressure as well as oil production rate for updated models after 15th generation has been reduced as it forms the Pareto front.

As a further comparison, several optimal solutions have been selected among population of the final generation and simulation responses are compared with the observed data in Figure 4.21. The match quality of all objective functions is in an acceptable range for most of the updated models where the best model is represented as blue line.

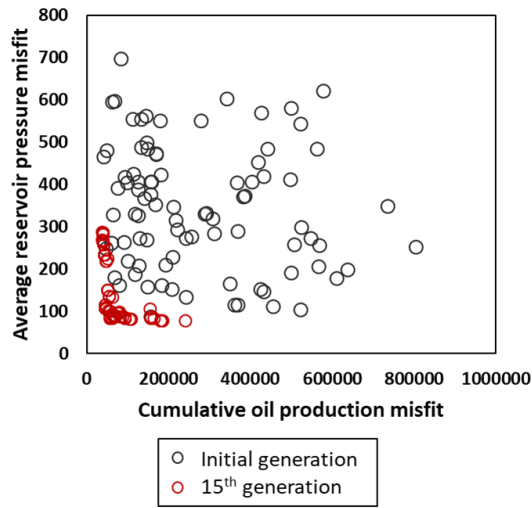


Figure 4.20 Performance of MOGA for primary depletion

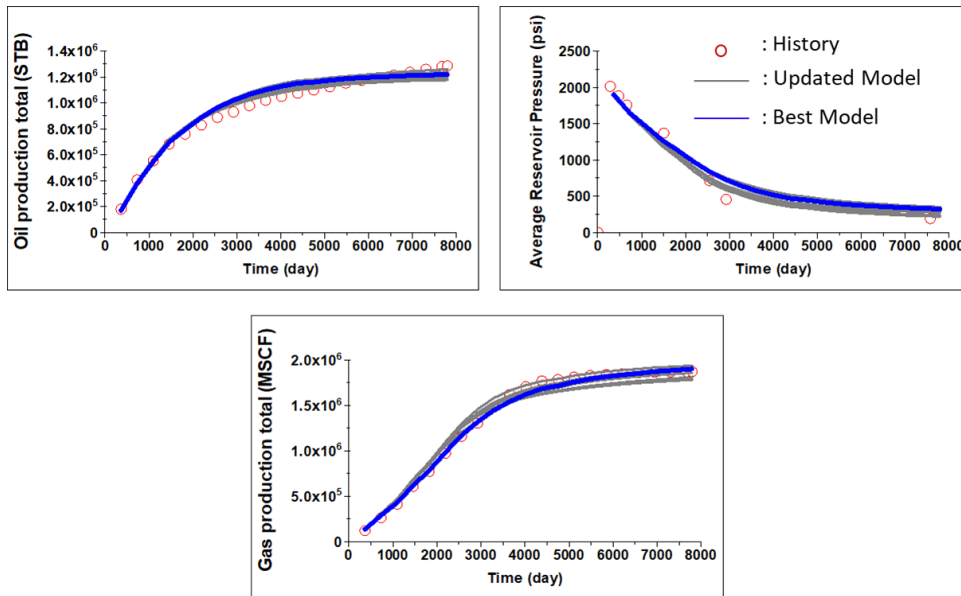


Figure 4.21 Comparison of simulation responses of the history matched model with the observed data for primary depletion

Depending on the influence of each objective function, optimal solutions can be divided into three groups as described in Figure 4.22. Group 1 represents a good match

with oil production while there is inconsistency in average reservoir pressure. In contrast, Group 3 has low average reservoir misfit whereas models cannot meet oil production as shown in observed data. Group 2 shows intermediate level of misfit for both objective functions including oil production and average reservoir pressure, which indicates optimal solutions in this history matching process. In this first stage of history matching, we adjusted not only reservoir properties but also EOS models that have been selected from the previous fluid model calibration. In Figure 4.23, histograms of EOS models for each group respectively are demonstrated. It can be seen that EOS models from high oil formation volume factors are not included in the final generation. In addition, EOS model #4 and #5 are dominant in general but especially in Group 2. The comparison of phase behaviors of those two fluid models are also represented in Figure 4.24.

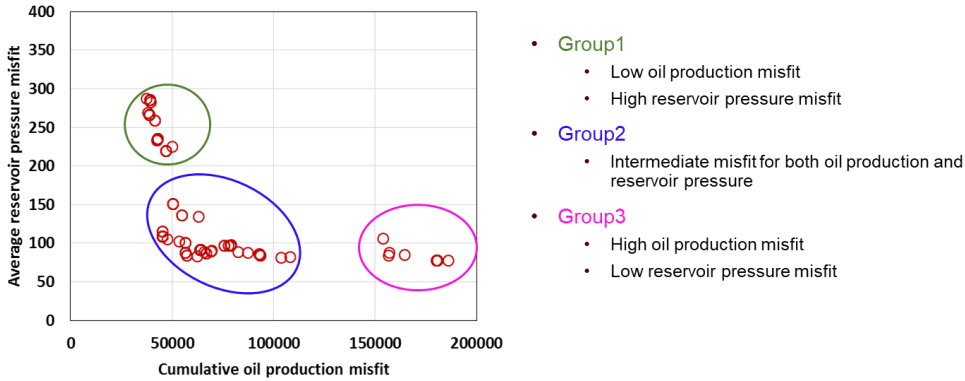


Figure 4.22 Three different groups in optimal solutions depending on the importance of objective functions

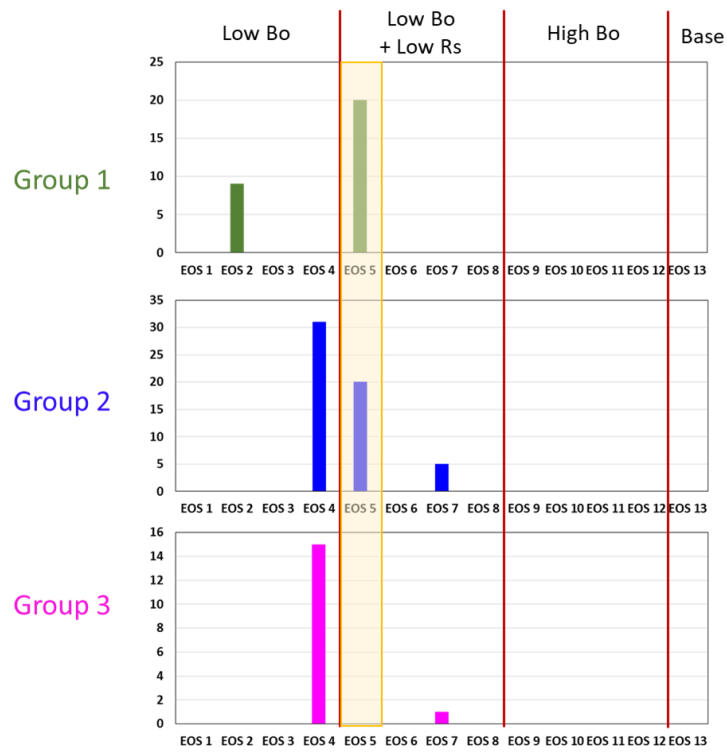


Figure 4.23 Histogram of EOS models for each group

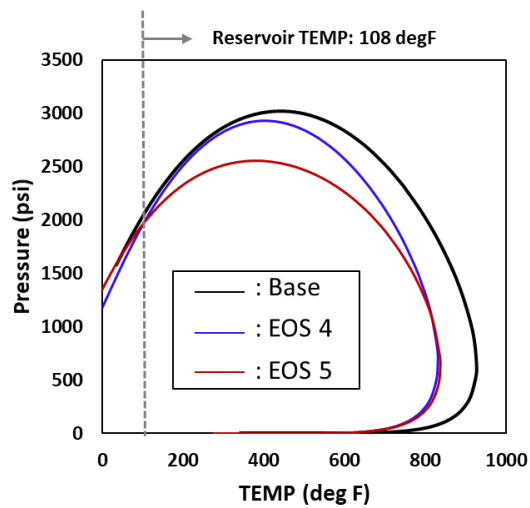
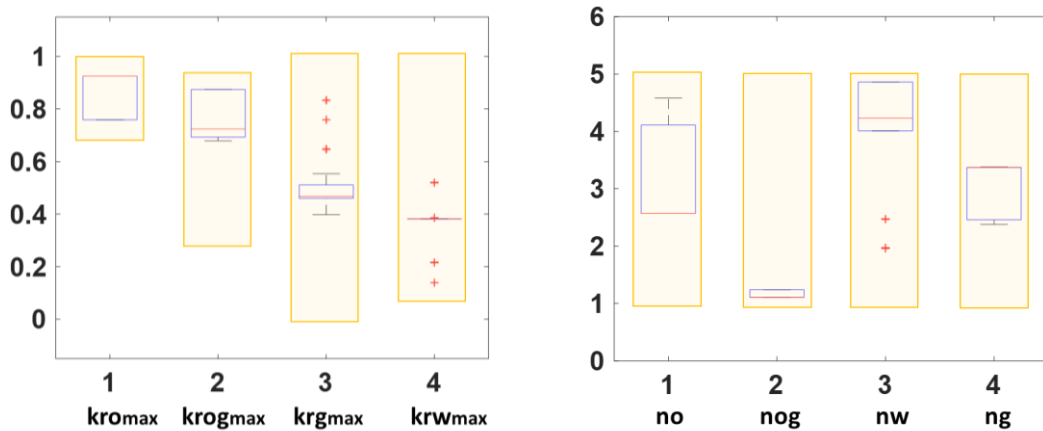


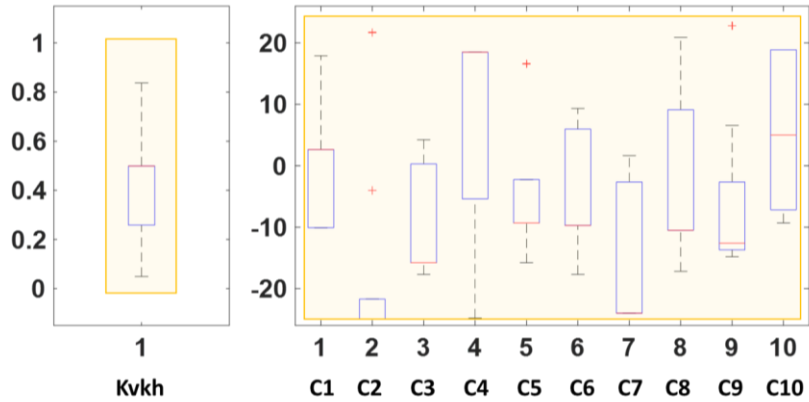
Figure 4.24 Comparison of phase behavior

Moving on to the investigation of other calibrated parameters, Figure 4.25 presents box plots of each parameter. In the box plot, yellow boxes represent the ranges that we specified in the beginning. It has been observed that endpoints of relative permeability for all phases have been reduced overall, where the endpoints for oil are converged to the higher value. The distribution of pore volume multipliers is narrowed down significantly where pore volume of region 1~4 decreases whereas pore volume of the rest of regions increases. On the other hand, there are still some level of uncertainties in the permeability multiplier, which we can continue to reduce in the next stages of history matching process where we further include more production periods.

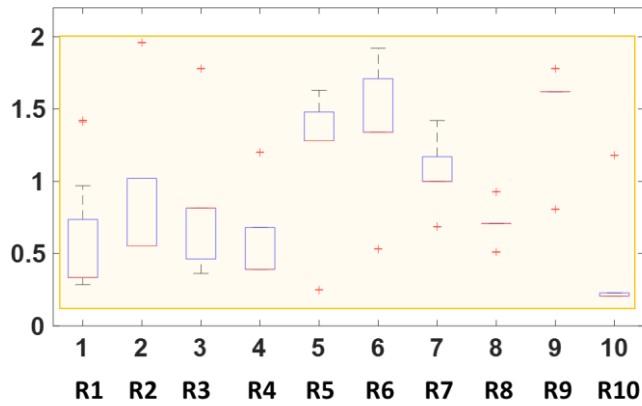


(a) Endpoints of relative permeability (b) Exponents of relative permeability

Figure 4.25 Box plots of calibrated parameters for primary depletion



(c) Vertical horizontal ratio and GCT coefficients



(d) Pore volume multipliers

Figure 4.26 Continued

In Figure 4.27, we show the comparison of simulation responses with the observed data for the best match model including the water production. As explained before, due to the reliability issue of water production as well as the lack of water saturation distribution, water production was not considered as the objective functions. The relative permeability curves for the best case are presented as compared with the previous relative permeability

curve provided by an operator (Figure 4.28). It can be seen that oil and gas relative permeability increases in general whereas the ability for water to flow has been decreases.

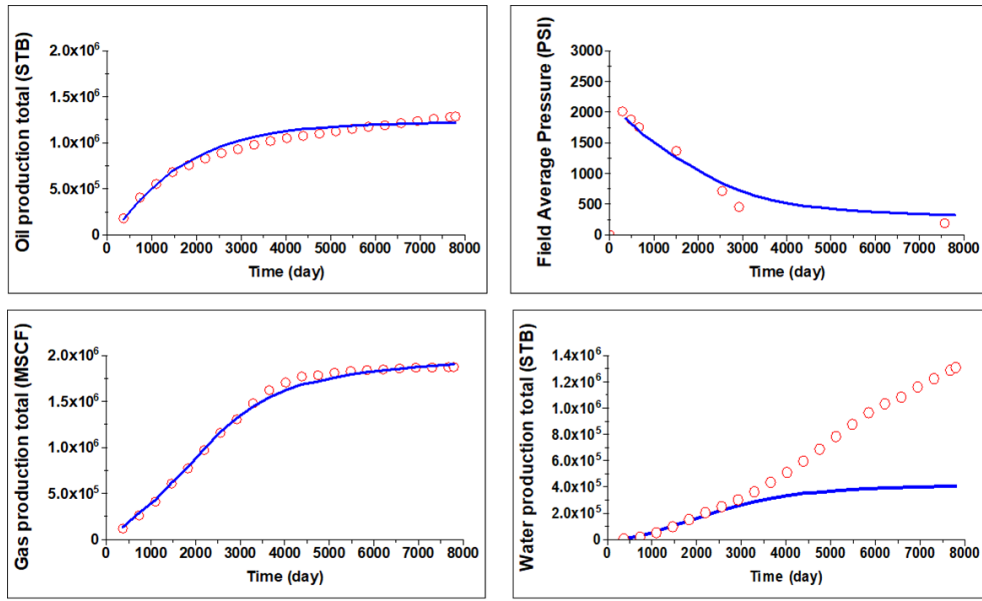


Figure 4.27 Comparison of simulation responses of the best updated model with the observed data

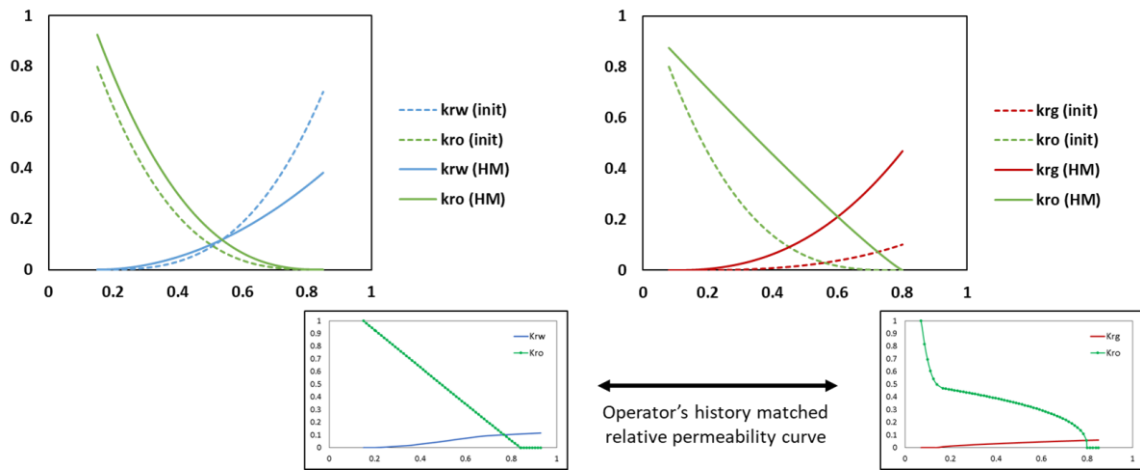


Figure 4.28 Comparison of relative permeability before and after history matching during primary depletion

4.5.4 Enhanced Oil Recovery

In Dover 33 field, there was an enhanced oil recovery project utilizing carbon dioxide after 20 years of primary depletion. Although the history matching process for primary recovery is performed successfully, the updated model is not able to match historical fluid production as shown in Figure 4.29. Therefore, a further model calibration including the EOR period needs to be conducted with the reduced ranges of parameters, such as GCT coefficients for reservoir permeability and pore volume multipliers, which are used in the previous stage of history matching. However, we will apply different relative permeability curves for the EOR period as CO₂ is injected into the reservoir.

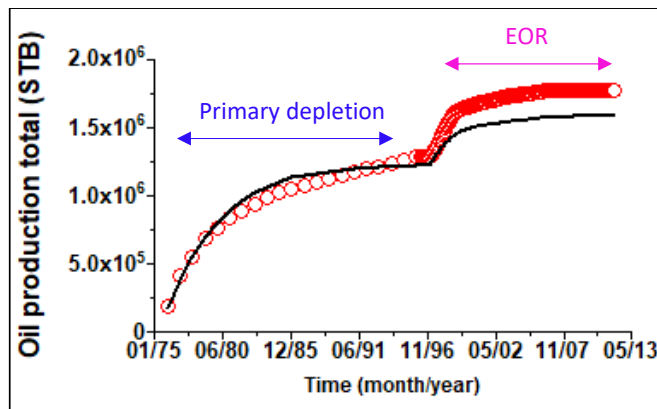


Figure 4.29 Comparison of cumulative oil production with the updated model from primary depletion

Before performing history matching for the EOR period, the selected EOS model from the previous stage has been examined in terms of a phase behavior as well as physical properties of oil-CO₂ mixtures to see the impact of CO₂ injection. First, the comparison of phase behavior for three different CO₂ and oil mixtures with respect to different CO₂ mole

fractions has been made (Figure 4.30). Then, Minimum Miscibility Pressure (MMP) has been determined by a slimtube test at the pressure of around 1350 psi, which indicates that supercritical CO₂ is employed to displace the oil in the reservoir where the pressure is greater than 1350 psi and eventually to improve the oil recovery (Figure 4.31). In addition, as CO₂ dissolves in oil, it has a substantial impact on the swelling of crude oil, which eventually leads to an increase in oil mobility as shown in Figure 4.32. The swelling factor is defined as a volume of mixture at a saturation pressure per a volume of the original fluid at its saturation pressure. Lastly, the density of oil-CO₂ mixtures for 50% CO₂ mole fraction is compared with that of original fluid (Figure 4.33). It can be seen that the density of mixtures increases with the added CO₂.

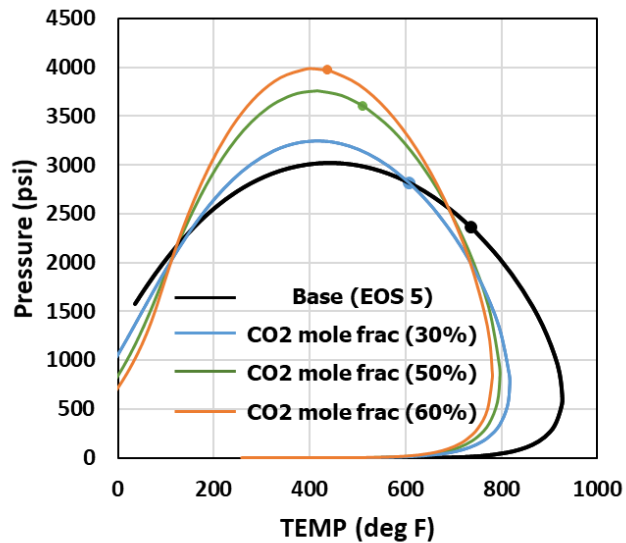


Figure 4.30 Comparison of phase diagram for different oil and CO₂ mixtures

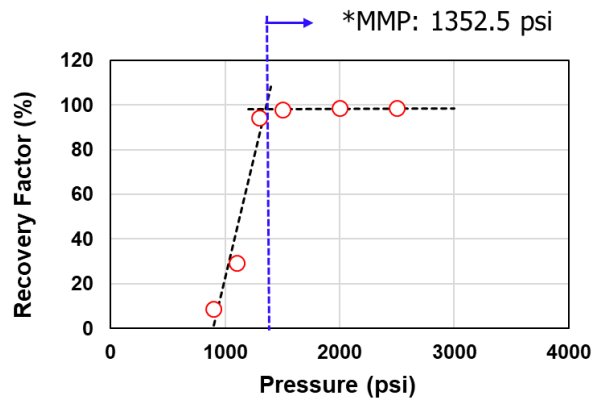


Figure 4.31 Determination of Minimum Miscibility Pressure (MMP)

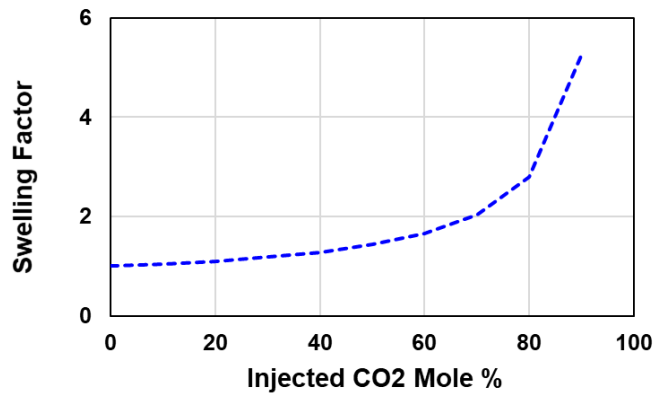


Figure 4.32 Swelling factor of EOS 5

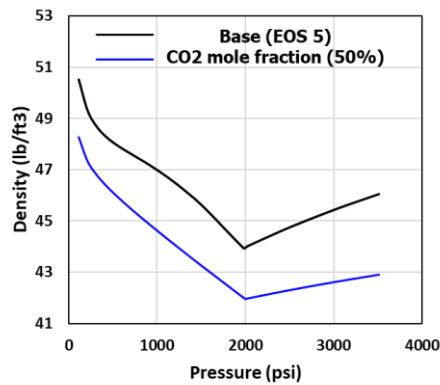


Figure 4.33 Density of original fluid compared with oil and CO₂ mixture (CO₂ mole fraction of 50%)

For the second stage of history matching, we also consider three objective functions, which are the misfits of average reservoir pressure, cumulative oil production and cumulative gas production respectively. All objective functions are evaluated during the primary production and EOR period as well. We also continue to utilize Multi-objective Genetic Algorithm to effectively optimize all objective functions simultaneously. Figure 4.34 shows the results of MOGA indicating the significant reduction of misfits after 17th generation. Solutions from the final generation are forming the Pareto front whereas models from an initial generation are scattered to cover all possible solutions in the beginning. In Figure 4.35, the comparison of simulation responses against the observed data is presented for one of the updated models from MOGA. It can be seen that they are showing a good agreement.

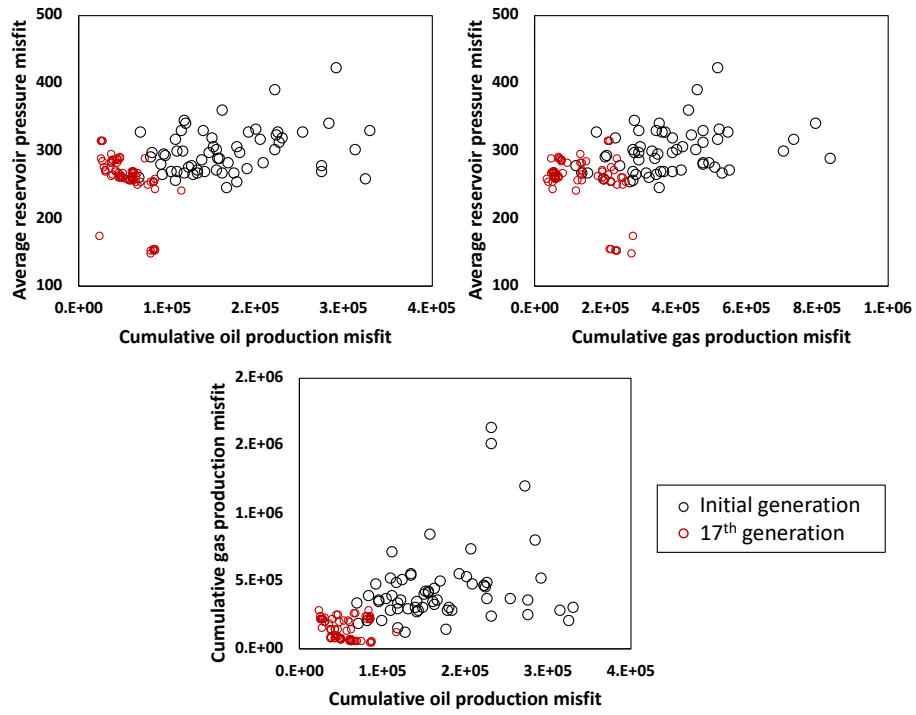


Figure 4.34 Performance of MOGA for CO₂ EOR period

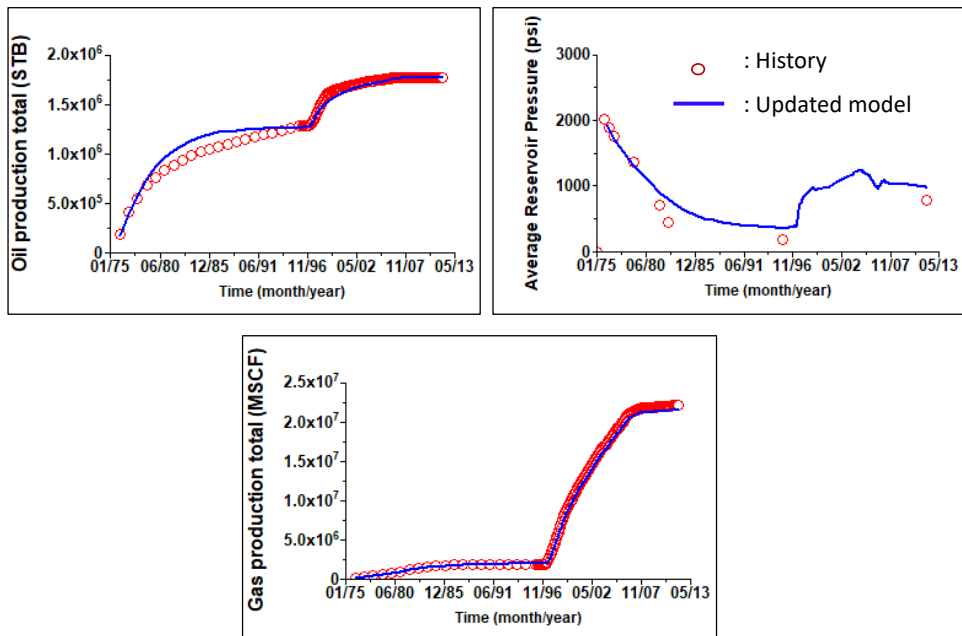


Figure 4.35 Comparison of simulation responses of the history matched model with the observed data for CO₂ EOR period

As for the parameters that have been calibrated through the second stage of history matching, the distribution of each variables is now presented. First, most of endpoints and exponents of relative permeability for the EOR period are converged well except for the exponent of gas relative permeability (Figure 4.36). Compared to the relative permeability curves for primary production (Figure 4.37), gas-oil relative permeability curves are quite analogous whereas water-oil relative permeability curves are fairly different. In the water-oil relative permeability curve, it can be seen that oil relative permeability increases compared to the one for primary depletion due to the effect of CO₂ injection. In addition, it is noted that the shape of relative permeability curves seems to be more reasonable compared with operator's history matched ones. Then, the distributions of GCT coefficients and pore volume multipliers are shown in Figure 4.38 and Figure 4.39. The ranges of each parameter are further narrowed down during the second stage of history matching.

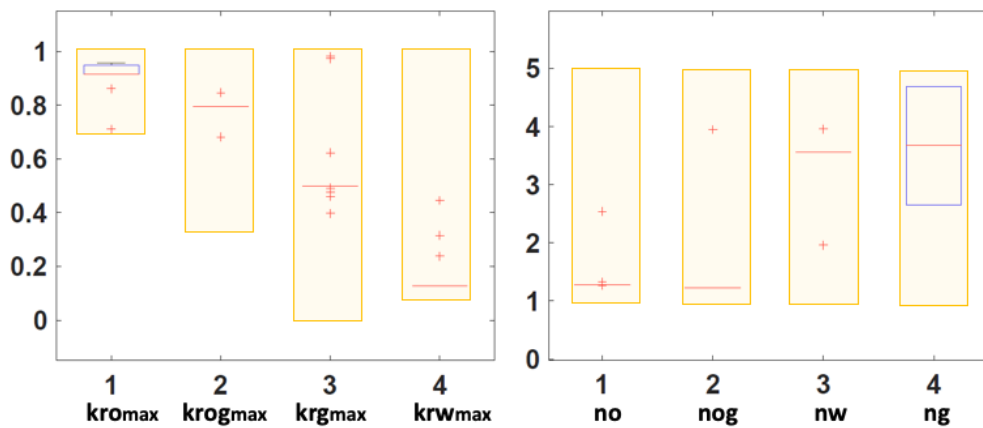


Figure 4.36 Box plots of parameters associated with relative permeability: endpoints (left) and exponents (right)

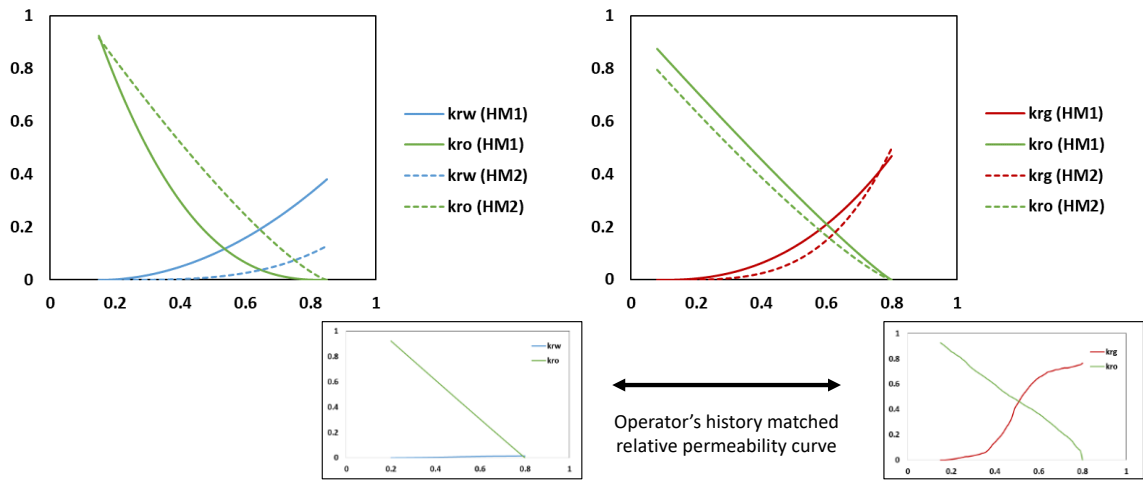


Figure 4.37 Comparison of relative permeability before and after history matching during CO₂ EOR period

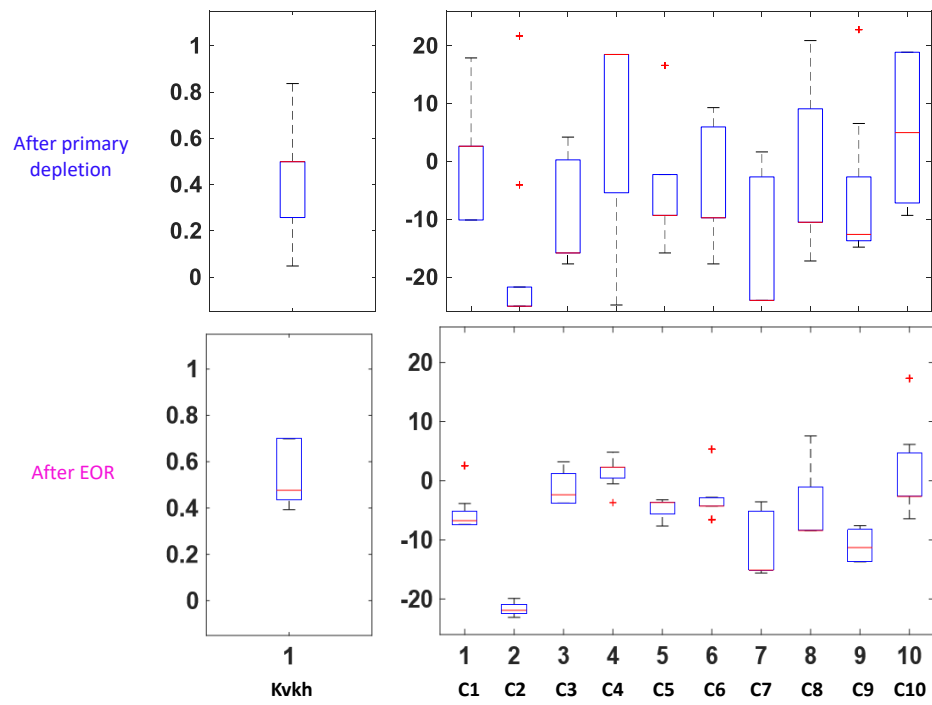


Figure 4.38 Comparison of distribution for parameters associated with permeability between after primary depletion and after EOR period

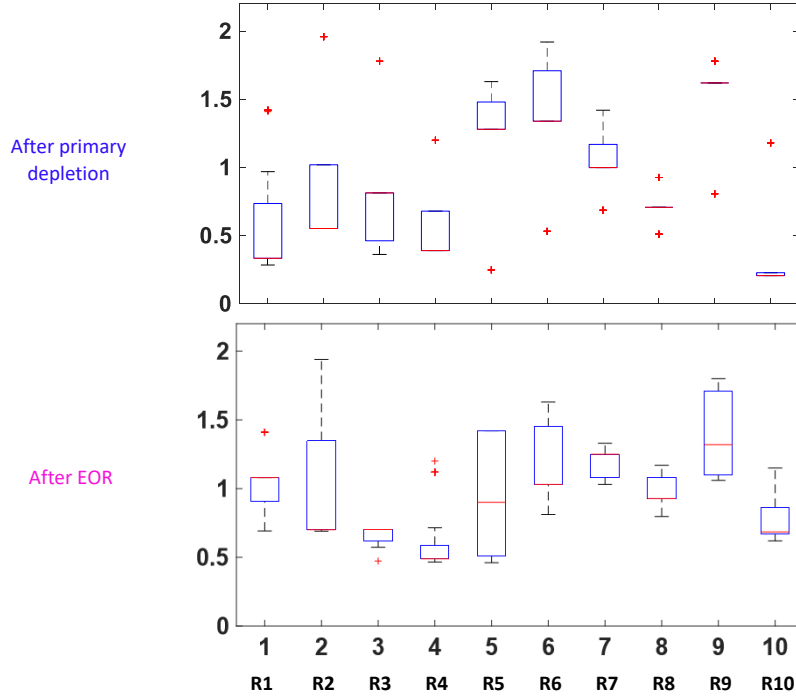


Figure 4.39 Comparison of distribution for pore volume multipliers between after primary depletion and after EOR period

4.5.5 CO₂ Injection Only Period

After the primary production followed by the enhanced oil recovery using carbon dioxide, there is a CO₂ injection only period for the purpose of CO₂ sequestration. One of the history matched models from the first and second stage of model calibration process is used to simulate this period. However, when bottomhole pressure is predicted during CO₂ injection only period, the behavior of bottomhole pressure in an injector is not well matched with the measured data that shows the sharp increasing trend (Figure 4.40). Moreover, a sudden increase in pressure response occurs with a reduced injection rate as shown in Figure 4.41. Therefore, additional reservoir model calibrations are required to capture an abrupt rise of bottomhole pressure, which eventually includes entire production

periods from primary depletion to CO₂ injection only period. In this stage, the range of parameters that is narrowed down from the previous history matching is carried over to preserve the previous matching quality.

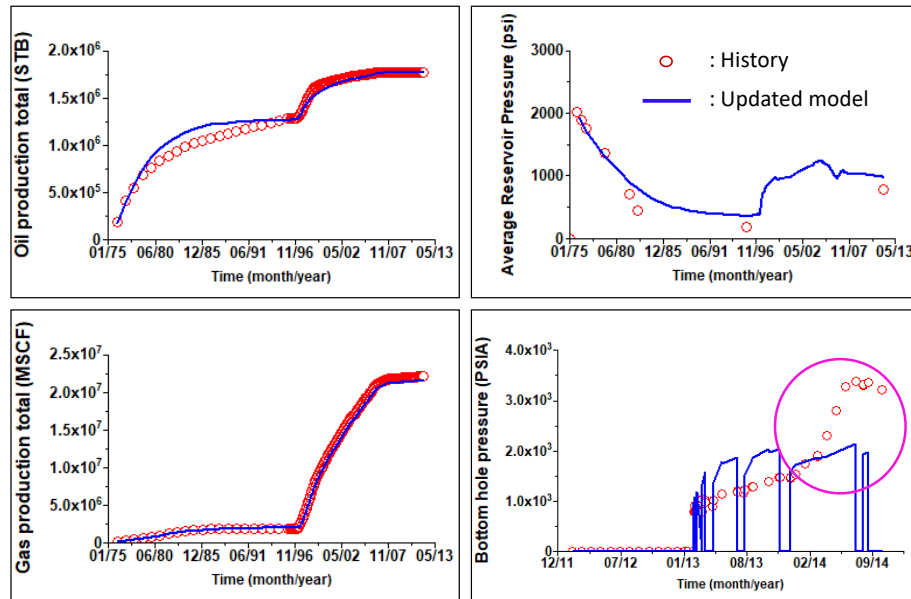


Figure 4.40 Comparison of simulation responses of the history matched model with the observed data (BHP: prediction)

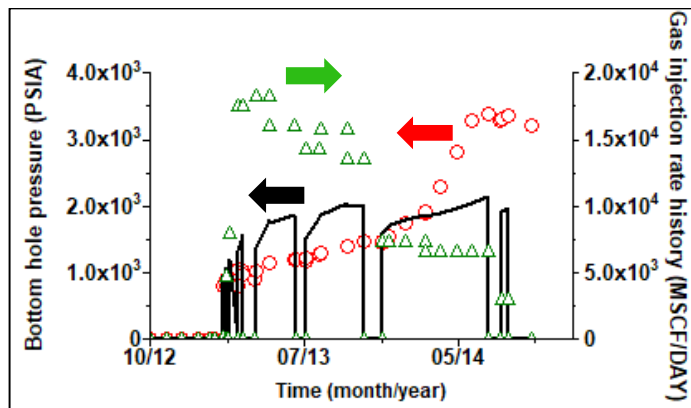


Figure 4.41 Difference in bottomhole pressure between simulation response and the measure data in comparison to the reduced gas injection rate

As a result of a third stage of history matching using MOGA, objective functions are significantly reduced after several generations (Figure 4.42). In this stage, three objective functions are the misfit of cumulative oil production, average reservoir pressure and bottomhole pressure of the injector. Even though the match quality of bottomhole pressure has been improved compared to the previous model (Figure 4.43), the misfit of average reservoir pressure increases especially during the EOR period, which indicates that two objective functions are conflicting with each other.

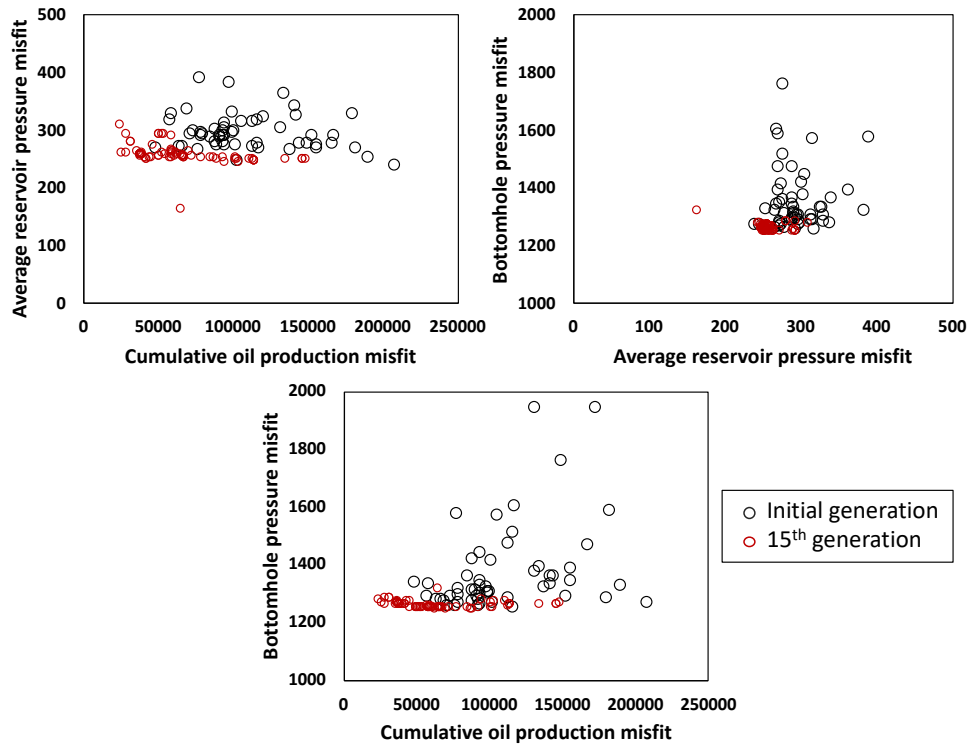


Figure 4.42 Performance of MOGA for CO₂ injection only period

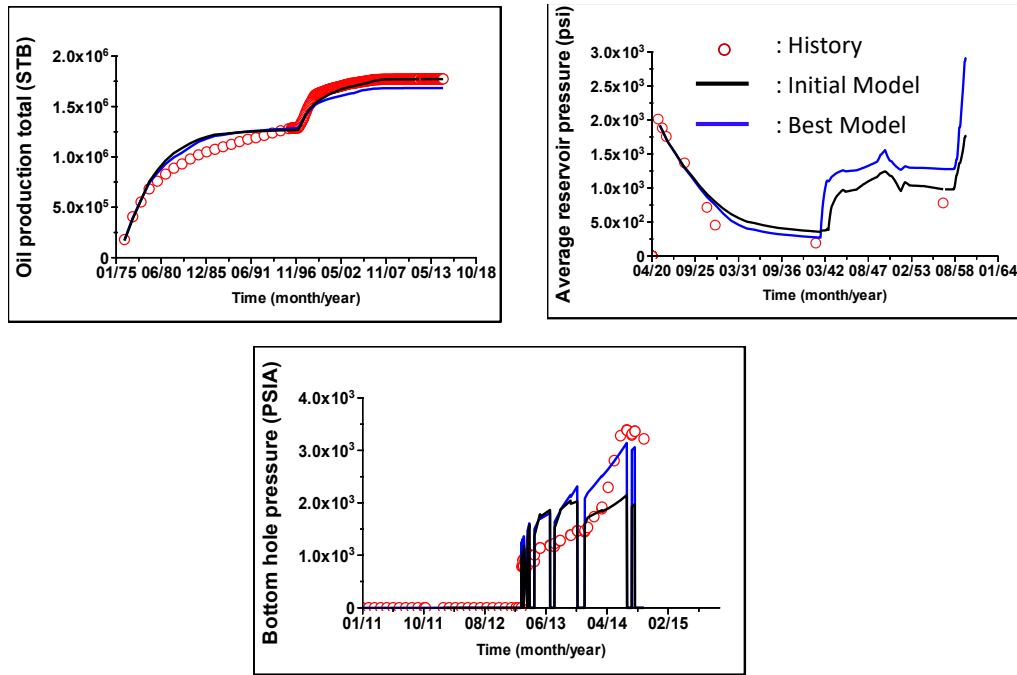


Figure 4.43 Comparison of simulation responses of the history matched model with the observed data for CO₂ injection only period

In terms of parameters that have been calibrated through several stages of history matching, reservoir permeability and pore volume related parameters are even further narrowed down (Figure 4.45 and Figure 4.46) whereas exponents and endpoints of relative permeability are more widely distributed than the previous history matching (Figure 4.44). This is because the range including outliers is provided to allow some level of flexibility. In addition, less convergence of these parameters represents difficulties in achieving the conflicted objective functions especially between average reservoir pressure and bottomhole pressure of the injector.

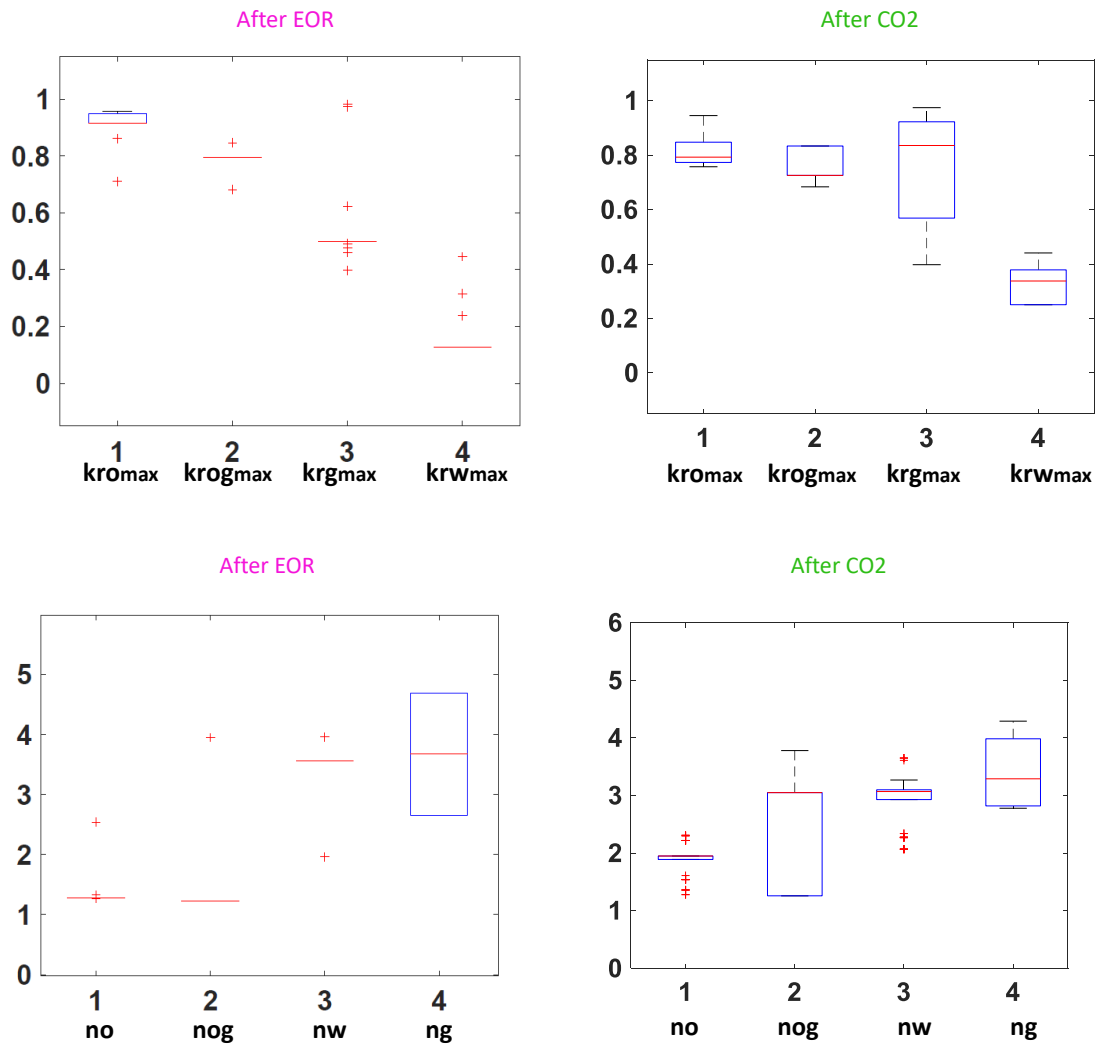


Figure 4.44 Comparison of distribution for parameters associated with relative permeability between after EOR period and after CO₂ injection only period: endpoints (top) and exponents (bottom)

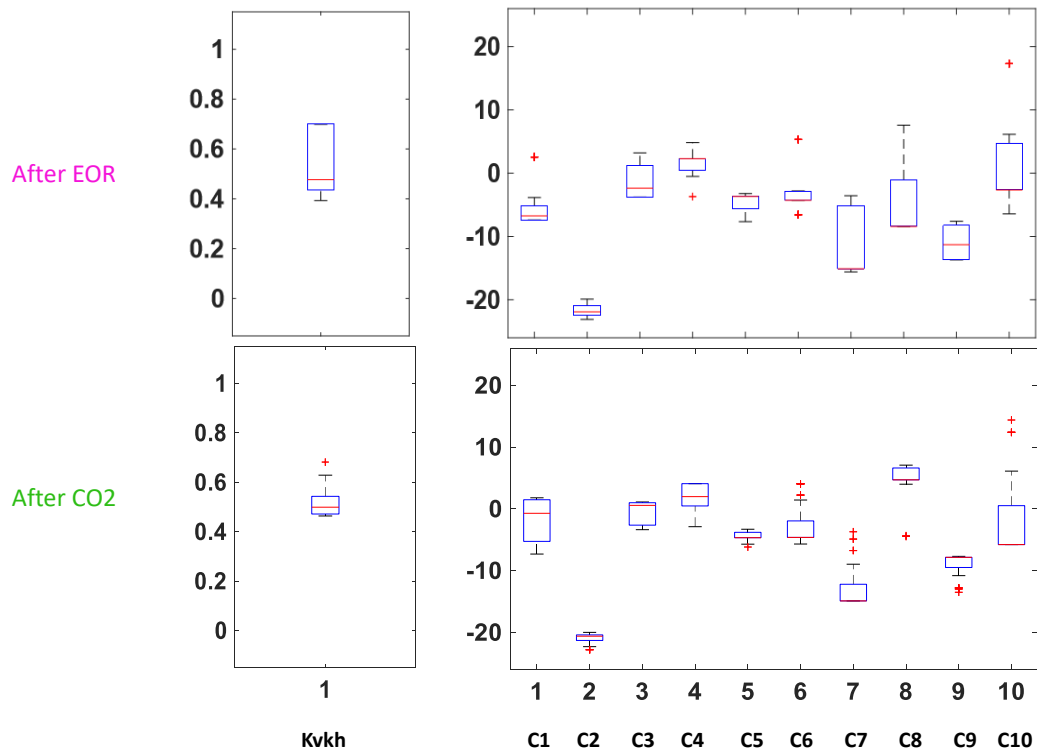


Figure 4.45 Comparison of distribution for parameters associated with permeability between after EOR period and after CO₂ injection only period

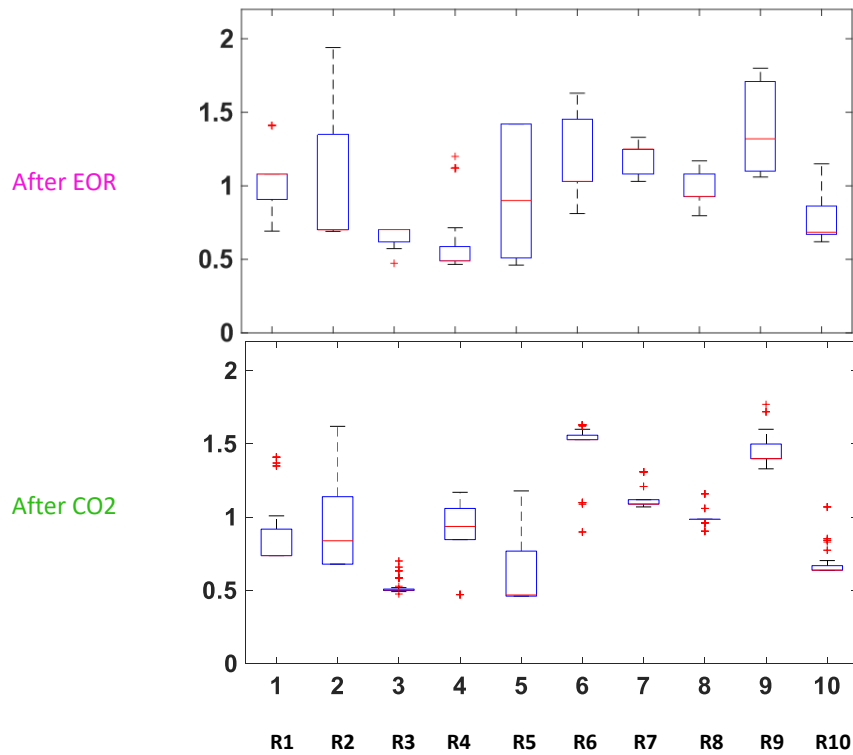


Figure 4.46 Comparison of distribution for pore volume multipliers between after EOR period and after CO₂ injection only period

Although Multi-objective Genetic Algorithm has been used to solve multi-objectives problems in the previous history matching, it was not sufficient to minimize misfits of all objective functions simultaneously. Therefore, GA with a single objective function, which only focuses on the misfit of bottomhole pressure, has been performed to investigate parameters that makes difference (Figure 4.47). As shown in Figure 4.48, the simulated response of the updated model from GA is better matched with the observed data than the one from MOGA as well as the initial model.

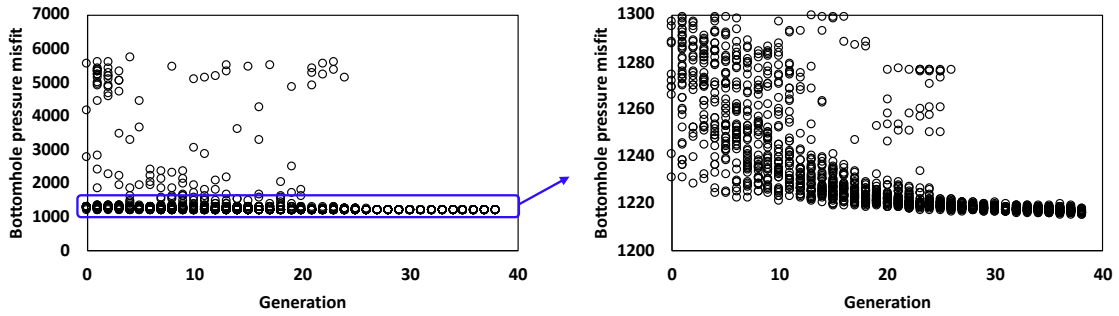


Figure 4.47 Results of Genetic Algorithm with a single objective function

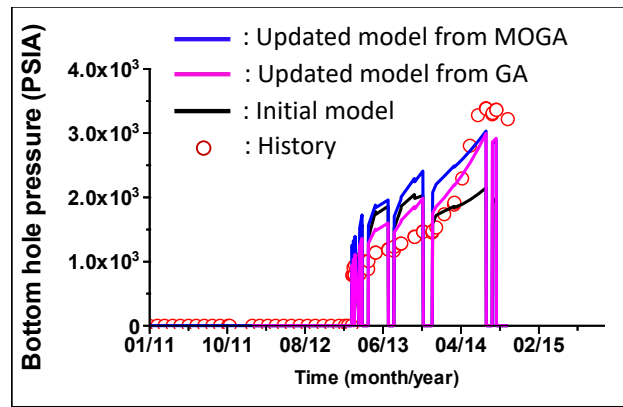


Figure 4.48 Comparison of bottomhole pressure between updated models and history data

4.5.6 Discussion

As a hierarchical history matching for all production periods is finished, the bottomhole pressure of two monitor wells (Figure 4.49) during CO₂ injection only period has been compared as a validation. Figure 4.50 and Figure 4.51 show that the simulated responses of the bottomhole pressure from the two last updated models (one from the Multi-objective GA and the other from the single GA) are well matched with the observed data, which indicates that history matchings have been performed successfully.

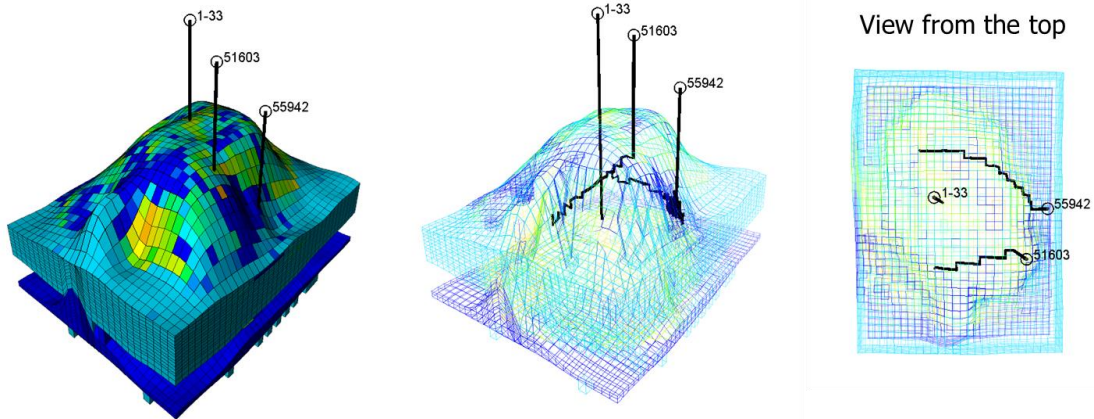


Figure 4.49 Location of monitor wells

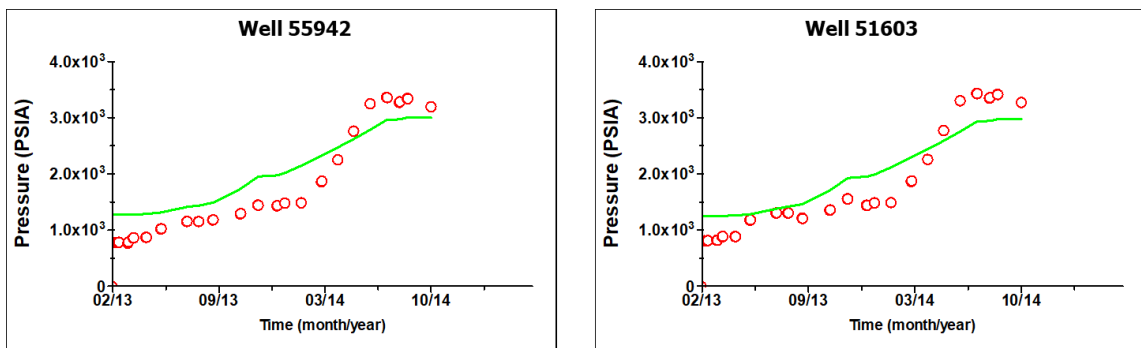


Figure 4.50 Comparison of the bottomhole pressure for two monitor wells: the history matched model from MOGA

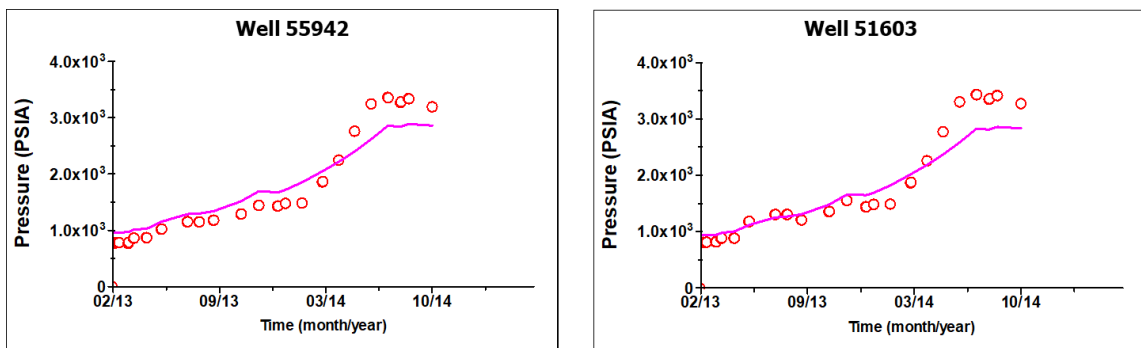


Figure 4.51 Comparison of the bottomhole pressure for two monitor wells: the history matched model from GA

It has been noticed that there is an apparent difference in pore volume multipliers especially for region 6 and region 8 (Figure 4.52). In other words, pore volumes of regions around the injector has been reduced to achieve better bottomhole pressure match, which indicates the possibility of pore volume reduction during CO₂ injection. Also, as shown in the comparison of the histogram of pore volume for history matched models at every stage (Figure 4.53), higher and lower part of pore volume in the last updated model (After CO₂ only) have been decreased to obtain a better match for bottomhole pressure whereas pore volume in the middle has been increased, compared to the previous history matched models.

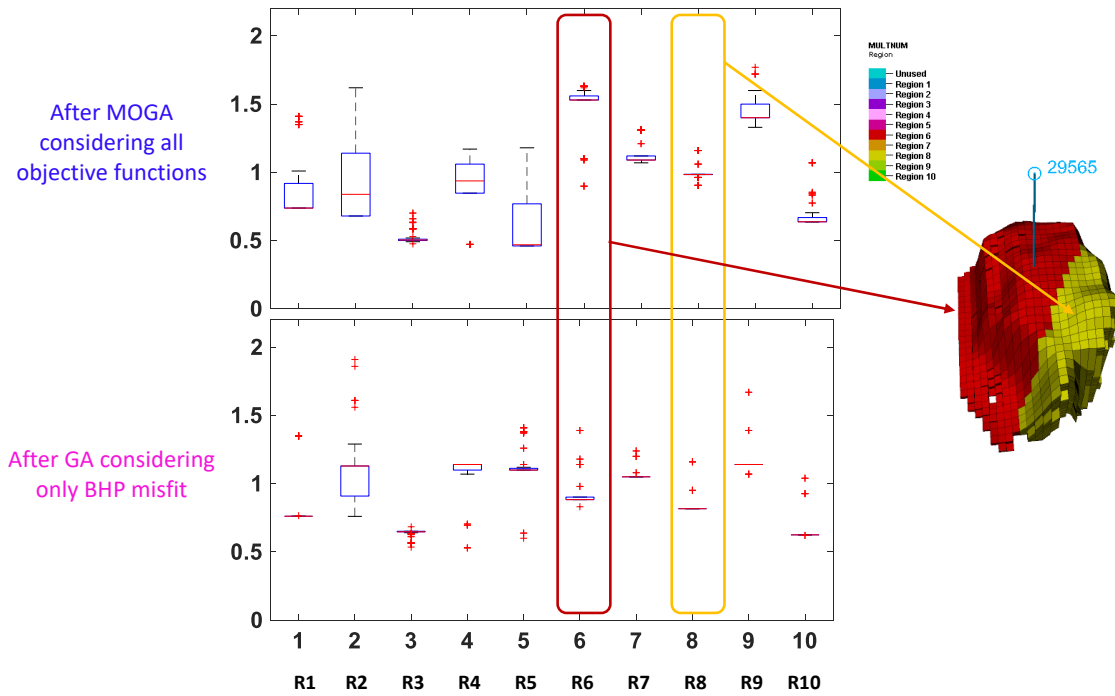


Figure 4.52 Comparison of distribution of pore volume multipliers between MOGA results and GA results

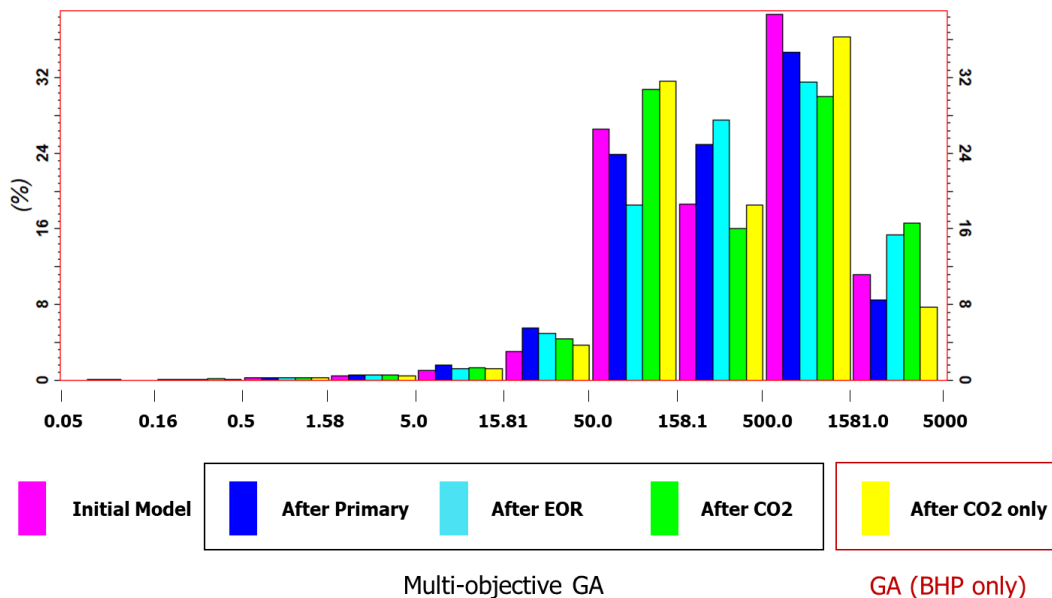


Figure 4.53 Comparison of the histograms of pore volume for the updated models

In addition, the permeability distribution has been investigated among the history matched models. Compared to an initial model, overall permeability has been increased as several stages of history matching have been performed (Figure 4.54). There has been an increase in the higher permeability while the lower part of permeability has been reduced. More specifically, the difference in the permeability between the history matching during EOR period and the history matching during CO₂ injection only period has been examined. As shown in Figure 4.55 and Figure 4.56, there has been an increase in permeability around regions between an injector and producer ‘51603’ whereas permeability for the regions around producer ‘55942’ has been decreased. For the last updated model from the single GA, an increase of permeability is more noticeable, compared with the updated model during CO₂ injection only period using the Multi-

objective GA. Lastly, the permeability of the last updated model from the single GA is presented in the Figure 4.57 and Figure 4.58 with the certain threshold to see the characteristics of permeability distribution. As shown in Figure 4.57, all three wells are connected with a higher permeability channel, whereas the lower permeability regions are located at the upper part of the reservoirs (Figure 4.58), which might be the cause of the sharp increasing trend of the bottomhole pressure during the last stage of production period.

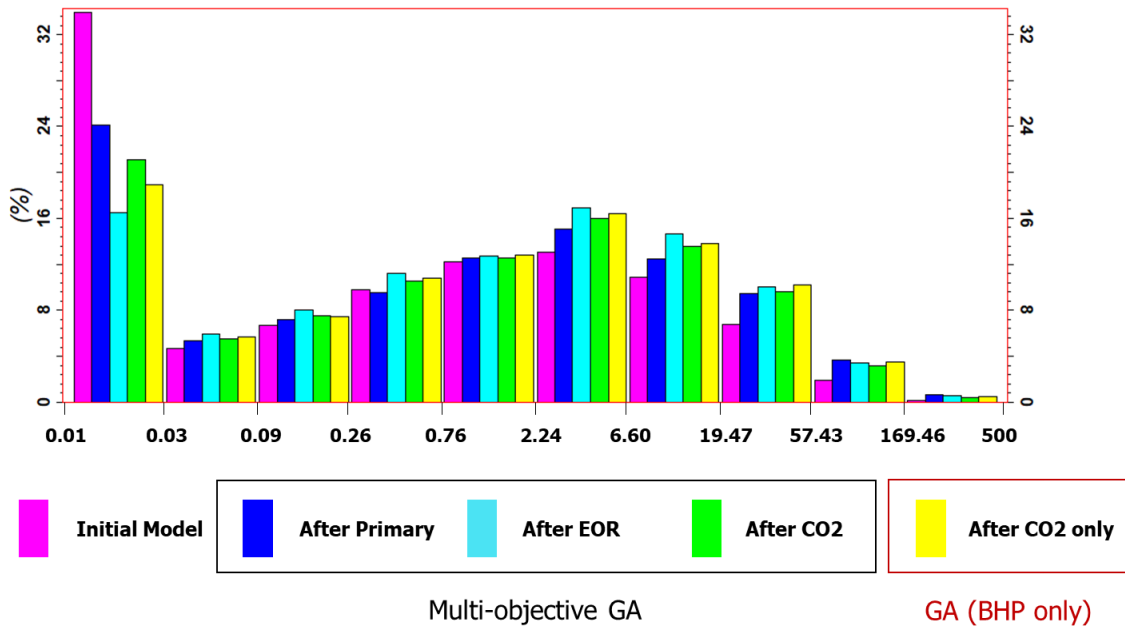


Figure 4.54 Comparison of the histograms of permeability for the updated models

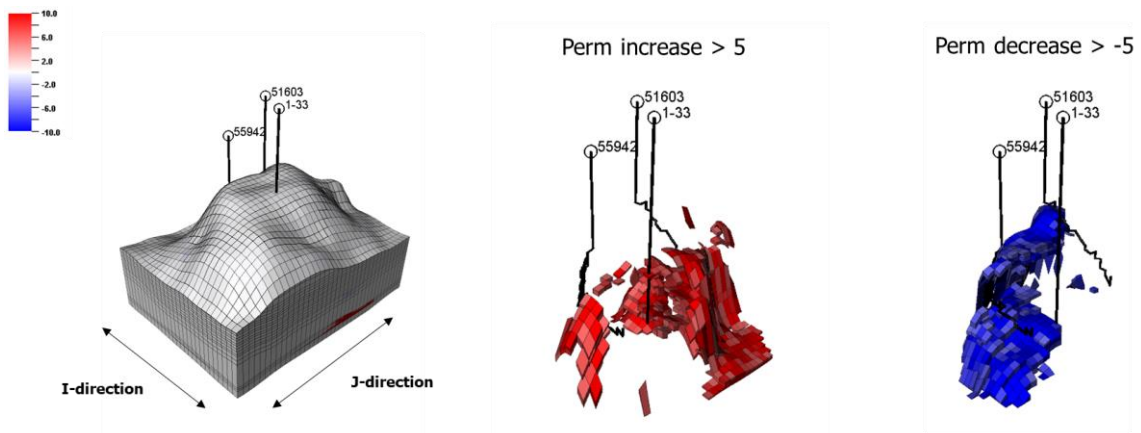


Figure 4.55 Difference in permeability (CO₂ injection only period (GA) and CO₂ EOR period)

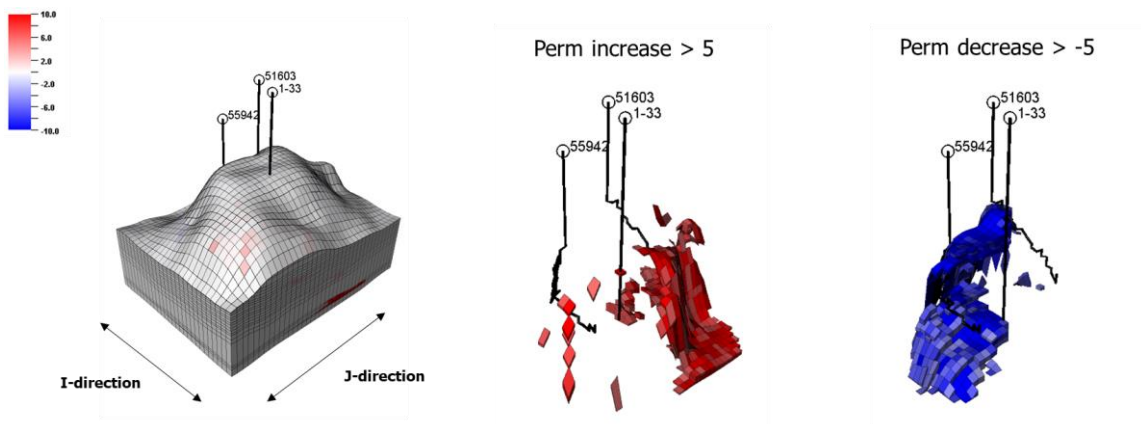


Figure 4.56 Difference in permeability (CO₂ injection only period (MOGA) and CO₂ EOR period)

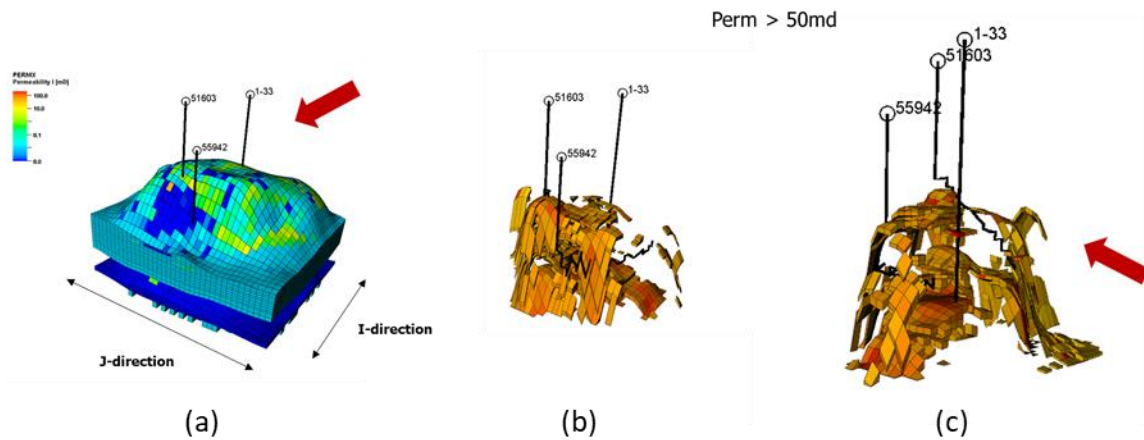


Figure 4.57 Permeability of CO₂ injection only period after GA: (a) permeability distribution (b) and (c) with the high threshold (Perm > 50md) from two different perspective

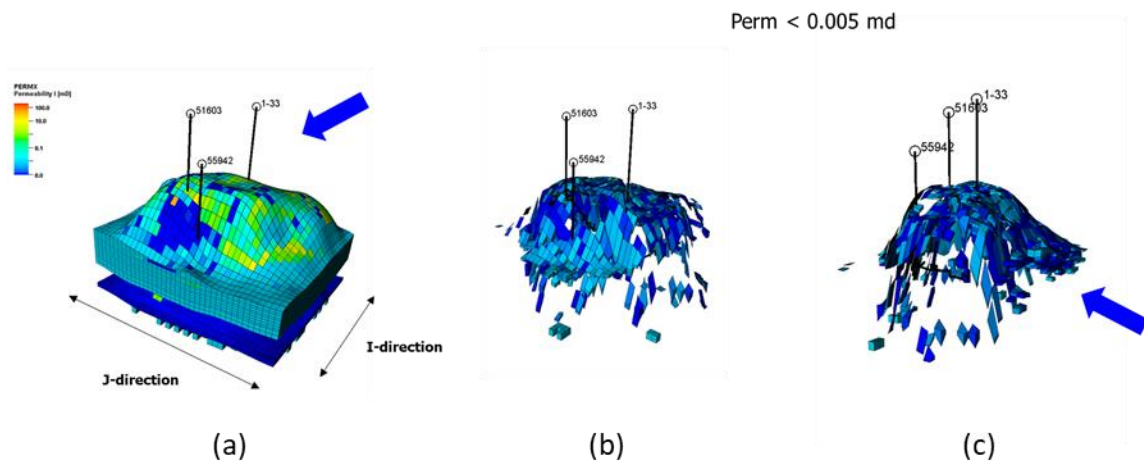


Figure 4.58 Permeability of CO₂ injection only period after GA: (a) permeability distribution (b) and (c) with the low threshold (Perm < 0.005md) from two different perspective

4.6 Conclusions

In this chapter, we proposed the workflow of a multi-stage model calibration that involves a fluid model adjustment and a reservoir model calibration in the Dover 33 field.

Due to the lack of reliability in the initial fluid model provided by the operator, parameters in the EOS model have been changed using the Genetic Algorithm that leads to several updated models. Then, the sensitivity analysis has been performed to investigate the impact of parameters in history matching. With the results of the fluid model calibration and the sensitivity study, the history matching process has been divided into three stages based on its production period to calibrate reservoir parameters in a hierarchical manner. Following conclusions are obtained below:

- The uncertainty in the original fluid model that has been determined with the limited number of experimental data has been reduced by conducting the fluid model calibration. In this model calibration, three different oil formation volume factors are assumed to obtain updated fluid models that have distinct characteristics.
- As a result of incorporating an EOS model as one of the parameters in the reservoir model calibration during primary depletion, Multi-objective Genetic Algorithm proves to be an efficient in finding optimal solutions that show a good agreement for all objective functions respectively. While history matched models have been obtained, the uncertainty in parameters is also substantially reduced.
- In the following history matching during the CO₂ EOR period as well as the CO₂ injection only period, parameters are further narrowed down with acceptable matching results. It has been noticed during the last stage of history matching that there are difficulties in finding optimal solutions for both oil productions and pressure responses. In comparison, the results of single objective Genetic

Algorithm that only accounts for bottomhole pressure responses, possible pore volume reductions during the CO₂ injection in regions around an injector has been indicated to capture the sharp increasing trend.

CONCLUSIONS

In this dissertation, we demonstrated an efficient approach in the application of an enhanced oil recovery using Multi-objective Genetic Algorithm. In addition, the extension of Fast Marching Method to multi-well problems was investigated with the improved calculation of inter-partition transmissibility that enables us to model the communication between partitions where we independently build 1-D simulation models respectively. This research involved comprehensive simulation studies that have been applied to the optimization of chemical EOR, the performance of unconventional reservoirs and field history matching. Some conclusions from this research are summarized as follows:

- Wettability alteration using surfactant based nanofluids has shown the feasibility as a promising EOR mechanism in tight oil reservoirs. As the oil-wet system is changed toward the more water-wet conditions, relative permeability and capillary pressure are altered accordingly. As a result, an additional oil recovery has been achieved. In addition, the efficiency of chemical usages has been optimized while maximizing incremental oil production with Multi-objective optimization process. It is noticed that high oil gains with the efficient usage of surfactants can be obtained from the low surfactant concentration combined with a longer injection duration. Also, oil recovery can be affected by a different injection timing where the early injection can enhance a faster production rate, which in turn leads to the efficient reservoir management. Therefore, the appropriate selection of optimal injection timing is required to achieve the best outcome while considering operational parameters such as maximum injection pressure.

- The application of Fast Marching Method in unconventional reservoirs has been presented with the significant computational efficiency. Moreover, the improved workflow of computation of inter-partition transmissibility has been proposed and demonstrated, which leads to a further reduction in overall computation time for the field-scale application, while showing good agreement with the results from the FDSim. We recognize that the water-cut prediction using the FMM-based approach shows slight deviations compared to the FDSim. This may be improved by incorporating a recently introduced FMM-based simulation approach by Onishi et al. (2019) that is capable of capturing gravity and multiphase flow in hydraulic fracture planes. In all numerical examples presented in chapter 3, the FMM-based flow simulation is found to be in good approximation with commercial finite difference simulator (FDSim). Our results demonstrate that the inter-partition transmissibility method is able to capture the complex interactions between multiple wells with different production constraints.
- A hierarchical history matching process that accounts for not only reservoir model calibrations but also fluid model calibrations has been proposed and applied to the Dover 33 field. The uncertainty in the fluid model requires modifications in EOS model parameters. Including several updated EOS models in the history matching for primary depletion leads to successful history matching results for all objective functions. Other parameters that are associated with reservoir properties are calibrated throughout the additional production periods. Even though there are difficulties to meet all objective functions simultaneously including bottomhole

pressure of the injector during CO₂ injection only period, parameters are further narrowed down with acceptable matching results. However, the sharp increasing trend in bottomhole pressure is expected to match better with the modeling of pore volume reductions during CO₂ injections.

REFERENCES

- Adejare, O.O., Nasralla, R.A., Nasr-El-Din, H.A. (2012), A Procedure for Measuring Contact Angles When Surfactants Reduce the Interfacial Tension and Cause Oil Droplets to Spread. SPE 160876.
- Alexander, T, J. Baihly, and C. Boyer. 2011. "Shale Gas Revolution." *Oilfield Review* 23 (3): 40-55.
- Anderson, G.A.: "Simulation of Chemical Flood Enhanced Oil Recovery Processes Including the Effects of Reservoir Wettability." M.S thesis, The University of Texas at Austin, 2006.
- Anderson, W.G., (1987), Wettability Literature Survey-Part 6: The Effects of Wettability on Waterflooding. *Journal of Petroleum Technology*, Society of Petroleum Engineers, Vol. 39, Issue 12, SPE-16471-PA.
- Buckley, J.S., Bousseau, C., Li, Y., (1995), Wetting Alteration by Brine and Crude Oil: From Contact Angles to Cores. Society of Petroleum Engineers, SPE 30765.
- Cheraghian, G., (2015), Thermal Resistance and Application of Nanoclay on Polymer Flooding in Heavy Oil Recovery. *Petroleum Science and Technology*, 33:17-18, Pages: 1580-1586.
- Cheraghian, G., Nezhad, S.S.K., Kamari, M., Hemmati, M., Masihi, M., Bazgir, S., (2014), Adsorption Polymer on Reservoir Rock and Role of the Nanoparticles, Clay and SiO₂. *International Nano Letters*, 4:114.
- Cipolla, C. L., M. J. Williams, X. Weng et al. 2010a. "Hydraulic Fracture Monitoring to Reservoir Simulation: Maximizing Value." *SPE Annual Technical Conference and Exhibition*. Sep. 19-22, Florence, Italy. SPE-133877-MS. doi:<https://doi.org/10.2118/133877-MS>.
- Cipolla, C. L., E. P. Lolon, J. C. Erdle et al. 2010b. "Reservoir Modeling in Shale-Gas Reservoirs." *SPE Res. Eval & Eng.* 13 (4): 638-653. doi:<http://dx.doi.org/10.2118/125530-PA>.
- Cipolla, C. L., T. Fitzpatrick, M. J. Williams et al. 2011. "Seismic-to-Simulation for Unconventional Reservoir Development." *SPE Reservoir Characterisation and Simulation Conference and Exhibition*. Abu Dhabi, UAE. SPE-146876-MS. doi:<http://dx.doi.org/10.2118/146876-MS>

- Datta-Gupta, A., Pope, G.A., Sepehrnoori, K., and Thrasher, R.L, (1986), A Symmetric, Positive Definite Formulation of a Three-Dimensional Micellar/Polymer Simulator, SPE Reservoir Engineering 1, No. 6, Pages: 622-632.
- Datta-Gupta, A., J. Xie, Gupta N. et al. 2011. "Radius of Investigation and its Generalization to Unconventional Reservoirs." *Journal of Petroleum Technology* 63 (7): 52-55. doi:http://dx.doi.org/10.2118/0711-0052-JPT.
- Delshad, M., Freeze, G.A., Jackson, R.E., McKinney, D.C., Pope, G.A., Sepehrnoori, K., Sharma, M.M., and Speitel, Jr., G.E., (1994), Three-dimensional NAPL fate and transport model. Poster presented at RSKERL Ground Water Res. Semin., Oklahoma City, OK, Jun 1-3, 1994.
- Delshad, M., (1994), UTCHEM Technical Manual.
- Delshad, Mojdeh, G. A. Pope and K. Sepehrnoori. 1996. "A Compositional Simulator for Modeling Surfactant Enhanced Aquifer Remediation," *Journal of Contaminant Hydrology*, 23, 303-327.
- Delshad, M., Najafabadi, N.F, Anderson, G.A, Pope, G.A and Sepehrnoori, K., (2006), Modeling Wettability Alteration in Naturally Fractured Reservoirs. Society of Petroleum Engineers, SPE 100081.
- Diaz de Souza, O. C., A. J. Sharp, R. C. Martinez et al. 2012. "Integrated Unconventional Shale Gas Reservoir Modeling: A Worked Example From the Haynesville Shale, De Soto Parish, North Louisiana." *SPE Americas Unconventional Resources Conference*. Pittsburgh, Pennsylvania. 5-7 June. SPE-154692-MS. doi:http://dx.doi.org/10.2118/154692-MS.
- Dong, H., Hong, Y., Rui, W., Fan, D., (2006), The Effect of Wettability on Oil Recovery of Alkaline/Surfactant/Polymer Flooding. SPE 102564.
- Giraldo, J., Benjumea, P., Lopera, S., Cortes, F.B., Ruiz, M.A., (2013), Wettability Alteration of Sandstone Cores by Alumina-Based Nanofluids. *Energy & Fuels*, Vol. 27, Pages: 3659-3665.
- Hashemi, R., Nassar, N.N., Almao, P.P., (2013), Enhanced Heavy Oil Recovery by in Situ Prepared Ultradispersed Multimedia Nanoparticles: A Study of Hot Fluid Flooding for Athabasca Bitumen Recovery. *Energy & Fuels*, Vol. 27, Pages: 2194-2201.
- Hendraningrat, L., Li, S., Torsaeter, O., (2013), A Coreflood Investigation of Nanofluid Enhanced Oil Recovery in Low-Medium Permeability Berea Sandstone. SPE 164106.

- Huang, J. 2017. Analysis of Hydraulic Fracture Propagation and Well Performances using Geomechanical Models and Fast Marching. College Station: Ph.D Dissertation. Texas A&M University.
- Iino, A., Vyas, A., Huang, J. et al. 2017a. Efficient Modeling and History Matching of Shale Oil Reservoirs Using the Fast Marching Method: Field Application and Validation. SPE Western Regional Meeting. Apr. 24-27, Bakersfield, CA. SPE-185719-MS. doi:<https://doi.org/10.2118/185719-MS>.
- Iino, A., Vyas, A., Huang, J. et al. 2017b. Rapid Compositional Simulation and History Matching of Shale Oil Reservoirs Using the Fast Marching Method. SPE/AAPG/SEG Unconventional Resources Technology Conference. Jul. 24-26, Austin, TX. URTEC-2693139-MS. doi:<https://doi.org/10.15530/URTEC-2017-2693139>
- Iino, A. 2018. Efficient History Matching and Optimization of Unconventional Reservoirs Using the Fast Marching Method. College Station: Ph.D Dissertation. Texas A&M University.
- Jung, H. Y., Onishi, T., & Datta-Gupta, A. (2018). *Numerical Simulation of EOR from Wettability Alteration in Tight Oil Reservoir with Multiple Hydraulic Fractures*. Paper presented at the SPE Annual Technical Conference and Exhibition, Dallas, Texas, USA. <https://doi.org/10.2118/191409-MS>
- Karimi, A., Fakhroueian, Z., Bahramian, A., Khiabani, N.P., Darabad, J.B., Azin, R., Arya, S., (2012), Wettability Alteration in Carbonates using Zirconium Oxide Nanofluids: EOR Implications. Energy & Fuels, Vol. 26, Pages: 1028-1036.
- Kaveh, N.S., J.Berentsen, C.W., Rudolph, E.S.J., Wolf, K-H. A.A., Rossen, W.R., (2012), Wettability Determination by Equilibrium Contact Angle Measurements: Reservoir Rock-Connate Water System with Injection of CO₂. Society of Petroleum Engineers, SPE 154382.
- Li, S., Genys, M., Wang, K. and Torsaeter, O., (2015), Experimental Study of Wettability Alteration during Nanofluid Enhanced Oil Recovery Process and its Effect on Oil Recovery. Society of Petroleum Engineers, SPE 175610.
- Li, S. and Torsaeter, O., (2015), Experimental Investigation of the Influence of Nanoparticles Adsorption and Transport on Wettability Alteration for Oil Wet Berea Sandstone. Society of Petroleum Engineers, SPE 172539.
- Marongiu-Porcu, M., Lee, D., Shan, D., Morales, A., 2016. Advanced modeling of interwell-fracturing interference: an Eagle Ford shale-oil study. SPE Journal 21, 1,567-561,582.

- Masalmeh, S.K., (2002), The Effect of Wettability on Saturation Functions and Impact on Carbonate Reservoirs in the Middle East. Society of Petroleum Engineers, SPE 78515.
- Miranda, C.R., Lara, L.S.D., Tonetto, B.C., (2012), Stability and Mobility of Functionalized Silica Nanoparticles for Enhanced Oil Recovery Applications. SPE 157033.
- Morrow, N.R., (1990), Wettability and Its Effect on Oil Recovery. Journal of Petroleum Technology, Society of Petroleum Engineers, Vol. 42, Issue: 12, Pages: 1476-1484, SPE-21621-PA.
- Novlesky, A., A. Kumar and S. Merkle. 2011. "Shale Gas Modeling Workflow: From Microseismic to Simulation – A Horn River Case Study." *Canadian Unconventional Resources Conference*. Calgary, Alberta, Canada. 15-17 November. SPE-148710-MS. doi:<http://dx.doi.org/10.2118/148710-MS>.
- Ogolo, N. A., Olafuyi, O. A., Onyekonwu, M. O., (2012), Enhanced Oil Recovery Using Nanoparticles. SPE 160847.
- Park, H.-Y., Datta-Gupta, A., and King, M.J., (2015), Handling Conflicting Multiple Objectives Using Pareto-Based Evolutionary Algorithm During History Matching of Reservoir Performance. Journal of Petroleum Science and Engineering 125: 48-66.
- Penny, G., Zelenev, A., Lett, N., Paktinat, J. and O'Neil, B., (2012), Nanofluid System Improves Post Frac Oil and Gas Recovery in Hydrocarbon Rich Gas Reservoirs, Society of Petroleum Engineers, SPE 154308.
- Pope, G.A. and Nelson, R.C, (1978), A Chemical Flooding Compositional Simulator, SPEJ, Pages: 339-354.
- Ponnampati, R., Karazincir, O., Dao, E., Ng, R., Mohanty, K. K., Krishnamoorti, R., (2011), Polymer-Functionalized Nanoparticles for Improving Waterflood Sweep Efficiency: Characterization and Transport Properties. Industrial & Engineering Chemistry Research, Vol. 50, Pages: 13030-13036.
- Rao, D.N., (1997), Is There a Correlation Between Wettability From Corefloods and Contact Angles. SPE 32734.
- Salehi, M., Johnson, S.J., Liang, J-T., (2008), Mechanistic Study of Wettability Alteration Using Surfactants with Applications in Naturally Fractured Reservoirs. Langmuir, Vol. 24, Pages: 14099-14107.

- Sethian, J. A. 1996. "A Fast Marching Level Set Method for Monotonically Advancing Front." *Proc. Natl. Acad. Sci. USA* 93 (4): 1591-1595.
- Sethian, J. A. 1999. "Fast Marching Methods." *SIAM Rev* 41 (2): 199-235.
doi:<http://dx.doi.org/10.1137/S0036144598347059>.
- Sharma, G., Mohanty, K.K., (2013), Wettability Alteration in High-Temperature and High-Salinity Carbonate Reservoirs. Society of Petroleum Engineers, SPE-147306-MS.
- Sheshdeh, M.J., (2015), A Review Study of Wettability Alteration Methods with Regard to Nano-Materials Application. SPE- 173884-MS.
- Skauge, T., Hetland, S., Spildo, K., Skauge, A., (2010), Nano-Sized Particles for EOR. Society of Petroleum Engineers, SPE 129933.
- Teklu, T.W., Alameri, W., Kazemi, H., Graves, R.M., (2015), Contact Angle Measurements on Conventional and Unconventional Reservoir Cores. SPE-178568-MS/URTeC:2153996.
- Vasco, D. W., and A. Datta-Gupta. 2016. *Subsurface Fluid Flow and Imaging: Application for Hydrology, Reservoir Engineering and Geophysics*. Cambridge: Cambridge University Press.
- Wu, K., B. Wu, and W. Yu, 2018, Mechanism Analysis of Well Interference in Unconventional Reservoirs: Insights From Fracture-Geometry Simulation Between Two Horizontal Wells: SPE Production & Operations, v. 33, p. 12-20.
- Xie, J., C. Yang, N. Gupta et al. 2015. "Depth of Investigation and Depletion in Unconventional Reservoirs With Fast-Marching Methods." *SPE Journal* 20 (4): 831-841. doi:<http://dx.doi.org/10.2118/154532-PA>.
- Yaich, E., O. C. Diaz De Souza, R. A. Foster, and I. S. Abou-sayed, 2014, A Methodology to Quantify the Impact of Well Interference and Optimize Well Spacing in the Marcellus Shale, SPE/CSUR Unconventional Resources Conference – Canada, Calgary, Alberta, Canada, Society of Petroleum Engineers, p. 11.
- Yu, Wei, Hamid Reza Lashgari, Kan Wu, and Kamy Sephrnoori. "Co2 Injection for Enhanced Oil Recovery in Bakken Tight Oil Reservoirs." *Fuel* 159 (2015/11/01/ 2015): 354-63.

- Yuan, Y., Lee, T.R., (2013), Contact Angle and Wetting Properties. Surface Science Techniques, Vol.51 of the series Springer Series in Surface Sciences, Pages: 3-34.
- Zhang, T., Davidson, A., Bryant, S.L., Huh, C., (2010), Nanoparticle-Stabilized Emulsions for Applications in Enhanced Oil Recovery. SPE 129885.
- Zhang, Y., N. Bansal, Y. Fujita et al. 2016. "From Streamlines to Fast Marching: Rapid Simulation and Performance Assessment of Shale-Gas Reservoirs by Use of Diffusivity Time of Flight as a Spatial Coordinate." *SPE Journal* 21 (5): 1-16. doi:<http://dx.doi.org/10.2118/168997-PA>.
- Zuloaga-Molero, Pavel, Wei Yu, Yifei Xu, Kamy Sepehrnoori, and Baozhen Li. "Simulation Study of Co₂-Eor in Tight Oil Reservoirs with Complex Fracture Geometries." *Scientific Reports* 6, no. 1 (2016/09/15 2016): 33445.

APPENDIX A
COMPARISON OF EIKONAL SOLVER BETWEEN CELL-CENTER FMM AND
27PT-STENCIL FMM

Fast Marching Method (FMM), which is the method to solve the Eikonal equation, can be divided into several versions depending on the number of points where the Diffusive Time of Flight (DTOF) is calculated for each cell. More discretization while performing the FMM leads to more accurate $w(\tau)$ calculation, and a 1-D FMM-based simulation in turn shows the better match of simulation results compared to 3-D Finite Difference simulation. These improved and stable results with more discretization, however, have introduced expensive computational time that is not desirable for the FMM, which has been known for a rapid reservoir simulation. On the other hand, if less number of points is used in discretization, much greater speed-up factor can be achieved from a FMM-based simulation but, at the same time, the accuracy of simulation is more likely to be unstable for some cases. Two extreme versions of the FMM, based on the discretization scheme, are cell-center FMM and 27pt-stencil FMM. Cell-center FMM is only to calculate DTOF on the center of each grid cell whereas 27pt-stencil FMM accounts for unknowns including not only center but also vertex and edges of the cell.

Li (2018) has investigated pros and cons of various designs for the Eikonal solvers depending on the selection of discretization. In this section, a comparison of two different Eikonal solvers (cell-center and 27pt-stencil) is conducted for the case with complex hydraulic fractures where grid cells that represent hydraulic fractures are occasionally

disconnected. Iino (2018) has studied that there are some specific cases (having high contrast in permeability between fractures and formation) where the accuracy and stability of simulation results are significantly affected by the choice of discretization schemes. In those cases, 27pt-stencil FMM performs better than cell-center FMM.

In general, it has been noticed that 27pt-stencil FMM provides better performance despite long CPU time because of the difference in how to accumulate pore volume with respect to Diffusive Time of Flight (Iino 2018). In other words, 27pt-stencil FMM results in a smooth relationship between pore volume and Diffusive Time of Flight even when propagating from the fracture to the formation. That is because Diffusive Time of Flight is interpolated using maximum and minimum values of DTOF for every cell.

However, in an increased demand to better understand unconventional reservoirs, the geometry of hydraulic fractures in a reservoir simulation has been complicated recently while majority of the former hydraulic fractures are represented as a planar type of structure with uniform properties, such as constant fracture conductivity and water saturation. Therefore, in this section, we investigate several synthetic cases from 2-D to 3-D examples to compare the feasibility of two Eikonal solvers.

A.1 Validation Using 2D Synthetic Cases

A.1.1 Case Setting

We set up the 2-D reservoir models as summarized in Table A.. In order to see the effect of discretization schemes, simple examples have been set up, which are 2-D, single phase synthetic cases (Figure A.1). These single-porosity models are homogeneous

reservoirs with uniform permeability of 100 mD. The size of reservoir is 1010'×1010'×100' and the number of grid cells is 101×101×1 (10,201 cells). There is one vertical well with one zigzag type of hydraulic fractures that have 100 md·ft of fracture conductivity in this model. Depending on the connectivity of two sides (west and east) of hydraulic fractures and on the location of the wells, four different cases are prepared as summarized in Table A.1.

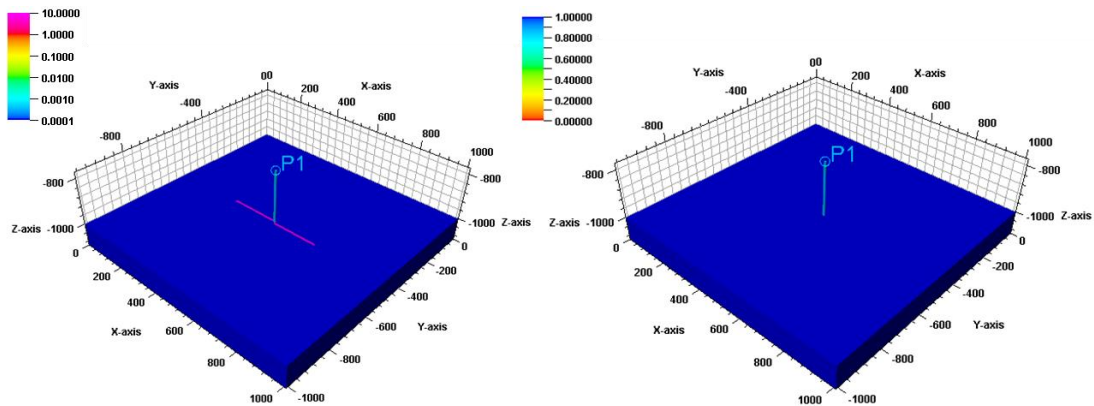


Figure A.1 Permeability distribution (Left) and initial water saturation distribution (Right) for 2D synthetic case

Table A.1 2-D synthetic cases setup

	Location of well		Connection of zigzag HF	
	At the center	Away from the center	Connected	Disconnected
Case 1-1	○		○	
Case 1-2	○			○
Case 2-1		○	○	
Case 2-2		○		○

The wells are right in the center of the reservoir and are located in the edge of one side of hydraulic fractures for case 1-1 and case 1-2 (Figure A.2). On the other hand, the location of a well for case 2-1 and case 2-2 is shifted away from the center where the well is in the middle of one side of hydraulic fractures (Figure A.3). Also, for the respective well location, cases are divided into two sets depending on whether two sides of hydraulic fractures are disconnected or connected with one cell in the middle. Here, we are trying to represent the complex geometry with disconnected features of hydraulic fractures. This is because it can take place when to convert the complex hydraulic fractures generated in the unstructured grid to the one in the structured grid for reservoir simulations.

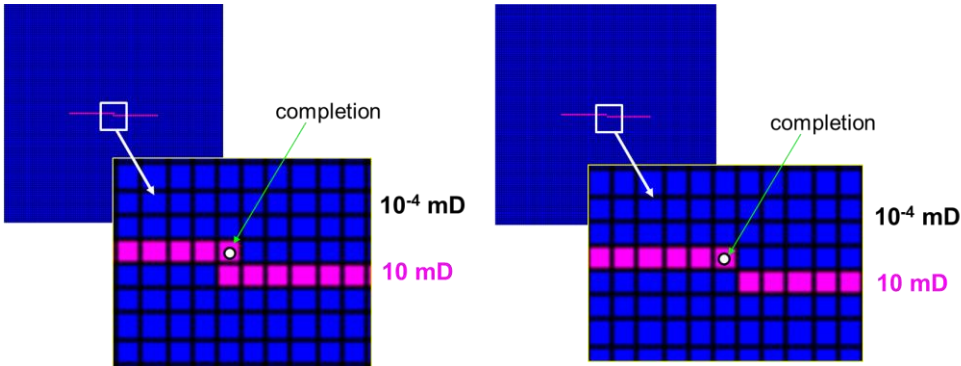


Figure A.2 Description of Case 1-1 (Left) and Case 1-2 (Right)

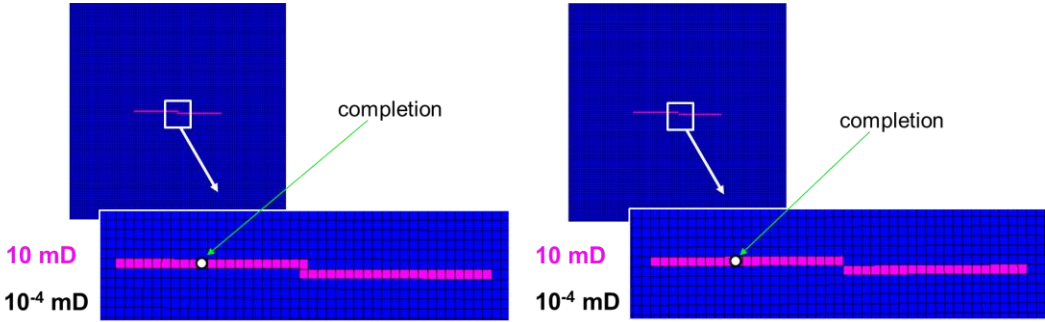


Figure A.3 Description of Case 2-1 (Left) and Case 2-2 (Right)

A.1.2 Comparison of Diffusive Time of Flight and Simulation Results

In order to study the performance of an individual Eikonal solver on complex hydraulic fractures, simulation results of the FMM-based simulation with both cell-center FMM and 27pt-stencil FMM have been compared with those of Finite Difference simulator (Eclipse) for each case (Figure A.4 and Figure A.5). All models are simulated with constant water production rate so bottomhole pressure has been presented. As shown in both figures, the cases having connected zigzag hydraulic fractures, which corresponds to Case 1-1 and Case 2-1, show a fairly good agreement with one another. However, Case 1-2 and Case 2-2 that have disconnected fractures show that cell-center FMM is better matched with Eclipse than 27pt-stencil FMM regardless of the location of the well. Especially, both FMM-based simulation results for Case 1-2 are relatively less accurate compared to Case 2-2. This can be explained by the boundary effect due to the contrast of permeability between hydraulic fractures and formation. Since the cell where the well is located in is contacting the formation, which has very low permeability, the formation itself can function as boundary. In this case, simulation results can be improved by considering a reflected DTOF map and solving additional pressure drops on that reflection DTOF map (Huang 2017).

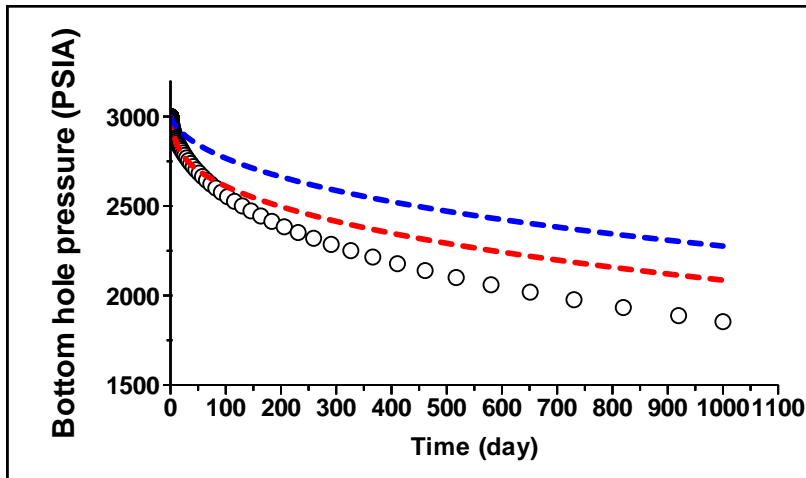
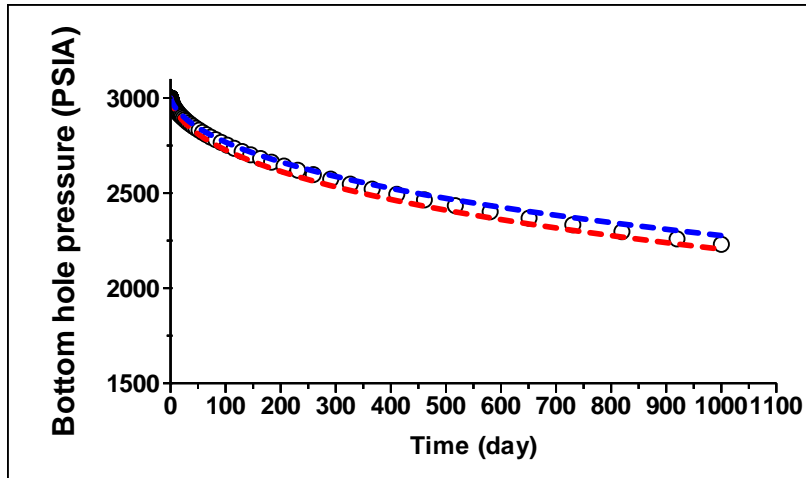


Figure A.4 Comparison of bottom hole pressure for Case 1-1 (top) and Case 1-2 (bottom): symbol: Eclipse, red line: cell-center FMM and blue line: 27pt-stencil FMM

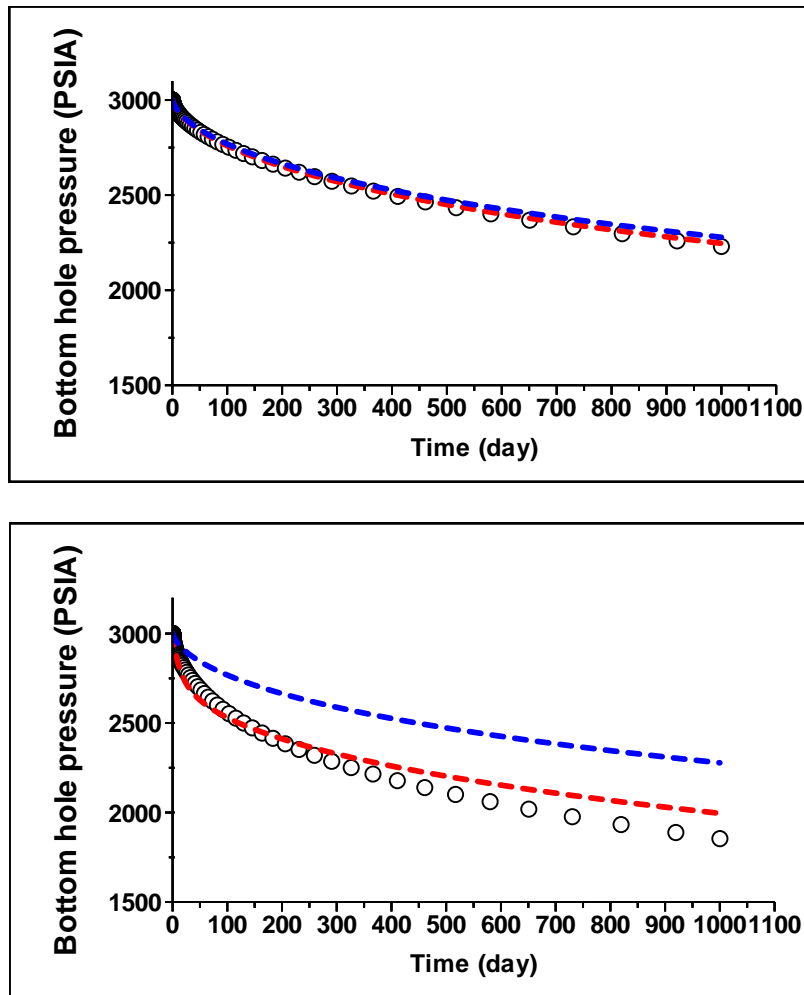


Figure A.5 Comparison of bottom hole pressure for Case 2-1 (top) and Case 2-2 (bottom): symbol: Eclipse, red line: cell-center FMM and blue line: 27pt-stencil FMM

In addition to bottomhole pressure plots, the Diffusive Time of Flight has been examined to see what could cause the difference between cell-center FMM and 27pt-stencil FMM for the disconnected fracture geometry along with the pressure distribution. While both DTOF maps from cell-center FMM and 27pt-stencil FMM are consistent with each other for the Case 1-1 (Figure A.6), there is a large discrepancy between two for the

Case 1-2 (Figure A.7), where the DTOF contours of cell-center FMM are aligned well with pressure distribution from Finite Difference simulation after 5 month.

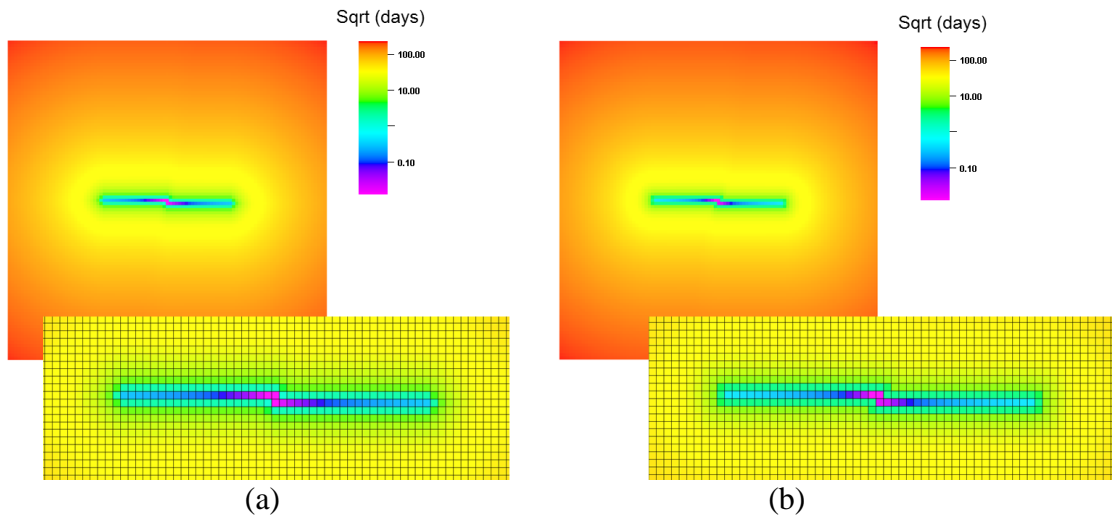


Figure A.6 Diffusive Time of Flight maps for Case 1-1 (a) cell-center FMM (b) 27pt-stencil FMM

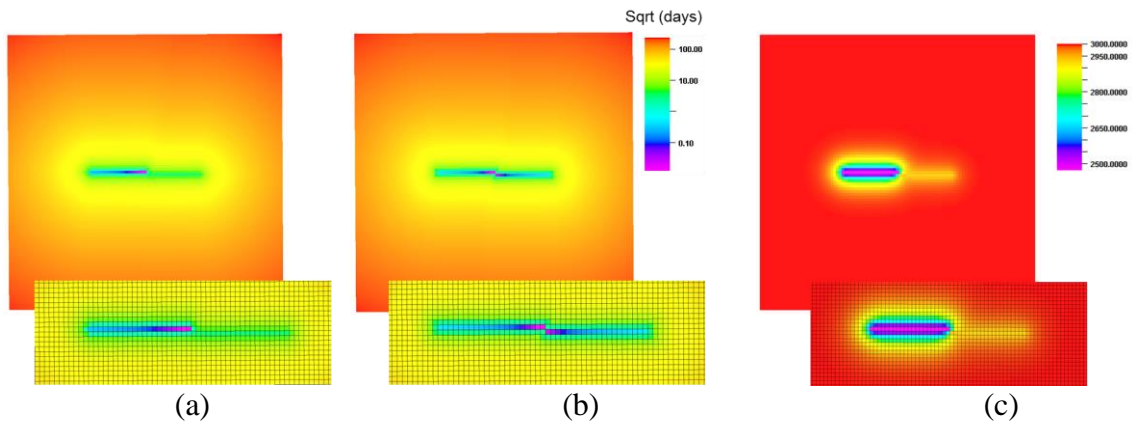


Figure A.7 Diffusive Time of Flight maps for Case 1-2 (a) cell-center FMM (b) 27pt-stencil FMM (c) pressure distribution after 5 months

The reason for the discrepancy for Case 1-2 is ironically due to the accuracy of 27pt-stencil FMM with more discretization when obtaining Diffusive Time of Flight. Even

though the connection through the vertex between two cells is not defined in Finite Difference simulation, 27pt-stencil scheme starts to accumulate pore volume of east side of the hydraulic fracture immediately since it calculates DTOF at the vertex which is connected to an east-south cell with high permeability. Then, 27pt-stencil FMM considers that point as a shortest path. Case 2-1 and Case 2-2, which show a good agreement of pressure profile than the first two cases, present analogous tendency (Figure A.8 and Figure A.9) as we have already seen in the previous cases. Therefore, the location of well affects the accuracy of the simulation results of the FMM-based simulation, such that it helps to prevent from the effect of reflection at early time for these specific cases.

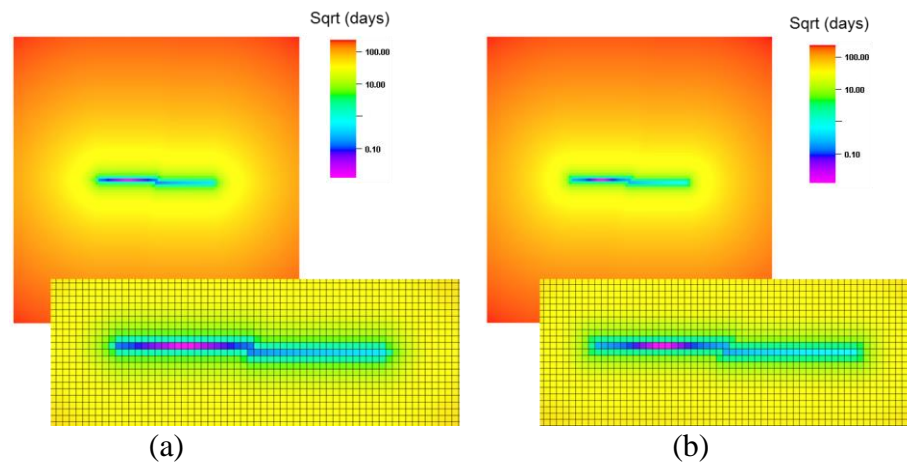


Figure A.8 Diffusive Time of Flight maps for Case 2-1 (a) cell-center FMM (b) 27pt-stencil FMM

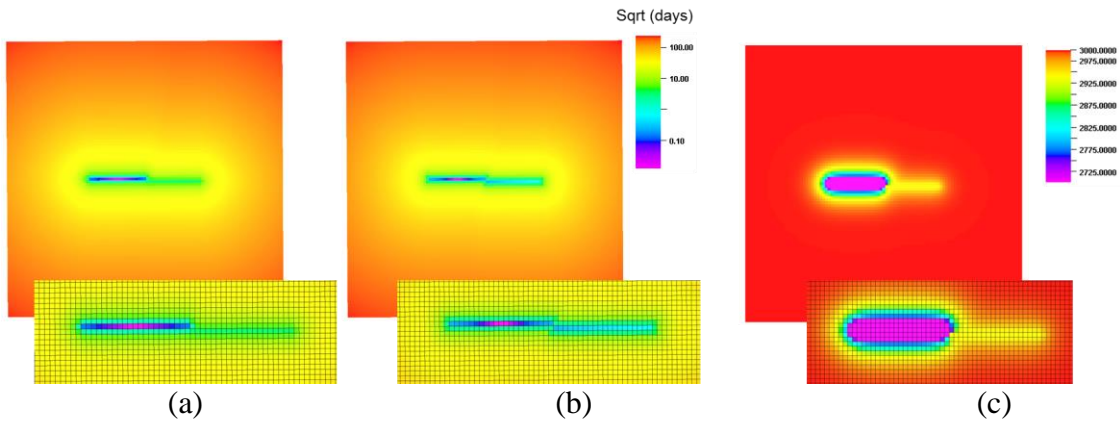
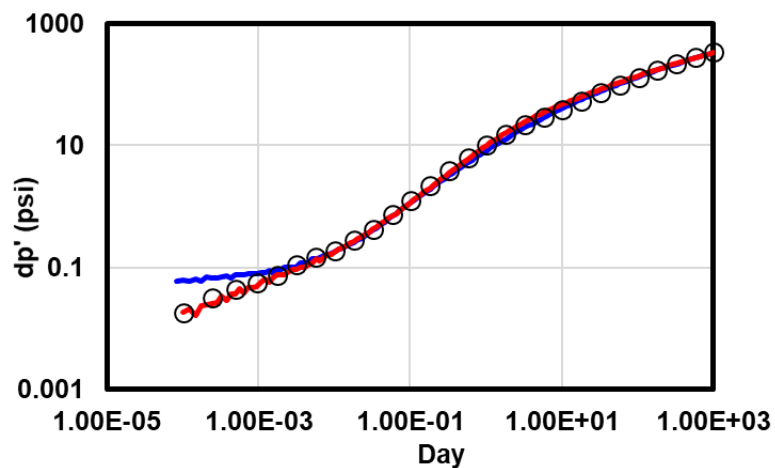


Figure A.9 Diffusive Time of Flight maps for Case 2-2 (a) cell-center FMM (b) 27pt-stencil FMM (c) pressure distribution after 5 months

Other than bottomhole pressure profile as well as Diffusive Time of Flight maps, log-log diagnostic plots are generated to see if a pressure derivative from the FMM-based simulation follows the one from FD simulations. As shown in Figure A.10 and Figure A.11, overall trend of both cell-center FMM and 27pt-stencil FMM shows a reasonable match with Eclipse for Case 1-1 and Case 2-1. On the other hand, it has been observed that the pressure derivative of 27pt-stencil FMM is quite deviated from the one of Eclipse, which can explain the poor match for bottomhole pressure.



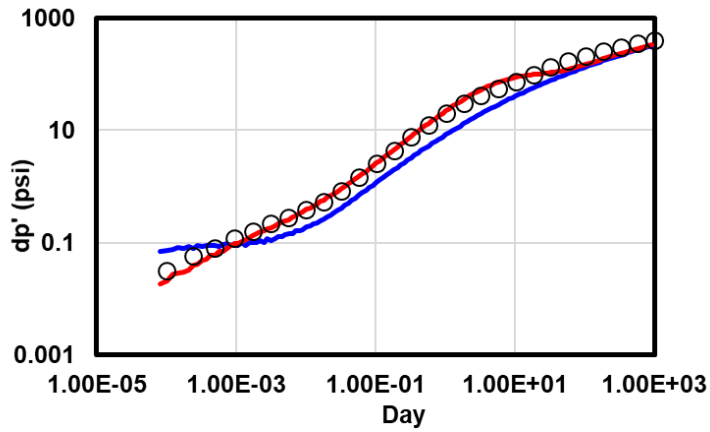


Figure A.10 Log-log diagnostic plot Case 1-1 (top) Case 1-2 (bottom): symbol: Eclipse, red line: cell-center FMM and blue line: 27pt-stencil FMM

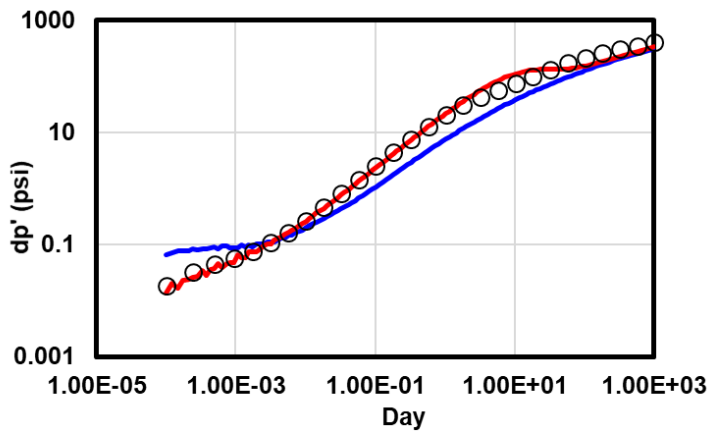
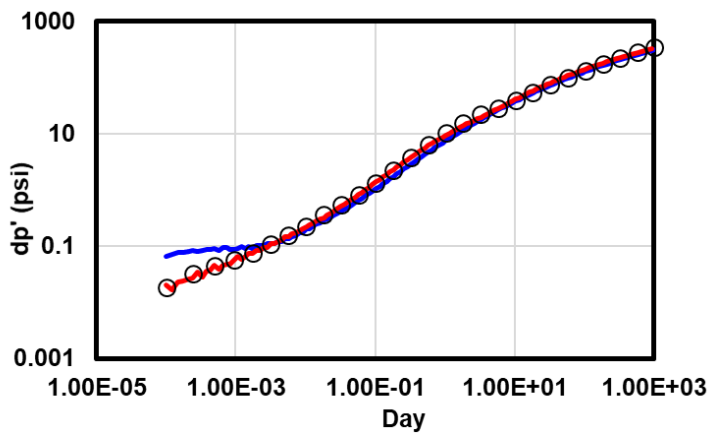


Figure A.11 Log-log diagnostic plot Case 2-1 (top) Case 2-2 (bottom): symbol: Eclipse, red line: cell-center FMM and blue line: 27pt-stencil FMM

A.1.3 Representation of Flow Through Vertex in Finite Difference Simulation

One of the important observations from the previous results is that 27pt-stencil FMM-based simulation behaves differently because the pore volume of the east side hydraulic fracture is accumulated through the vertex for the disconnected fracture geometry. This results in the overestimate of $w(\tau)$ function, which in turn leads to high bottomhole pressure, compared to Finite Difference simulation. To emulate and confirm the flow pattern that is occurring in 27pt-stencil FMM, two additional cases are prepared where the two side of zigzag fractures are connected but with a smaller and refined grid cell as shown in Figure A.12. By adjusting the size of the cells around a connection between two sides of fractures and by having fractures connected with 0.1ft of grid cell, similar flow patterns can be achieved in Finite Difference simulations. Table A.2 summarizes two new cases combined with the previous cases.

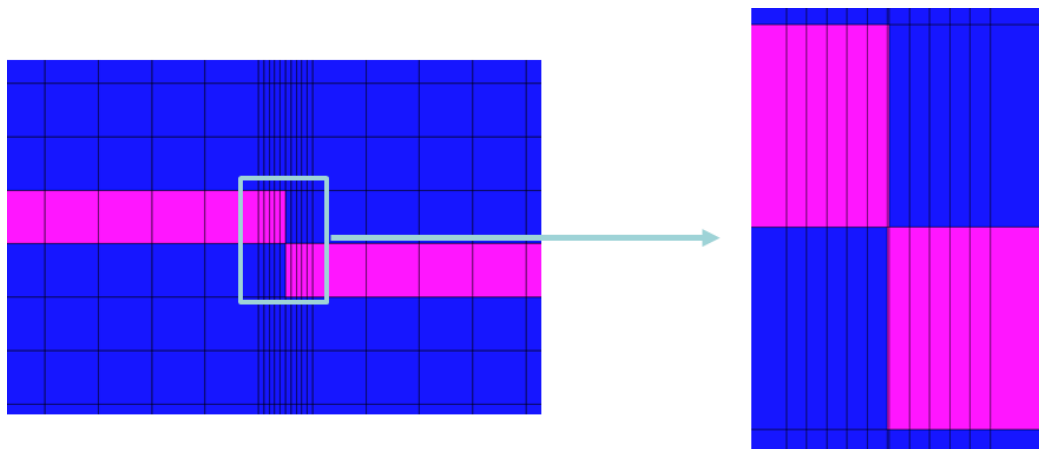


Figure A.12 Representation of connection between zigzag hydraulic fractures through refined grid cell

Table A.2 Additional 2-D cases setup

	Location of well		Connection of zigzag HF	
	At the center	Away from the center	Connected	Disconnected
Case 1-1	○		○	
Case 1-2	○			○
Case 2-1		○	○	
Case 2-2		○		○
Case 3	○		○	
Case 4		○	○	

In Figure A.13, the bottomhole pressure of Case 3 (FD simulation) has been included in the comparison of all simulation results generated from the Case 1-2. There are some level of mismatch between 27pt-stencil FMM (Case 1-2) and Finite Difference simulation (Case 3), however, the quality of match has been improved. It can be also noticed that DTOF map of 27pt-stencil FMM is now more consistent with pressure distribution of Case 3 (Figure A.14), which indicates that once the flow between west and east fractures can be considered properly with the grid refinement, the performance of 27pt-stencil FMM is favorable as expected.

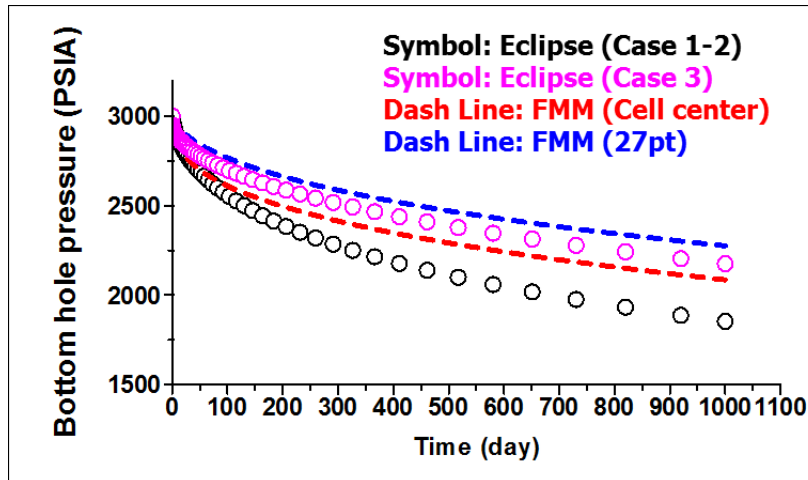


Figure A.13 Comparison of bottomhole pressure between Case 1-2 and Case 3

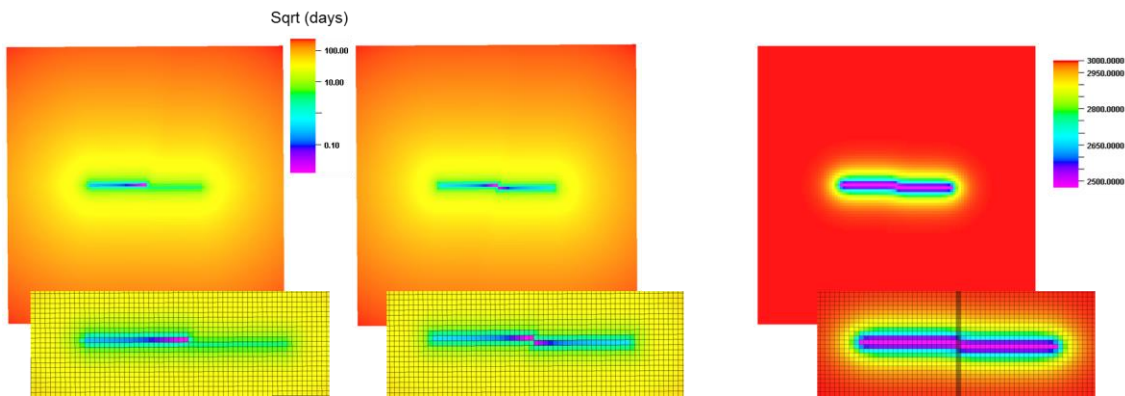


Figure A.14 Diffusive Time of Flight maps for Case 1-2: (a) cell-center FMM (b) 27pt-stencil FMM, (c) pressure distribution for Case 3

If the location of the well is moved away from the center, which is more likely to avoid the effect of reflection at early time, a bottomhole pressure profile from Case 4 (FD simulation) becomes closer to the one from 27pt-stencil FMM-based simulation (Figure A.15). Also, overall shape of pressure distribution of Case 4 is better matched with 27pt-stencil FMM DTOF maps (Figure A.16).

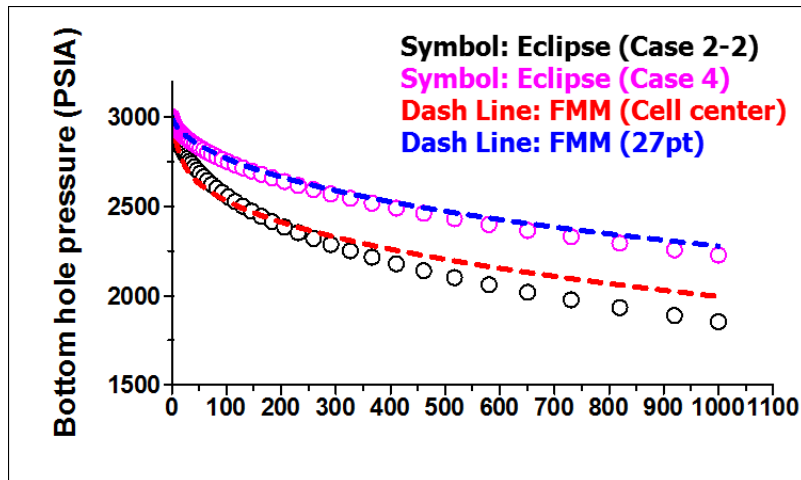


Figure A.15 Comparison of bottomhole pressure between Case 2-2 and Case 4

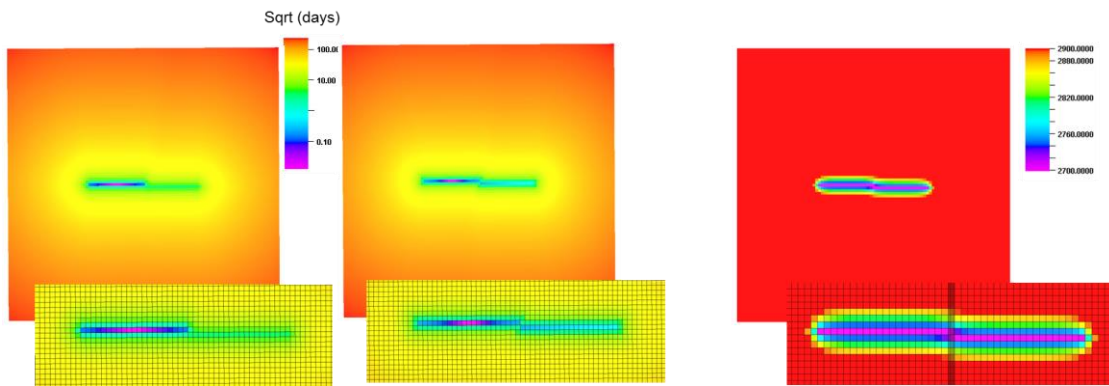


Figure A.16 Diffusive Time of Flight maps for Case 2-2: (a) cell-center FMM (b) 27pt-stencil FMM, (c) pressure distribution for Case 4

A.2 3D Synthetic Example

A.2.1 Case Setting

We set up a 3-D reservoir model with a zigzag type of hydraulic fractures as described in Figure A.17 to see the effect of different Eikonal solvers between cell-center FMM and 27pt-stencil FMM. Similar to the previous 2-D synthetic examples, this is a homogeneous and single-phase model where the matrix permeability is 100nd and initial

water saturation is 1.0. The reservoir domain of 1,100'×1,100'×100' was regularly divided into 101×101×5 Cartesian cells. In addition, there is a vertical well in the middle of a zigzag hydraulic fracture.

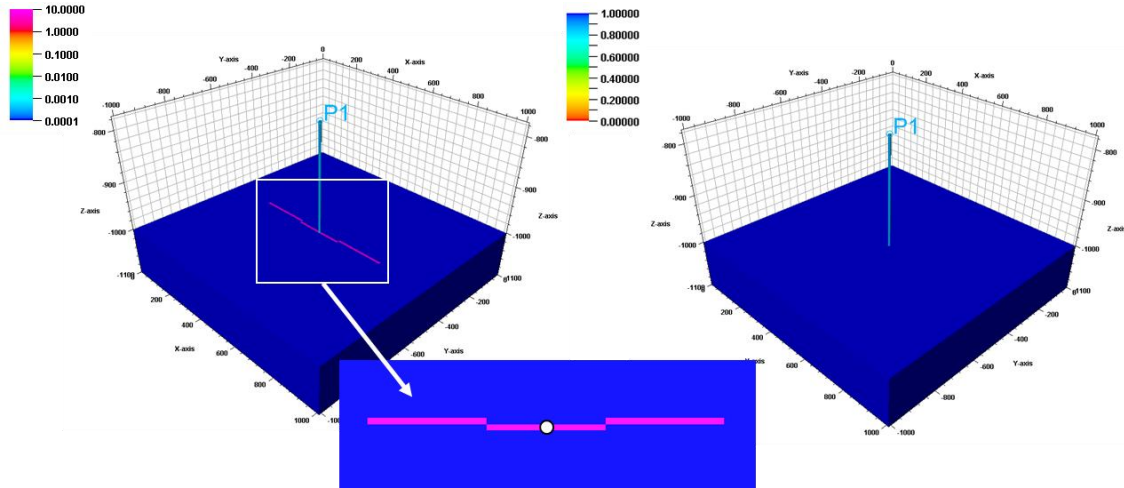


Figure A.17 Permeability distribution (Left) and initial water saturation distribution (Right) for 3D synthetic case

A.2.2 Simulation Results

As we have seen in the Section A.1, pressure responses from the 3-D Finite Difference simulation show a reasonable agreement with the one from cell-center FMM (Figure A.18). Bottomhole pressure from 27pt-stencil FMM is significantly higher than the other two simulation results, which implies that 1-D transmissibility from 27pt-stencil is greater than the one from cell-center FMM because it accumulates pore volume of both sides of hydraulic fractures through the edge of grid blocks. It is also observed that the Diffusive Tight of Flight (DTOF) map from cell-center FMM is better matched with the pressure distribution from a 3-D Finite Difference simulation as shown in Figure A.19. It

has proved that pressure disturbance is not immediately developed into both sides of hydraulic fractures whereas it is the case for 27pt-stencil FMM. A comparison of DTOF in a 3-D view in Figure A.20 also demonstrates that pressure fronts are already propagating into the both sides of hydraulic fractures in 27pt-stencil FMM whereas DTOF remains the middle hydraulic fractures due to the low permeability with the specified cutoff. Therefore, it can be concluded that 27pt-stencil FMM is able to cause the mismatch with 3-D Finite Difference simulation for cases with complex hydraulic fractures.

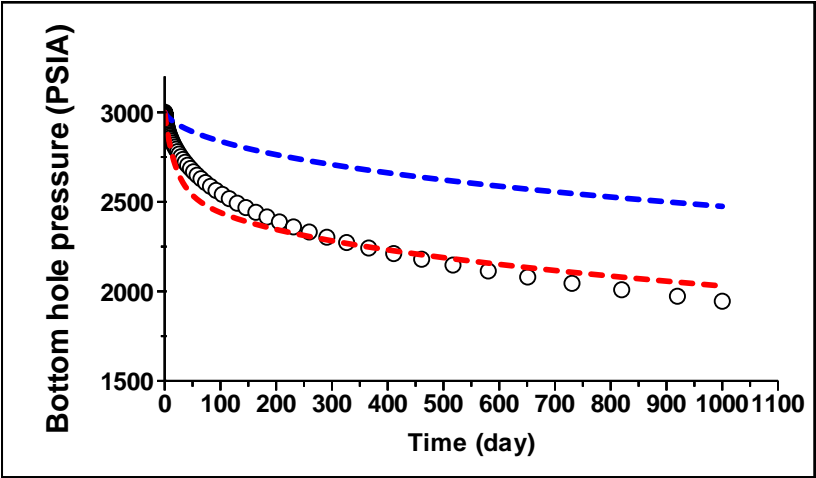


Figure A.18 Comparison of bottom hole pressure for 3D case: symbol: Eclipse, red line: cell-center FMM and blue line: 27pt-stencil FMM

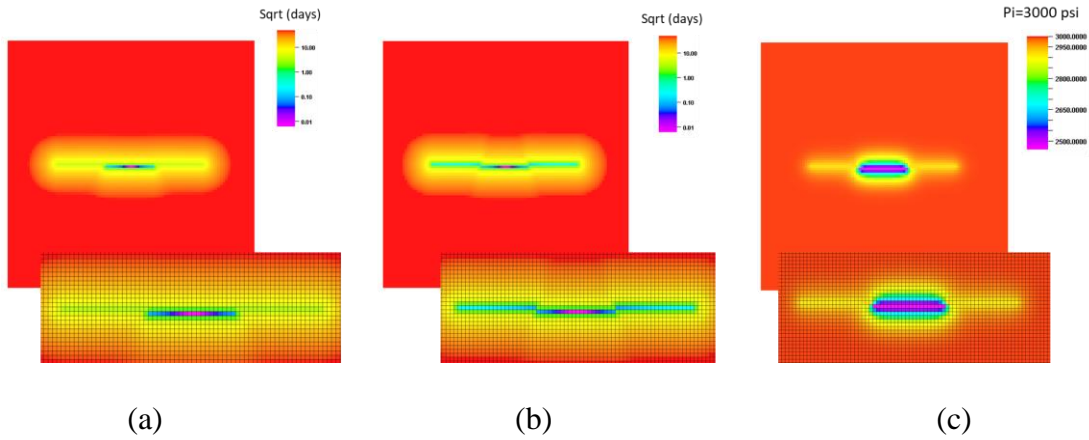


Figure A.19 Diffusive Time of Flight maps in 3rd layer for 3D case (a) cell-center FMM (b) 27pt-stencil FMM (c) pressure distribution after 5 months

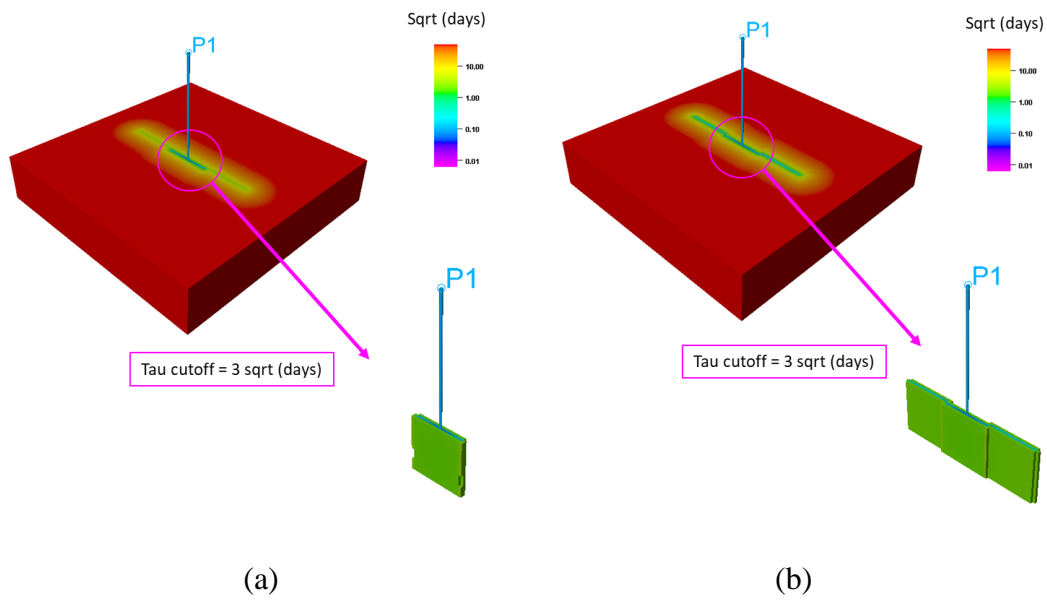


Figure A.20 Diffusive Time of Flight with cutoff (a) cell-center FMM (b) 27pt-stencil FMM

A.3 Field Application

A.3.1 Case Setting

A simulation model in this field application is provided by an operator, which is a dual-porosity and single permeability compositional model with 13 components. As shown in Figure A.21, the geometry of hydraulic fractures is extremely complicated, which has high permeability compared to the matrix domain. Permeability in matrix domain is in the micro-darcy range with the mean of $3.5 \mu\text{d}$, which is homogeneous horizontally but heterogeneous vertically. Reservoir dimension is $5,400' \times 6,169' \times 443'$ consisting of $196 \times 224 \times 90$ grid blocks with one horizontal well.

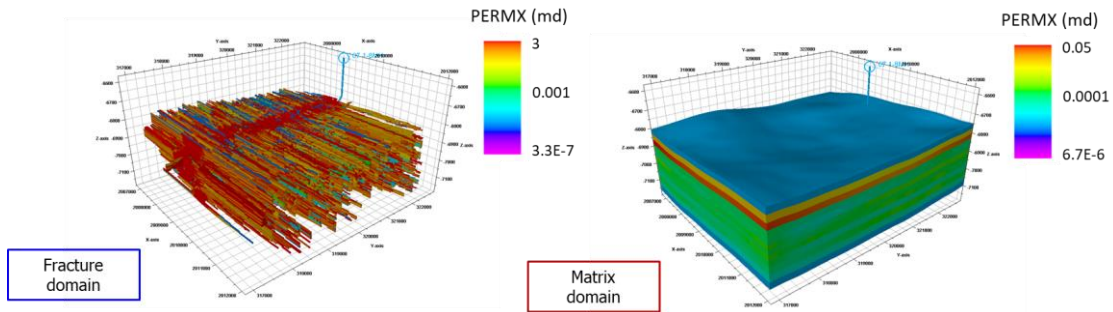


Figure A.21 Permeability distribution in fracture domain (left) in matrix domain (Right)

A.3.2 Simulation Results

In the dual-porosity system where the fracture domain has a higher permeability and consequently plays an important role in fluid flow, the Eikonal equation is solved in the fracture domain only (Iino 2017). Therefore, cell-center FMM and 27pt-stencil FMM are applied and used to calculate DTOF in the fracture domain in this field application

respectively. In Figure A.22, DTOF maps are presented and compared with each other when it comes to a certain τ cutoff. Within the specified τ cutoff, there is a distinct difference, which indicates that DTOF from 27pt-stencil FMM is propagating further than the one from cell-center FMM. As a result, oil production rate and bottomhole pressure from 1-D simulation using 27pt-stencil are higher than the ones from Finite Difference simulation whereas simulation responses from cell-center FMM show a good agreement. It implies that the transmissibility in 1-D simulation using 27pt-stencil is higher than what it is supposed to be due to an incorrect DTOF distribution as shown in Figure A.23.

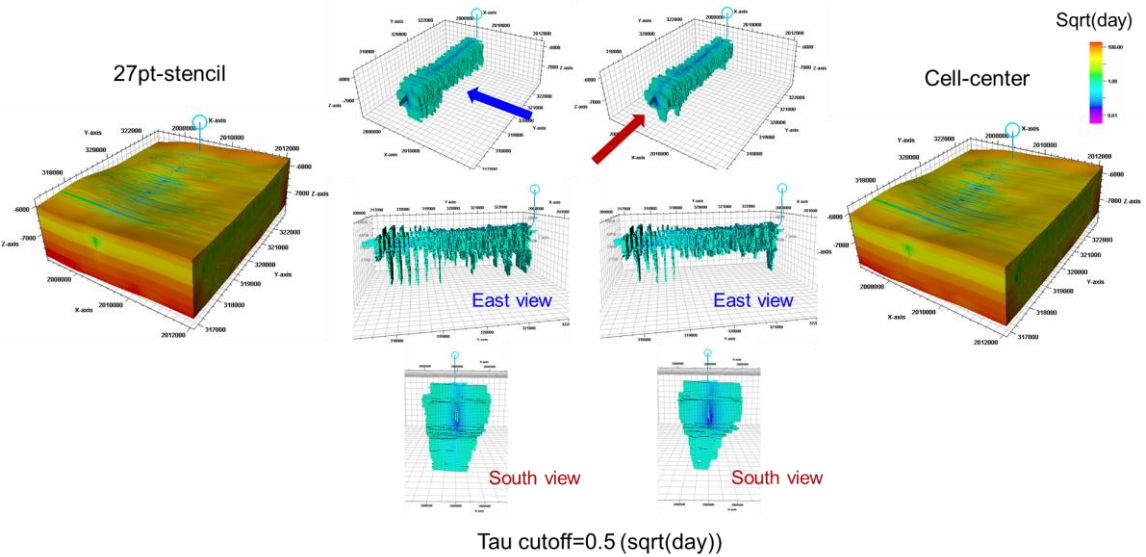
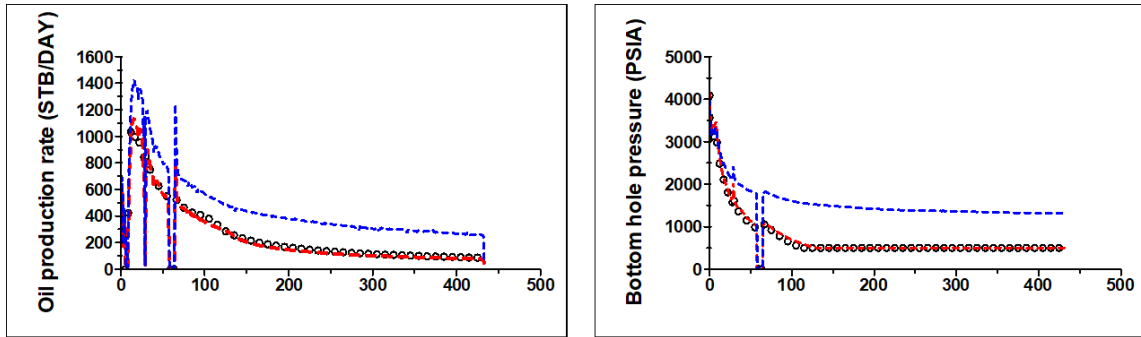


Figure A.22 Comparison of Diffusive Time of Flight: 27pt-stencil (left) and cell-center (right)



(a) Oil production rate

(b) Bottomhole Pressure

Figure A.23 Comparison of simulated response: symbol: Eclipse, red line: cell-center FMM and blue line: 27pt-stencil FMM

A.4 Summary

In this appendix, we discussed the validity to use the cell-center FMM for special cases that have complex hydraulic fracture geometries:

- The accuracy of the Eikonal solvers is dependent upon the geometry of hydraulic fractures
- For the case with connected hydraulic fractures, both cell-center and 27pt-stencil FMM perform well and show comparable simulation results with Finite Difference simulation
- For the case with disconnected hydraulic fractures, 27pt-stencil FMM can capture the flow through the vertex so that it shows different simulation responses from those of Finite Difference simulation
- With an appropriate grid refinement around the disconnected area, the flow through vertex in 27pt-stencil FMM can be captured properly in Finite Difference

simulation by allowing west and east fractures to be connected with a smaller as well as refined grid cell.

- The field application with the complicated geometry of hydraulic fractures demonstrated that the cell-center FMM is more appropriate because DTOF in the 27pt-stencil FMM seems to be propagating rapidly.

APPENDIX B

GLOBAL (HISTORY MATCHING TOOL USING GENETIC ALGORITHM)

MANUAL

GLOBAL is a software for the history matching based on Genetic Algorithm (GA). It currently has a function of a single GA, a Multi-objective GA and GCT (Grid-Connectivity-based Transform).

B.1 Source Code and Compiling by Visual Studio

B.1.1 Source Code

This software is compiled and installed from source codes which is in a format of C++. Once the source codes are compiled, it will generate an executable file, called “GLOBAL.exe”. Table B.1 has the list of source codes and the corresponding description respectively.

Table B.8 Source codes and descriptions

Source filenames	Descriptions
cmg.cpp cmg.h	simulator CMG(IMEX/GEM)
conf.h	build configuration, smart pointer, test build, external library, linear solver
counted_ptr.h	counted smart pointer, compatible with std::vector<T>, similar to boost::shared_ptr
dv_proxy.h	matlab fast marching DV/SRV calculation interface
ecl.cpp ecl.h	simulator ECL(ECLIPSE/E300)
eval.h	utility function for calculating expression value in template
ga.cpp ga.h	GA / MOGA inversion

gaio.h	ASCII/Binary I/O class with unified form
gauss.cpp gauss.h	direct linear solver with LU decomposition for kriging
inverse.h	class template for scanning .INP and overall steps of inversion
krige.cpp krige.h	response surface by kriging interpolation
lhdesign.cpp lhdesign.h	Latin Hypercube sampling, a space filling design
libdvproxy.h	header file for dvproxy.dll/dvproxy.so built from matlab
main.cpp	main entry of program
Makefile	makefile, can be customized for general purpose
owned_ptr.h	owned smart pointer, esp. for file streams, similar to boost::scoped_ptr
parameter.h	parameter class, high/low bounds, CDF
platform.cpp platform.h	platform check/output for binary
quadratic.cpp quadratic.h	response surface by quadratic polynomial regression, not recommended
rand_design.cpp rand_design.h	random experimental design
reservoir.h	main class template for data integration
rsf.cpp rsf.h	base response surface class, inherited by kriging and quadratic
stdafx.cpp stdafx.h	common functions
test.h	testing functions for developing purpose
well.cpp well.h	well class, consists of well rates, pressure, completions

B.1.2 Compiling by Visual Studio

Open GLOBAL.sln from Visual Studio 2015, select win32 or x64 (if x64 compilers installed), Build→Build Solution.

An executable called **GLOBAL.exe** will be generated for those folders:

GLOBAL\x64\Release (64 bit release build, for application purpose)

GLOBAL\x64\Debug (64 bit debug build, for debugging purpose)

GLOBAL\Release (32 bit release build)

GLOBAL\Debug (32 bit debug build)

B.2 Preparation of Input Files

B.2.1 Overview of Input Files and Their Structures

In order to run GLOBAL, mainly four types of input files need to be prepared, which are 1) *.INP 2) *.TMPL 3) *.DISTR 4) *.DATA (simulation deck) as shown in Figure B.1. *.INP file is a main input file for GLOBAL to control the whole workflow with keywords. *.DISTR file has the information of all variables to be changed during history matching, such as base, minimum and maximum values and each variable in the *.TMPL will be replaced with an actual value. More details can be found in the following sections for each input file.

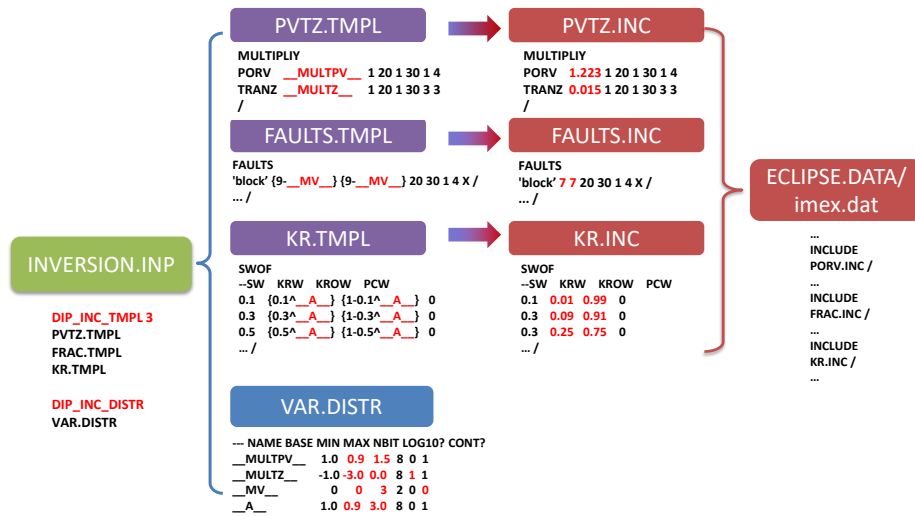


Figure B.1 Overview of global update

B.2.2 Inversion Input File (*.INP)

Keywords in the *.INP file is shown in Table B.2 with the description.

Table B.2 Keywords in inversion input file

Keywords and formats	Descriptions
<p>DIP_STUDYNAME ECLRFT</p> <p>DIP_SIM_CMD \$e300 -ver 2019.1</p>	<p><u>1. Simulator Settings</u></p> <p>Prefix of a simulation input deck</p> <p>Overwrite default simulator commands: \$eclipse/@eclipse for ECLIPSE, or any executable (*.exe) of simulator can be used</p>
<p>DIP_INC_TMPL 3 PVTZ.TMPL FAULTS.TMPL KR.TMPL</p> <p>DIP_INC_DISTR VAR.DISTR</p> <p>DIP_SENS_RUN</p>	<p><u>2. Variable Settings</u></p> <p>Include templates for variable substitutions, 3 means number of templates, the name of variables should be consistent with .DISTR file</p> <p>Distributions of variables included in all .TMPL files. Should contain exactly same list of vars in form of __*__</p> <p>If this option turned on, Tornado sensitivity analysis will be generated to a *.SENS file, all GA/proxy settings will be skipped. Starting from base column, perturbing each variable to its lower and high bound.</p>
<p>DIP_OBJECTIVE LPT MDT SBHP SRV</p> <p>DIP_SMRY_OBS 1 SCHEDULE</p> <p>DIP_MDT_OBS 1 obs_mdt_office.txt</p> <p>DIP_KEY_WELL 2 P1 P2</p>	<p><u>3. Objective Settings</u></p> <p>Build-in objective, each keyword will corresponds to following observed data. Keywords allowed includes: LPT/OPT/WPT/GPT: field total liq/oil/water/gas prod. MDT: well MDT pressures vs. TVD FBHP: well flowing BHP SBHP: well shut-in BHP FPR: Field average reservoir pressure WOPR/WWPR/WGPR: well oil/water/gas prod.</p> <p>Required if LPT/OPT/WPT/GPT/FBHP/SBHP included OBJECTIVE, observed data from WCONHIST or ECL Office format .FHF. SCHEDULE means obs from WCONHIST</p> <p>Required if MDT included in OBJECTIVE, observed data in *_TRUE.RFT (reference run) or ECL Office format</p> <p>Wells included in OBJECTIVE, others skipped. 2 means number of wells, followed by list of well names</p>

<p>DIP_KEY_TSTEP 5 1-2 3 4-5</p> <p>DIP_KEY_TIME 4 0 100 300 400</p>	<p>TSTEPS included in OBJECTIVE, others skipped. 5 is number of TSTEPS, followed by TSTEP id ranges, can be used for integrating only selected data or prediction. Not compatible with UNIFOUT</p> <p>Time period included in OBJECTIVE, others skipped. 4 means number of time bounds, 0-100 days, 300-400 days</p>
<p>DIP_PROXY_NED 20</p> <p>DIP_PROXY_TOL 0.2</p> <p>DIP_PROXY_SCAN</p>	<p><u>4. Proxy Settings (Applicable only when GA is used)</u></p> <p>Number of experiments designs for initial response surface proxy. Set to large for small problems.</p> <p>Tolerance allowed for response surface proxy check</p> <p>If this keyword exists, previous proxy will be scanned from existed .BIN file, otherwise existed .BIN/OUT/.OBJ will be removed/replaced, very useful for field case with fixed variable distribution setting, restart from previous proxy (.BIN file)</p>
<p>DIP_GA_CROSSOVER 0.70 2</p> <p>DIP_GA_MUTATE 0.05 2</p> <p>DIP_GA_REPLACE 0.70</p> <p>DIP_GA_POPSIZE 500</p> <p>DIP_GA_NGEN 5000</p>	<p><u>5. GA Settings (Applicable for both GA and MOGA)</u></p> <p>Default 0.50 0, uniform crossover with p=0.50. 0.70 2 means multi-point crossover with p=0.70 for each segment, 2 segments</p> <p>Default 0.001 0, uniform mutation with p=0.001. 0.05 2 means multi-point mutation with p=0.05 for each segment, 2 bits. p should be higher for multipoint mutation than that for uniform for same level of mutation by different schemes</p> <p>Elitism algorithm default 1.00. 0.70 means 70% of population will be replace, while top 30% good samples of generation kept to next generation, very useful for large-scale inverse problem</p> <p>Population size, must be even number, long list of variable should go with larger pop size</p> <p>Max number of generation allowed before exit</p>
<p>DIP_MO_GA</p> <p>DIP_GA_RESTART</p>	<p><u>6. Selection of GA or MOGA</u></p> <p>Default is running with single-objective GA. Only when this keyword is presented, GLOBAL will perform Multi-objective GA</p>

	(Optional for MOGA) If users want restart from the last generation of the previous run, put this keyword with the output file ('SOLUTION.out')having the last generation results
DIP_GCT 20 BF_Final.GRDECL PERMX0.GRDECL PERMX.GRDECL	<u>7. Selection of GCT</u> Parameterized permeability can be used as a history matching parameter by having this keyword. 20 means the number of basis function defined in 'BF_Final.GRDECL'. Also, 'PERMX0.GRDECL' specifies initial permeability 'PERMX.GRDECL' represents the updated permeability filed during GA

B.2.3 Template (.TMPL) Files and Include (.INC) Files

(1) How templates work?

As shown in Figure B., multiple .TMPL files contain multiple variable names in the format of `__VARNAME__`, the number of variables should be consistent with *.DISTR file, otherwise the code will quit. Take **KR.TMPL** in Figure B. as an example. In template file,

SWOF

0.1 {0.1^__A__ {1-0.1^__A__} 0

0.3 {0.3^__A__} {1-0.3^__A__} 0

0.5 {0.3^__A__} {1-0.3^__A__} 0

.../

Generally there are two steps: **substitution** and **evaluation**:

a. **Each occurrence of `__A__` in a `KR.TMPL` will be substituted with its GA evolved value at the same location** (since `__A__` occurs multiple times, they will be substituted with same values). Assume `__A__=2.0` from GA, after substitutions, we get

SWOF

0.1 {0.1^2.0} {1-0.1^2.0} 0

0.3 {0.3^2.0} {1-0.3^2.0} 0

0.5 {0.3^2.0} {1-0.3^2.0} 0

.../

b. **Evaluations will be made only for expressions enclosed by { },** which gives:

SWOF

0.1 0.01 0.99 0

0.3 0.09 0.91 0

0.5 0.25 0.75 0

.../

If no expressions or string enclosed by { }, no evaluations or calculations will be performed. For instances,

$3*__A__ \rightarrow 3*2.0$ (only substitution)

$3*__A__ \rightarrow 3* 2.0$ (processed as two expressions, only substitution)

$\{3* _A_ \} \rightarrow 6.0$ (substitution and evaluation)

$\{3* _A_ \} \rightarrow \text{error}$ (spaces within { } is not allowed)

The final content (SWOF table) will be same as KR.INC for inclusion to the ECLIPSE input deck or imex.dat for CMG. Therefore, relative permeability defined in **KR.INC** will be changed every time for each population in GA.

(2) Rules to make expressions in .TMPL files

a. The global code will explain every string contains $_ * _$ as an expression, extract the template variable, substitute GA evolved values, and calculate results values.

No space is allowed within one expression. e.g. $\{0.1^ _A_ \}$ will be considered as two expressions and therefore no exponential calculations will be done;

b. Currently supported operators: +, -, *, /, ^, use $\{2.71828^ _A_ \}$ for $\exp(_A_)$;

c. If the expression is complex, use more () to bracket your equation such as 1.0-
 $\{(10^ (_A_ + (2.71828^ _B_)))\}$ to help the program understand better. The rule of thumb is **only one operator allowed in one ()**;

d. Feel free to **check the expression evaluation result** by setting .DISTR to a fixed value (min~max).

B.2.4 The Variable Distribution (.DISTR) File

This file contains the variable distribution, each row formatted as examples in Figure B.:

__VAR1__ base low high resolution log10 continuous

__VAR2__ base low high resolution log10 continuous

...

where "**base**" column of values are used for sensitivity analysis as a baseline in the Tornado diagram. "**low**" and "**high**" column means lower and higher bounds of variables, "**resolution**" column stands for number of bits used to represent the current variable in a genome binary string. 2 bits in Figure B. will give us binary strings 00,01,10,11, which means integer numbers 0-3 for __MV__, which controls the location of fault "block". "log10" column informs whether base/low/high values in current row are after log10. "**continuous**" informs if this variable is continuous (1) or discrete (0, CDF mapping will be done). As shown in Figure B., only __MV__ is a discrete variable, __MULTPV__, __MULTXY__ and __A__ are continuous variables. Comments start with "--".

B.3 How to Run GLOBAL

B.3.1 Run From Visual Studio

If you build your executable from visual studio, build **Release of Win32 or x64**, and then change working directory and command arguments as presented in Figure B.24.

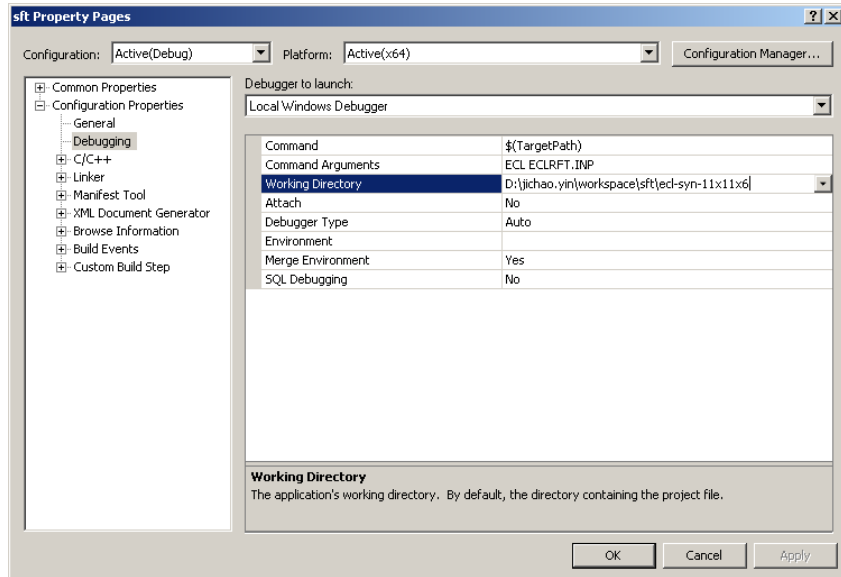


Figure B.24 Run GLOBAL by setting command line arguments

B.3.2 Run From the Command Line

Users can start a command line to run GLOBAL or double click directly on the GLOBAL executable to begin (Figure B.3). Then, input two arguments, which are the type of the simulator and the name of an inversion file (*.INP) respectively.

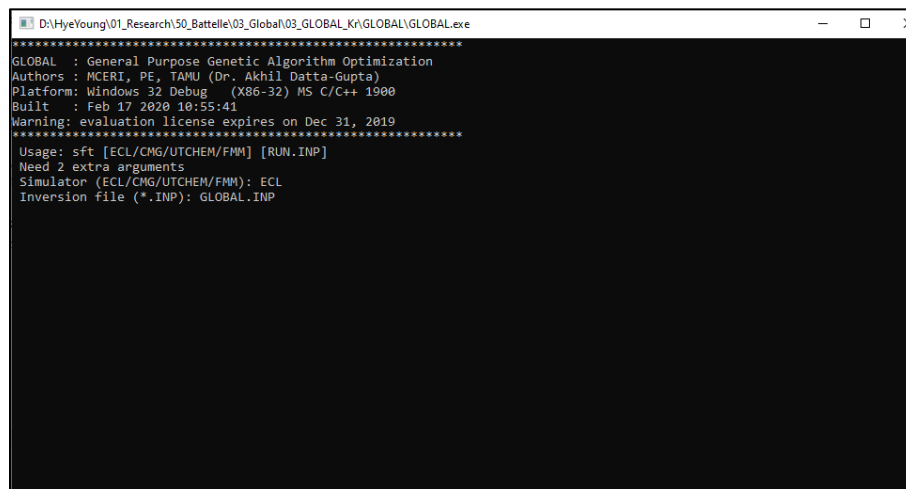


Figure B.3 Run GLOBAL using command line

B.3.3 Output Formats

There are various output files from the GLOBAL run. However, output files from running a GLOBAL are different depending on the algorithm that users used (depending on either GA or MOGA).

1) Running with “GA”

a. **XXX.OUT** - this file contains results of ALL flow simulations, every row is a flow simulation, the columns are (in order):

(1) The first *nvar* columns are variable values (consistent with *.DISTR file and *.TMPL files);

(2) Overall objective value;

(3) Proxy approximated objective value;

(4) Proxy objective error comparing to flow simulation;

(5) Proxy data-exact error. A proxy model constructed by kriging interpolation should reproduce data at experiment points, a polynomial regression proxy will not;

(6) *nobj* individual objective values. *nobj* is consistent with keywords defined in DIP_OBJECTIVE. For example for LPT|MDT, there will be two columns objLPT and objMDT;

(7) Simulation Run ID. For a single inversion, every flow simulation (ECLIPSE or CMG) will be marked with a unique number by the order of run.

- b. XXX.OBJ** - this file contains results of updated flow simulations when objective function reduced (or not higher than 1.10% existing min obj), same format as .OUT
- c. XXX.BIN** - same content as XXX.OUT but in binary, only for restart GA from previous run with same parameter definitions.
- d. XXX.EXP** - same format as .OUT by only *nvar* columns of variable values after Latin Hypercube sampling design. This file is useful for design of experiments research without proxy, GA or flow simulations.
- e. XXX.SENS** - result file from DIP_SENS_RUN, each row is the sensitivity of overall objective (DIP_OBJECTIVE) with respect to a single variable, columns are:

 - (1) Variable name;
 - (2) Lower bound value of the variable;
 - (3) Base value;
 - (4) Upper bound value;
 - (5) Overall objective value when all other variables are set to "Base" values while perturbing current variable to its lower bound;
 - (6) Overall objective value when all other variables are set to "Base" values while perturbing current variable to its upper bound.

2) Running with “**MOGA**”

With the Multi-objective Genetic Algorithm, there is only one output called “Solution.out”. Each column in this output file contains the information as shown below.

(1) The first *nvar* columns are variable values (consistent with *.DISTR file and *.TMPL files);

(2) *nobj* individual objective values. *nobj* is consistent with keywords defined in DIP_OBJECTIVE. For example for LPT|MDT, there will be two columns objLPT and objMDT;

(3) Simulation Run ID. For a single inversion, every flow simulation (ECLIPSE or CMG) will be marked with a unique number by the order of run;

(4) Generation;

(5) Rank. This will be determined while performing non-dominated sorting/ranking algorithm;

(6) Crowding distance. It measures diversity among populations in each generation. Population with a larger crowding distance will be selected for the next generation.